

Kilo-Voltage X-Ray Correction Factors for In-Water Measurements Based on TG-61

by

Nima Sherafati

A thesis submitted to the Faculty of Graduate and Postdoctoral Affairs
in partial fulfillment of the requirements for the degree of

Master of Science

in

Physics

Specialization in Medical Physics

Ottawa-Carleton Institute for Physics

Department of Physics

Carleton University

Ottawa, Ontario, Canada

Nov 2015

© 2015 Nima Sherafati

Abstract

For x-ray tube potentials ≥ 100 kV, the AAPM TG-61 protocol for 40-300 kV x-ray beam dosimetry in radiotherapy recommends an in-water measurement which is based on ionization chambers calibrated in air in terms of air kerma. The variation of the overall correction factor ($P_{Q,cham}$) and its components (known as corrections for the change in the chamber response due to the change in the spectrum distribution in phantom compared to that used for the calibration free in-air ($P_{E,\theta}$), displacement of water by the ionization chamber (P_{dis}) and correction due to the stem for in-water measurement relative to the free in-air calibration ($P_{stem,w}$)) were studied with depth and field size for 6 different beam qualities in the orthovoltage x-ray range (100 kV \leq tube potential ≤ 300 kV). The NE2571 ion chamber, Exradin A16 ion chamber, and Exradin W1 plastic scintillator were considered in this thesis. The last two detectors are not included in the TG-61 protocol.

Based on TG-61, the absorbed dose to water at the reference depth (2 cm) is given by :

$$D_{w,z} = M_w N_K^{air} P_{Q,cham} P_{sheath} \left[\left(\frac{\bar{\mu}_{en}}{\rho} \right)_{air}^w \right]_{water}, \quad (1)$$

where

$$P_{Q,cham} = P_{E,\theta} \times P_{stem,w} \times P_{dis}, \quad (2)$$

M_w is the fully corrected chamber reading for the in-water measurement, N_K^{air} is the air kerma calibration coefficient for a beam's quality, and $\left[\left(\frac{\bar{\mu}_{en}}{\rho} \right)_{air}^w \right]_{water}$ is the ratio for water-to-air of the mean mass energy-absorption coefficient, averaged over the photon spectrum at the reference point in water in the absence of the chamber.

The $P_{Q,cham}$ correction factor is calculated (see above).using two different methods; the direct method where the components of the $P_{Q,cham}$ correction factor are not

considered, and the indirect method where all of the three components of the $P_{Q,cham}$ correction factor are calculated individually and their product equals the $P_{Q,cham}$ correction factor. The values obtained from these two methods are in agreement within the statistical uncertainty.

In contrast with the EGS4 based values used in the TG-61 protocol, the EGSnrc Monte Carlo system was employed which has a systematic uncertainty of $\pm 0.1\%$ relative to its cross-sections while the values of the TG-61 protocol were determined from a combination of measurement and calculation using EGS4 code system which had $\pm 1\%$ systematic uncertainty for ionization chamber calculations. In addition we used the exact geometries of ionization chambers (e.g., the NE2571 ion chamber) and better statistics (up to 10^{11} histories for each simulation giving statistical uncertainties of less than $\pm 0.1\%$) which made an improvement in the correction factor's precision.

The results show that the maximum variation of the $P_{Q,cham}$ correction factor with HVL is 2.6% for the NE2571 ion chamber. Also, our values of the $P_{Q,cham}$ correction factor are not in agreement with those from the TG-61 protocol with the maximum deviation of 0.8% for the low-energy beam. For the Exradin A16 ion chamber and Exradin W1 plastic scintillator, the $P_{Q,cham}$ correction factor varies with HVL up to 26% and 13.5% respectively for a $10 \times 10 \text{ cm}^2$ field size. These variations decreases to 15.5% and 7.5% for a $1 \times 1 \text{ cm}^2$ field size. These large variation indicates that these two detectors should not be used for the kilovoltage x-ray dosimetry.

Acknowledgments

Firstly, I would like to express my sincere gratitude to my advisor Prof. D. W. O. Rogers for the continuous support of my Master study and related research, for his patience, motivation, and immense knowledge. His guidance helped me in all the time of research and writing of this thesis. I could not have imagined having a better advisor and mentor for my Master study.

My sincere thanks also goes to Sara Kashi who provided me an opportunity to discuss various aspects of my research.

Last but not the least, I would like to thank all of the Department faculty members for their help and support. I also thank my parents for the unceasing encouragement, support and attention.

Contents

List of figures	vii
List of tables	vii
Symbols and definitions	vii
1 Introduction	1
1.1 Kilo-Voltage x-ray beam dosimetry	1
1.2 Research motivation	3
2 TG-61	4
2.1 Beam quality specifier	4
2.2 In-Air measurement	6
2.3 In-Water measurement	6
2.4 $P_{Q,\text{cham}}$ correction factor	7
3 Simulation of Kilo-Voltage x-ray beams	11
3.1 SpekCalc	11
3.2 Beam qualities	12
4 Detectors	16
4.1 NE2571 Ion Chamber	16
4.2 Exradin A16 Ion Chamber	17
4.3 Exradin W1 Plastic Scintillator Detector	18
5 Geometries and Monte Carlo simulations	20

5.1	Monte Carlo Method	20
5.2	The EGSnrc code system	21
5.2.1	<i>egs_chamber</i> user code	21
5.3	Variance reduction techniques (VRT)	22
5.3.1	Photon cross-section enhancement technique (XCSE)	23
5.3.2	Range rejection and Russian roulette (RR) technique	24
5.4	Air-Kerma calculation	24
5.5	Detector dose calculation	31
5.6	$P_{Q,\text{cham}}$ calculation	39
5.6.1	$P_{E,\theta}$ calculation	40
5.6.2	$P_{\text{stem},w}$ calculation	42
5.6.3	P_{dis} calculation	46
6	$P_{Q,\text{cham}}$ correction factor	53
6.1	The NE2571 ion chamber	53
6.1.1	The $P_{E,\theta}$ correction factor	59
6.1.2	The $P_{\text{stem},w}$ correction factor	61
6.1.3	The P_{dis} correction factor	63
6.2	The Exradin A16 ion chamber	68
6.2.1	The $P_{E,\theta}$ correction factor	73
6.2.2	The $P_{\text{stem},w}$ correction factor	74
6.2.3	The P_{dis} correction factor	76
6.3	The Exradin W1 plastic scintillator	80
6.3.1	The $P_{E,\theta}$ correction factor	81
6.3.2	The $P_{\text{stem},w}$ and P_{dis} correction factors	89
7	Conclusions	91

7.1	The NE2571 ion chamber	91
7.2	The Exradin A16 ion chamber	92
7.3	The Exradin W1 plastic scintillator	93
References		95

List of Tables

3.1	Comparison between BEAMnrc, SpekCalc and IPEM78 for the measurement of HVL	12
3.2	Beam qualities in terms of HVL and the beam average energy as calculated by SpekCalc	14

List of Figures

2.1	X-ray tube potential versus HVL	4
2.2	Measurement of the half-value layer	5
3.1	SpekCalc graphical user interface software	11
3.2	Spectra for six different x-ray tube potentials and filters	13
3.3	Kilovoltage x-ray tube depth-dose curves for 100 cm ² field size	14
3.4	Kilovoltage x-ray tube depth-dose curves for 25 cm ² field size	15
3.5	Kilovoltage x-ray tube depth-dose curves for 1 cm ² field size	15
4.1	Geometry of the NE2571 ion chamber	16
4.2	Geometry of the Exradin A16 ion chamber	17
4.3	Geometry of the Exradin W1 ion chamber	19
5.1	The variation of kerma values for 100 kV x-ray beam with cavity thickness	25
5.2	The geometry for the calculation of water kerma and air kerma in a water phantom	26
5.3	The variation of $\left[\left(\frac{\bar{\mu}_{en}}{\rho} \right)_{air}^w \right]_{water}$ values with HVL	27
5.4	The variation of $\left[\left(\frac{\bar{\mu}_{en}}{\rho} \right)_{air}^w \right]_{water}$ values with depth	27
5.5	The geometry for the calculation of air kerma free in-air and in-water . .	28
5.6	The ratio of the air kerma in-water to in-air calculation for six beam qualities with depth	29
5.7	The ratio of the air kerma in-water to in-air calculations for six beam qualities with depth	30
5.8	The ratio of the air kerma in-water to in-air calculation for six beam qualities with depth	30
5.9	Geometry of detector dose calculations	32

5.10	The ratio of the NE2571 ion chamber dose in-water to the in-air calculation for the six beam qualities with depth for 10 cm field size beam	33
5.11	The ratio of the NE2571 ion chamber dose in-water to the in-air calculation for the six beam qualities with depth for 5 cm field size beam	34
5.12	The ratio of the Exradin A16 ion chamber dose in-water to the in-air calculation for the six beam qualities with depth for 10 cm field size beam	35
5.13	The ratio of the Exradin A16 ion chamber dose in-water to the in-air calculation for the six beam qualities with depth for 5 cm field size beam	35
5.14	The ratio of the Exradin A16 ion chamber dose in-water to the in-air calculation for the six beam qualities with depth for 10 cm field size beam	36
5.15	The ratio of the Exradin W1 plastic scintillator dose in-water to the in-air calculation for the six beam qualities with depth for 10 cm field size beam	37
5.16	The ratio of the Exradin W1 plastic scintillator dose in-water to the in-air calculation for the six beam qualities with depth for 5 cm field size beam	37
5.17	The ratio of the Exradin W1 plastic scintillator dose in-water to the in-air calculation for the six beam qualities with depth for 10 cm field size beam	38
5.18	The geometries for the calculation of the $P_{E,\theta}$	41
5.19	Geometry for the $P_{stem,w}$ calculation	44
5.20	Geometry for the P_{dis} calculation	47
5.21	Geometry for the calculation of the primary photons contribution to the P_{dis}	50
6.1	The $P_{Q,cham}$ values for NE2571ion chamber at 2 cm depth	54
6.2	$P_{Q,cham}, P_{E,\theta}, P_{stem,w}, P_{dis}$ versus HVL for the NE2571 ion chamber at 2 cm depth in water	56
6.3	$P_{Q,cham}, P_{E,\theta}, P_{stem,w}, P_{dis}$ versus HVL at 5 cm depth in water for 5 cm and 10 cm field sizes	57
6.4	$P_{Q,cham}, P_{E,\theta}, P_{stem,w}, P_{dis}$ versus HVL at 8 cm depth in water for 5 cm and 10 cm field sizes	58
6.5	$P_{Q,cham}, P_{E,\theta}, P_{stem,w}, P_{dis}$ versus HVL at 11 cm depth in water for 5 cm and 10 cm field sizes	58

6.6	Comparison of pet in this study with previous studies	61
6.7	A comparison between $P_{stem,w}$ values in this study with previous studies	62
6.8	The values for $\Delta_p K_{air}^w, \Delta_s K_{air}^w$, and \bar{K}_{air}^w at 2 cm depth in water	63
6.9	The values for $\Delta_p K_{air}^w, \Delta_s K_{air}^w$, and \bar{K}_{air}^w at 5 cm depth in water	64
6.10	The values for $\Delta_p K_{air}^w, \Delta_s K_{air}^w$, and \bar{K}_{air}^w at 8 cm depth in water	64
6.11	The values for $\Delta_p K_{air}^w, \Delta_s K_{air}^w$, and \bar{K}_{air}^w at 11 cm depth in water	65
6.12	The comparison between displacement correction factors	66
6.13	The $P_{Q,cham}$ values for the Exradin A16 ion chamber at 2 cm depth	68
6.14	The variations of the $P_{Q,cham}$ components of Exradin A16 ion chamber with HVLs for three different field sizes	69
6.15	The variations of the $P_{Q,cham}$ components of Exradin A16 ion chamber with HVLs for three different field sizes at 5 cm depth	71
6.16	The variations of the $P_{Q,cham}$ components of Exradin A16 ion chamber with HVLs for three different field sizes at 8 cm depth	72
6.17	The $P_{Q,cham}$ values for the Exradin A16 ion chamber with different electrode at 2 cm depth	74
6.18	The $P_{stem,w}$ values for the Exradin A16 ion chamber and its component .	75
6.19	The values for $\Delta_p K_{air}^w, \Delta_s K_{air}^w$, and \bar{K}_{air}^w at 2 cm depth in water for the Exradin A16 ion chamber	77
6.20	The values for $\Delta_p K_{air}^w, \Delta_s K_{air}^w$, and \bar{K}_{air}^w at 5 cm depth in water for the Exradin A16 ion chamber	78
6.21	The values for $\Delta_p K_{air}^w, \Delta_s K_{air}^w$, and \bar{K}_{air}^w at 8 cm depth in water for the Exradin A16 ion chamber	79
6.22	The $P_{Q,cham}$ values for the Exradin W1 plastic scintillator at 2 cm depth .	80
6.23	The $\left[\left(\frac{\bar{\mu}_{en}}{\rho} \right)_{pst}^{air} \right]_{water}^{air}$ values at 2 cm depth	83
6.24	The $\left[\left(\frac{\bar{\mu}_{en}}{\rho} \right)_{pst}^{air} \right]_{water}^{air}$ values normalized to 1 cm field size at 2 cm depth .	84
6.25	The variations of the $P_{Q,cham}$ components of Exradin W1 plastic scintillator with HVLs for three different field sizes	86
6.26	The variations of the $P_{Q,cham}$ components of Exradin W1 plastic scintillator with HVLs for three different field sizes	87
6.27	The variations of the $P_{Q,cham}$ and its components of the Exradin W1 plastic scintillator with HVLs for three different field sizes at 8 cm depth	88

Symbol	Definition
$AAPM$	American Association of Physicists in Medicine.
B_w	Back scatter factor.
D_{cav}^{air}	Dose to the detector cavity for detector free in-air.
D_{cav}^w	Dose to the detector cavity for detector in the water phantom.
$D_{cav}^{w,stemless}$	Dose to the detector cavity for stemless detector in the water phantom.
$D_{cav}^{air,stemless}$	Dose to the detector cavity for stemless detector free in-air.
E_{mean}	Mean energy of the incident x-ray beam.
f	Ratio of dose to the medium to the dose to the detector's cavity.
$K_{air}^{free\ in-air}$	Air kerma free-in-air .
K_{air}^w	Air kerma in the water phantom.
\bar{K}_{air}^w	Air kerma to the small volume surrounded by an air cavity with outer dimensions of the detector.
$(K_{air}^w)_p$	The same as K_{air}^w except for the primary photons.
$(K_{air}^w)_s$	The same as K_{air}^w except for the scattered photons.
$(\bar{K}_{air}^w)_p$	The same as \bar{K}_{air}^w except for the primary photons.
$(\bar{K}_{air}^w)_s$	The same as \bar{K}_{air}^w except for the scattered photons.
k_{bq}	Ratio of dose to the detector cavity to the detector's reading.
$\Delta_p K_{air}^w$	Change of the \bar{K}_{air}^w due to the displaced water for the primary photons.
$\Delta_s K_{air}^w$	Change of the \bar{K}_{air}^w due to the displaced water for the scattered photons.
HVL	Half value layer of an x-ray beam.
$IAEA$	International Atomic Energy Agency.
$ICRU$	International Commission on Radiation Units and Measurements.
M_{air}	Detector reading for the free-in-air measurement.
M_w	Detector reading for the in-water measurement
$NCRP$	National Council on Radiation Protection and Measurements.
N_K^{air}	air-kerma calibration coefficient for free-in-air measurement.
$P_{Q,cham}$	Overall detector correction factor for in-water measurement.
$P_{E,\theta}$	Beam quality correction factor for in-water measurement.
$P_{stem,air}$	Stem correction factor for in-air measurement.
$P_{stem,w}$	Stem correction factor for in-water relative to the in-air measurement.
$\bar{P}_{stem,w}$	Stem correction factor for in-water measurement.
$p_{st}(z, d)$	The ratio of the water kerma in a cylindrical water cavity without stem to the water kerma in the same water cavity with stem at depth z and field size d.
k_{st}	The ratio of the detector signal for the free-in-air measurements with stem to the one with an extra dummy stem.
P_{dis}	Displacement correction factor.
P_{dis}^{NK}	Displacement correction factor calculated by Nahum and Knight ¹ .
P_{dis}^{MN}	Displacement correction factor calculated by Ma and Nahum ² .
P_{dis}^{SV}	Displacement correction factor calculated by Seuntjens and Verhaegen ³ .
$(\sigma_p e)_{air}^w$	The ratio of the photoelectric cross-section for the in-water to the in-air measurement for a specific photon beam.

Chapter 1

Introduction

1.1 Kilo-Voltage x-ray beam dosimetry

Kilovoltage x-ray beams have been widely used for a wide variety of different applications since the last century. These days, clinical applications of kilovoltage x-rays consist of diagnostic imaging and external radiotherapy especially for skin cancer therapy since the maximum dose occurs close to the surface for this range of energy.

Based on a survey which had been done by the American Association of Physicists in Medicine (AAPM) in 1995, there were more demands for kilovoltage x-ray units showing a renewed interest in kilovoltage x-ray beams for external radiotherapy^{4,5}. For this reason, measurement of absorbed dose as accurately as possible became more important.

There are several dosimetry protocols for kilovoltage x-ray tubes such as ICRU Report No. 23⁶, National Council on Radiation Protection and Measurements (NCRP) Report No. 69⁷, International Atomic Energy Agency (IAEA) Code of Practice⁸ and AAPM Radiation Therapy Committee Task Group 61 (TG-61)⁵. The present research follows the TG-61 protocol which is based on an ionization chamber calibrated in terms of air-kerma free in-air,

$$K_{air}^{free\ in-air} = M_{air} N_K^{air}, \quad (1.1)$$

where $K_{air}^{free\ in-air}$ is the air kerma (kinetic energy released per unit mass, defined as the total of the initial kinetic energies of charged particles per unit mass liberated by uncharged ionization radiation) free in-air, M_{air} is the reading of the ionization chamber which must be corrected for temperature, pressure, recombination, polarity effects, and

electrometer accuracy; and N_K^{air} is the calibration coefficient for in-air measurement. Note that although TG-61 is based on ionization chambers calibrated in air, it does not limit users from considering other types of detectors and this thesis also investigates the Exradin W1 which is a plastic scintillator detector.

TG-61 consists of three main parts; first, determination of the half value layer (HVL) for each beam is discussed; second, the in-air calibration method is explained for x-ray tube potentials between 40 kV and 300 kV and if one is interested in absorbed dose at the surface of the water phantom; and finally, for x-ray tube potentials between 100 kV and 300 kV, the in-water method is recommended if the reference point of measurement is at depth in water.

This thesis focuses on medium energy x-rays (tube potential 100 - 300 kV) where the in-water method is recommended and the most important correction factor is $P_{Q, cham}$, the overall chamber correction factor, that accounts for changes in detector response (i.e., beam quality dependence) due to the differences between use of the detector in-air and in a water phantom.

Generally speaking, the beam quality dependence of a detector can be described in two parts⁹. First, a conversion factor, called k_{bq} , converts the detector's reading to the dose to the sensitive volume of the detector, hence

$$D_{cav} = k_{bq} M_{det} , \quad (1.2)$$

where D_{cav} and M_{det} are dose to the detector's cavity and detector's reading respectively. For an ion chamber detector, it is assumed that the k_{bq} conversion factor (i.e., $\left(\frac{W}{e}\right)_{air}$) to be constant although it has been shown there is some variation¹⁰. For the Exradin W1 plastic scintillator, the k_{bq} conversion factor can be beam quality dependent and the assumption of constant k_{bq} factor needs to be verified⁹.

The second part of the beam quality dependence of a detector consists of a conversion factor, called f , which relates the dose to the detector to the dose to the medium,

$$D_{med} = f D_{cav} , \quad (1.3)$$

where D_{med} is dose to the water. In this thesis, the k_{bq} conversion factor is considered as a constant for the NE2571 and Exradin A16 ion chambers, while for the Exradin W1 plastic scintillator, only the f conversion factor is considered which is approximately

equivalent to

$$f = \left(\frac{\bar{\mu}_{en}}{\rho} \right)_{pst}^{water}, \quad (1.4)$$

where the right hand side is the ratio for medium to polystyrene of the mean mass energy absorption coefficient averaged over the photon energy fluence spectrum. Note that the effect of wall for the Exradin W1 plastic scintillator in eqn 1.4 is considered to be small in comparison to $\left(\frac{\bar{\mu}_{en}}{\rho} \right)_{pst}^{water}$ due to the small size of the detector.

Starting with a description of the TG-61 formalism for in-water measurement, simulation of x-ray beams and geometry of detectors will be explained in detail as well as the variation of the $P_{Q,cham}$ correction factor with depth, beam quality and field size for the three different detectors.

1.2 Research motivation

The $P_{Q,cham}$ values in TG-61 were reported at 2 cm depth in a water phantom for several ionization chambers such as the NE2571 chamber. This research studies the variation of $P_{Q,cham}$ with depth (2 - 11 cm) and three field sizes ($1 \times 1 \text{ cm}^2$, $5 \times 5 \text{ cm}^2$, $10 \times 10 \text{ cm}^2$) for six different beam qualities (100 kV - 300 kV x-ray tube potential).

The values of $P_{Q,cham}$ for the NE2571 ion chamber in TG-61¹¹ protocol were calculated using the EGS4 code system¹² which has 1% systematic uncertainty in the calculation of the ionization chamber response for Cobalt beams and even higher for lower energy beams¹³. This research uses the EGSnrc code system¹⁴, which is the improved version of the EGS4 code system, to investigate the effects of this systematic uncertainty on the $P_{Q,cham}$ values for the NE2571 ion chamber.

In addition to the NE2571 ion chamber, the Exradin A16 ion chamber and Exradin W1 plastic scintillator detector are considered. These are not included in TG-61 protocol.

Chapter 2

TG-61

2.1 Beam quality specifier

It is essential to know what kind of radiation (quality) is being used since it is needed for correct measurement of radiation at the point of interest. According to the TG-61 protocol, kilovoltage x-ray beams should be specified by using two parameters; the half value layer of the beam (HVL) and the x-ray tube potential. Quality is expressed in terms of half value layer which is “the thickness of a specified attenuator (filter) that reduces the air-kerma rate in a narrow beam to one half of its original value”⁶, also known as the first HVL. It has been shown that for one x-ray tube potential there are different HVL values due to the different filtrations and there can be several tube potentials correspond for one HVL⁴, as shown in fig 2.1.

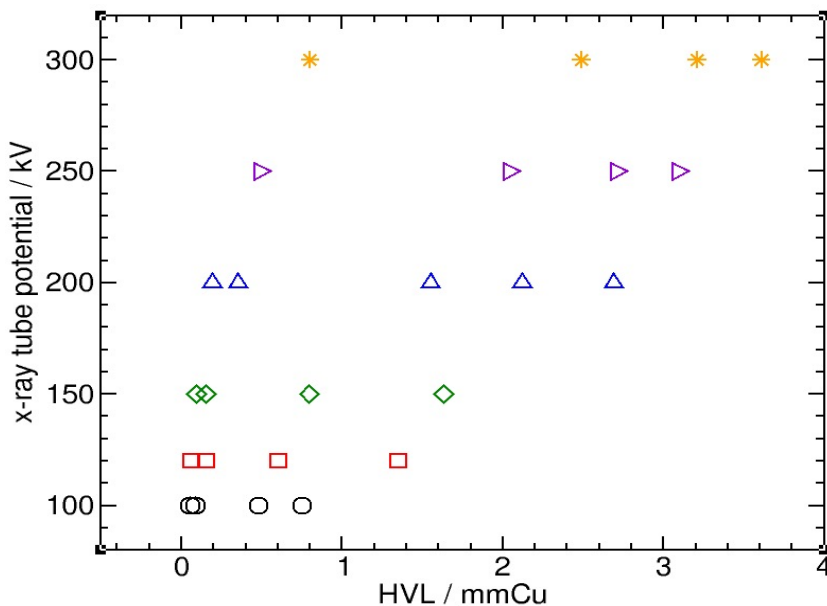


Figure 2.1: X-ray tube potential for different HVLs specified by copper thickness in mm. Data calculated using the SpekCalc software¹⁵.

The experimental setup for determination of HVL as explained in the TG-61 protocol is shown in fig 2.2. The diaphragm defines the beam field size. The diaphragm should not exceed 4 cm diameter and its thickness should be able to attenuate the primary beam to 0.1% of the incident photon beam. The distance between attenuator and detector should be at least 50 cm to avoid electron contamination produced by the attenuator material and diaphragm. The monitor chamber is necessary to correct for the variation of air-kerma rate and its position should not effect the beam in terms of scatter component. The beam after attenuator material should cover the sensitive volume of the detector, so smaller detectors are preferable for the air-kerma measurement. In addition, the variation in detector response must be less than 5% with beam qualities for 40 - 300 kV x-ray tubes to maximize the accuracy of the HVL measurement since the attenuator changes the beam quality. The accuracy of the attenuator thickness measurement should be 0.05 mm and high purity materials (99.9%) can significantly improve the measurement of HVL.

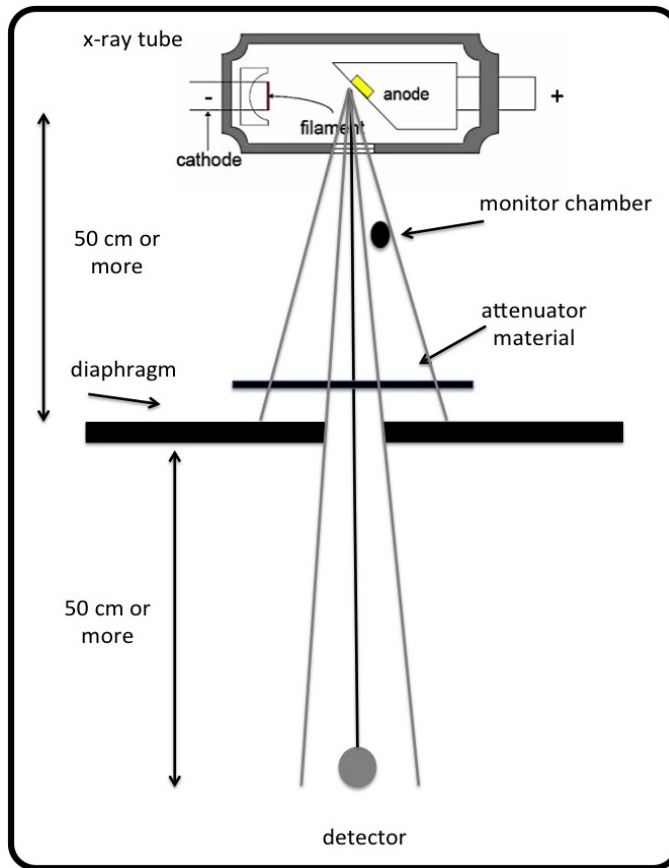


Figure 2.2: Arrangement for the half-value layer measurement.

2.2 In-Air measurement

The in-air method is recommended in the TG-61 protocol for x-ray tube potentials between 40 kV and 300 kV if the point of interest is at the phantom surface ($z_{ref} = 0$). To determine absorbed dose at the surface of a water phantom one can use the following equation,

$$D_{w,z=0} = M_{air} N_K^{air} B_w P_{stem,air} \left[\left(\frac{\bar{\mu}_{en}}{\rho} \right)_{air}^w \right]_{air}, \quad (2.1)$$

where M_{air} is the fully corrected detector reading free in-air, N_K^{air} is the air kerma calibration coefficient for the user's beam, B_w is the backscatter correction factor which accounts for the existence of the water phantom which increases the dose due to the backscattered particles; $P_{stem,air}$ is the stem correction factor which is related to the difference between the in-air calibration and an in-air measurement mainly due to the change in the field size of the beam (i.e., $P_{stem,air}$ equals to unity if the same field size is used in the calibration and the measurement for a given beam quality). $\left[\left(\frac{\bar{\mu}_{en}}{\rho} \right)_{air}^w \right]_{air}$ is the ratio for water to air of the mean mass energy-absorption coefficients averaged over the incident photon energy fluence spectrum.

For x-ray tube potentials below 70 kV, a parallel plate chamber is recommended where the effective point of measurement is at the centre of the sensitive air cavity. To create full buildup, a low-Z thin plastic cap (e.g. PMMA or polyethylene) is used. This also eliminates electron contamination. Additional details about the in-air method can be found in the TG-61 protocol⁵.

2.3 In-Water measurement

The in-water (in-phantom) method is recommended in TG-61 protocol if one is interested in absorbed dose at depth in a water phantom for x-ray tube potentials between 100 kV and 300 kV where the measurements are performed using a cylindrical ion chambers with the effective point of measurement at the centre of the sensitive air cavity. The reference point of measurement is at 2 cm depth in the water phantom since there is enough signal to be detected and buildup (charge particle equilibrium) is achieved. The IAEA TRS-277⁸ and IAEA TRS-398¹⁶ codes of practice recommend 5 cm depth as the reference point of measurement in the water phantom which provides less signal than

one at 2 cm depth. This is the main reason why a 2 cm depth has been recommended in the TG-61 protocol.

Absorbed dose to water at 2 cm reference depth is obtained using

$$D_{w,z=2cm} = M_w N_K^{air} P_{Q,cham} P_{sheath} \left[\left(\frac{\bar{\mu}_{en}}{\rho} \right)_{air}^w \right]_{water}, \quad (2.2)$$

where M_w is the fully corrected reading of the detector at 2 cm depth in water; N_K^{air} is the air kerma calibration coefficient free in-air; $P_{Q,cham}$ is the overall correction factor and will be discussed in detail in the next section; P_{sheath} is the correction factor when using a waterproof sleeve as needed for the NE2571 ionization chamber once the measurement is in a water phantom as opposed to the Exradin A16 and Exradin W1 which are waterproofs and hence $P_{sheath} = 1$; and $\left[\left(\frac{\bar{\mu}_{en}}{\rho} \right)_{air}^w \right]_{water}$ is the ratio for water to air of the mean mass energy absorption coefficients, averaged over the photon energy fluence spectrum at the reference point in water.⁵

2.4 $P_{Q,cham}$ correction factor

As mentioned in chapter 1, the TG-61 protocol is based on a detector calibrated in terms of the air kerma free in-air. For in-water measurements, the free in-air calibration coefficient, N_K^{air} , must be used with correction factors which take into account the effect of the water phantom on the calibration coefficient for the in-air measurement, namely $P_{Q,cham}$, the overall correction factor.

This research studies $P_{Q,cham}$ using two different methods, direct and indirect methods. For direct calculation of $P_{Q,cham}$, one can consider a detector to measure the air kerma in water at the reference depth using

$$K_{air}^w = M_w N_K^w, \quad (2.3)$$

where K_{air}^w is the air kerma in water; M_w is the fully corrected detector reading and N_K^w is the calibration coefficient for in-water measurement which is unknown since the detector is calibrated based on the air kerma free in-air (N_K^{air}).

To solve this problem, one can use N_K^{air} instead of N_K^w in eqn 2.3 then multiply it by $\frac{N_K^w}{N_K^{air}}$ as follows,

$$K_{air}^w = M_w N_K^{air} \times \frac{N_K^w}{N_K^{air}} , \quad (2.4)$$

where $\frac{N_K^w}{N_K^{air}}$ is the $P_{Q,cham}$ correction factor which must be obtained using computational simulations or measurements, i.e., one can calculate the detector's cavity dose using simulation or measure it through an experiment. Eqn 2.4 can be written as

$$K_{air}^w = M_w N_K^{air} P_{Q,cham} . \quad (2.5)$$

Using the relation between water kerma and air kerma in water,

$$K_{water} = K_{air}^w \left[\left(\frac{\bar{\mu}_{en}}{\rho} \right)_{air}^w \right]_{water} , \quad (2.6)$$

and eqn 2.5, one has,

$$K_{water} = M_w N_K^{air} P_{Q,cham} P_{sheath} \left[\left(\frac{\bar{\mu}_{en}}{\rho} \right)_{air}^w \right]_{water} , \quad (2.7)$$

where P_{sheath} is the correction factor for using any waterproof sleeve and defined as,

$$P_{sheath} = \frac{D_{cav}^{no\ sleeve}}{D_{cav}^{with\ sleeve}} , \quad (2.8)$$

where $D_{cav}^{no\ sleeve}$ and $D_{cav}^{with\ sleeve}$ are the dose to the detector's cavity in a water phantom without and with the waterproof sleeve respectively. The P_{sheath} correction factor can be calculated using the Monte Carlo simulations for a non-waterproof detector (i.e., the NE2571 ion chamber).

The water kerma in eqn 2.7 is equivalent to the dose in eqn 2.2 under the assumptions of quasi-charged particle equilibrium⁶ and negligible difference between the collision kerma and kerma ($K_{col} = K(1 - g)$ where g is the average fraction of energy transferred to the charged particles that is lost through the bremsstrahlung radiation.⁵),

i.e., dose at the reference point in water can be approximated by

$$D_w = K_{water} , \quad (2.9)$$

which leads to the eqn 2.2 on p 7.

To calculate the $P_{Q,cham}$, one can replace the calibration coefficients by their equivalents using eqns 1.1 and 2.3,

$$P_{Q,cham} = \frac{N_K^w}{N_K^{air}} = \frac{\frac{K_{air}^w}{M_w}}{\frac{K_{air}^{free\ in-air}}{M_{air}}} = \frac{K_{air}^w}{K_{air}^{free\ in-air}} \times \frac{M_{air}}{M_w} \quad (2.10)$$

The ratio of the detector reading for the in-air and in-water phantom at eqn 2.10 can be measured by doing an experiment but for the simulation, one can use the relation between absorbed dose in the ionization chamber and the collected charge inside the ionization chamber for the in-air and in-water measurements,

$$D_{cav}^{air} = \frac{M_{air}}{m_{air}} \times \left(\frac{W_{air}}{e} \right), \quad (2.11)$$

$$D_{cav}^w = \frac{M_w}{m_{air}} \times \left(\frac{W_{air}}{e} \right), \quad (2.12)$$

where m_{air} is the mass of the sensitive air inside the ionization chamber and $\left(\frac{W_{air}}{e} \right)$ is the average energy required to create one ionization in the air inside the ionization chamber which is assumed is constant. Dividing eqn 2.11 by eqn 2.12 one can have

$$\frac{D_{cav}^w}{D_{cav}^{air}} = \frac{\frac{M_w}{m_{air}} \times W}{\frac{M_{air}}{m_{air}} \times W} = \frac{M_w}{M_{air}} . \quad (2.13)$$

The left hand side of the eqn 2.13 can be calculated using the Monte Carlo simulations. Eqn 2.10 can be rewritten as,

$$P_{Q,cham} = \frac{K_{air}^w}{K_{air}^{free\ in-air}} \times \frac{D_{cav}^w}{D_{cav}^{air}} . \quad (2.14)$$

Eqn 2.13 has been widely used in the Monte Carlo simulations and in general can be used for all detectors. Ma and Nahum used the same approach to calculate the $P_{Q,cham}$ correction factor.²

For indirect calculation of the $P_{Q,cham}$ correction factor, one can study its components individually.

The $P_{Q,cham}$ correction factor consists of three different components :

$$P_{Q,cham} = P_{E,\theta} P_{stem,w} P_{dis} , \quad (2.15)$$

where

$P_{E,\theta}$ is the correction for changes in the beam quality (energy and direction of the incident particles) for in-water measurements compared to the measurements free in-air.

$P_{stem,w}$ is the stem correction factor which takes into account the difference of stem effect between in-water measurement and the in-air calibration.

P_{dis} corrects for the displaced water caused by the overall air cavity with its size equal to the detector's outer dimensions excluding the stem part. Note that N_K^{air} takes into account the effect of replacing the detector's materials with air for in-air measurements.

The components of the $P_{Q,cham}$ correction factor are investigated in order to understand the $P_{Q,cham}$ variations. (see chapter 6, page 53)

Generally speaking, direct calculation of $P_{Q,cham}$ is more efficient than indirect calculation since it takes less computational time and has lower uncertainty; on the other hand, indirect calculation is required to understand the variation of $P_{Q,cham}$ in terms of a detector's structure and materials.

Chapter 3

Simulation of Kilo-Voltage x-ray beams

3.1 SpekCalc

For calculating correction factors, as the first step it is very important to obtain x-ray emission spectra accurately as well as the half value layer. This research often considers the energy fluence spectrum which is a plot of the fluence at a given energy times the energy as opposed to a fluence spectrum such as that shown in fig 3.1 which plots the fluence at a given energy. SpekCalc is software which is able to simulate x-ray spectra from tungsten anodes in x-ray tubes and has been used in medical physics since 2009.

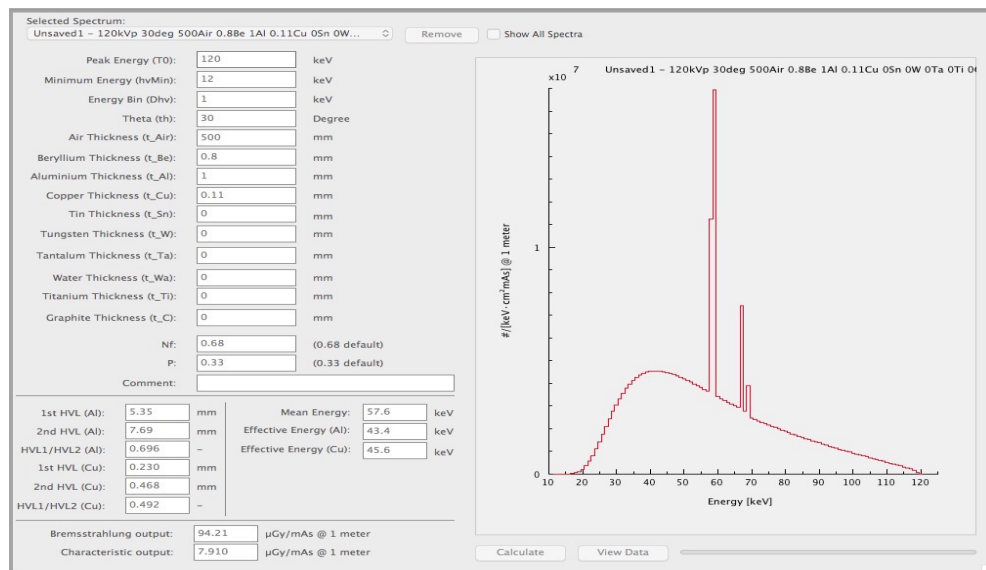


Figure 3.1: This is the graphical user interface of SpekCalc software running on the computer.

Figure 3.1 shows the control panel (left side) for the simulation of x-ray spectra where one can choose specific x-ray tube potential, bin size of the spectrum as well as different thickness for filtrations. The simulated spectrum is displayed on the right hand side as are calculated first and second HVLs in terms of thickness of Aluminum and Copper.

In the literature, x-ray beam quality has been compared between SpekCalc and other available programs such as IPEM78¹⁷ and BEAMnrc¹⁸. Table 3.1 shows a numerical comparison between these three sources of x-ray beams¹⁵.

Table 3.1: Quality of the x-ray beams produced by BEAMnrc, SpekCalc and IPEM78 for a tungsten anode and anode angle of 25 degrees.¹⁵

	kV	50	70	100	140		190	250
BEAMnrc	HVL (mm)	1.77	2.45	4.81	6.48	Al	1.36	1.87
	E_{mean} (keV)	32.4	39.7	52.7	62.5		93.5	107.1
SpekCalc	HVL (mm)	1.74	2.38	4.78	6.46	Al	1.39	1.93
	E_{mean} (keV)	32.4	39.6	53.0	62.8		94.6	109.0
IPEM78	HVL (mm)	1.83	2.59	4.91	6.70	Al		
	E_{mean} (keV)	32.5	40.1	52.9	62.9			

3.2 Beam qualities

The values of $P_{Q,chan}$ reported in TG-61 are from Seuntjens et al.¹¹, for x-ray beam qualities between 0.1 and 4.0 mm Cu where they used various combination of Al, Cu and Sn as filters.

This study considers x-ray tube potentials between 100 kV and 300 kV; for the filtration, Al and Cu are used to be consistent with the calculation of ratios of mass-energy absorption coefficients and backscatter factors calculated by Ma and Seuntjens¹⁹. Their values are included in the TG-61 protocol⁶.

For SpekCalc software calculation, the tungsten anode angle is 30 degrees to the line perpendicular to the incident electron beam and 50 cm thickness of air is considered. By adjusting x-ray tube potential and the thickness of Al and Cu, 6 different x-ray beam qualities between 0.08 and 3.6 mm Cu were calculated. In addition to table 3.2, the spectra of the x-ray beams are shown in fig 3.2.

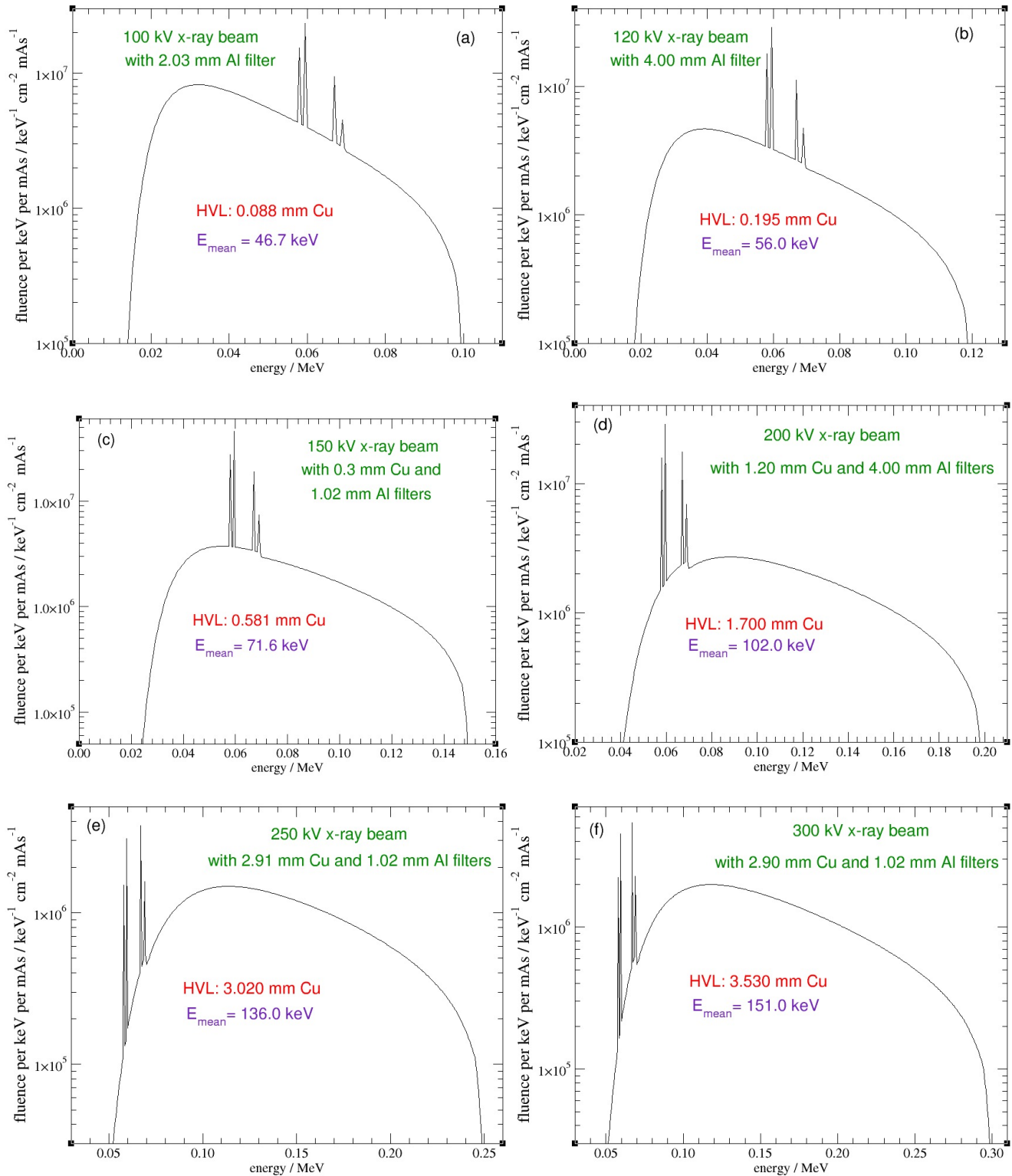


Figure 3.2: Spectra for six different x-ray tube potentials and filters as presented in table 3.2. The spectra are considered uniform across the entire field.

Table 3.2: Beam qualities and x-ray tube potentials used in this research as calculated by SpekCalc. The anode is made of tungsten and makes 30 degree from the line perpendicular to the incident electron beam.

kV	Filtration	HVL (mm Cu)	E_{mean} (keV)
100	2.03 mm Al	0.088	46.7
120	4.00 mm Al	0.195	56.0
150	0.30 mm Cu + 1.02 mm Al	0.581	71.6
200	1.20 mm Cu + 4.00 mm Al	1.700	102.0
250	2.91 mm Cu + 1.02 mm Al	3.020	136.0
300	2.90 mm Cu + 1.02 mm Al	3.530	151.0

Note that 120 kV x-ray beam was chosen to study the variation of $P_{Q, cham}$ between 100 kV and 150 kV x-ray beams where the $P_{Q, cham}$ variation is maximum (see chapter 6, p 54). Depth-dose curves normalized to the surface dose in a water phantom for the six different x-ray beam qualities (see table 3.2) are shown in figs 3.3, 3.4, and 3.5. The DOSRZnrc user code²⁰ was used for these calculations. Electron and photon cutoffs were 0.521 MeV and 0.01 MeV respectively. The bin size for the calculation of depth-dose curves was 0.2 cm thick with 0.1 cm diameter.

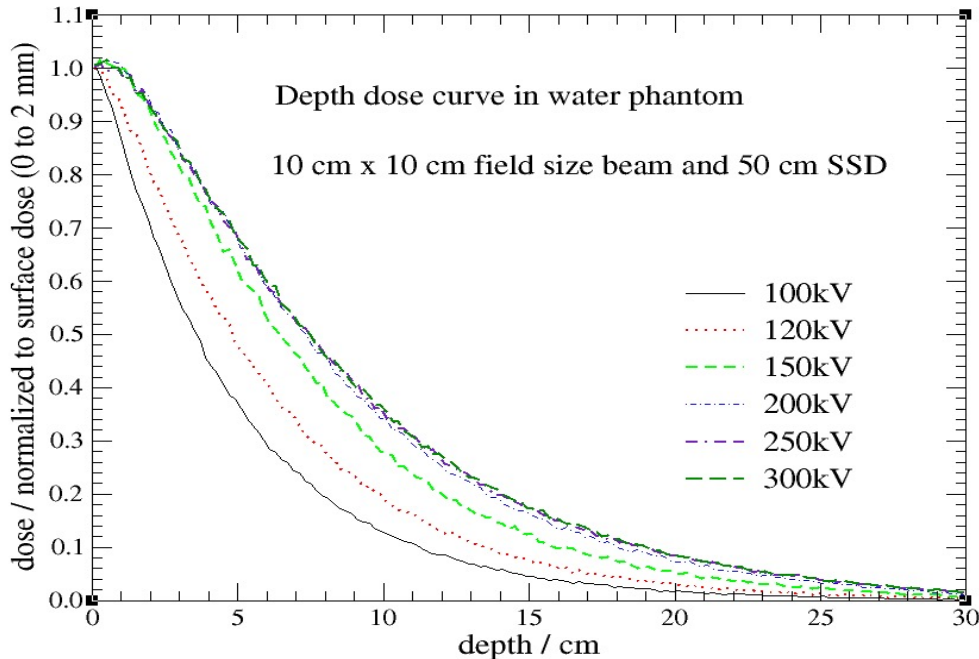


Figure 3.3: Depth-dose curves for 100 - 300 kV x-ray beams with 100 cm^2 field size and SSD = 50 cm with bin thickness = 0.2 cm and 0.1 cm diameter.

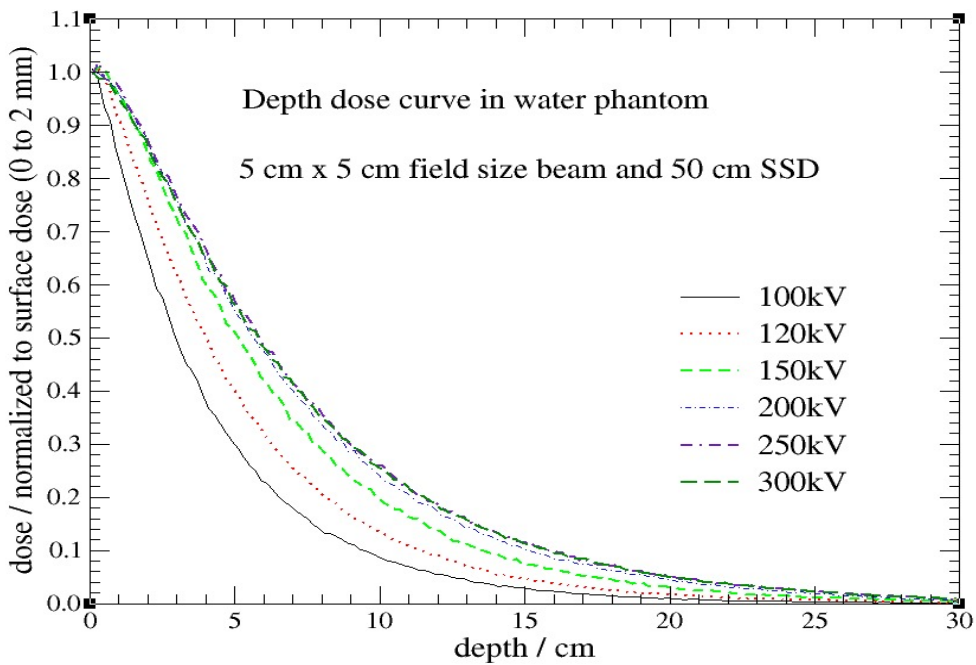


Figure 3.4: Same as fig 3.3 but for 25 cm² field size.

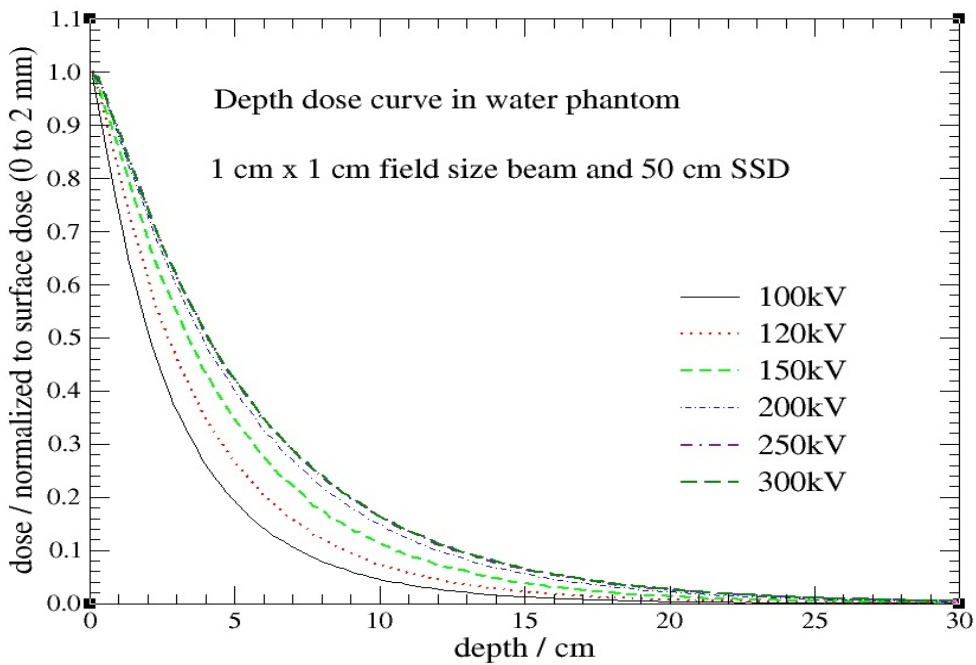


Figure 3.5: Same as fig 3.4 but for 1 cm² field size.

Chapter 4

Detectors

4.1 NE2571 Ion Chamber

One of the well known Farmer-type chambers is the NE2571 ion chamber which has been used throughout the world for the measurement of photon and electron beam dose. The NE2571 ion chamber is constructed with a thin wall of high purity graphite for the thimble and an aluminum electrode with 0.67 cm^3 air cavity volume. The NE2571 ion chamber is not waterproof and must be protected with a waterproof sleeve for in-water measurement. The geometry and materials of the NE2571 ion chamber are shown in fig 4.1.

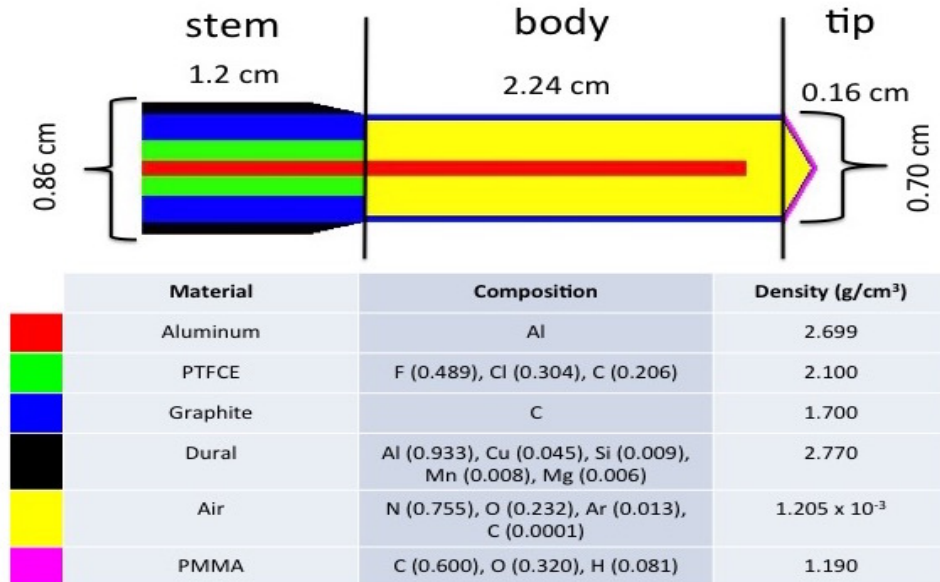


Figure 4.1: Geometry and materials of the NE2571 ion chamber created by the egs++ library²¹ for calculations with the egs_chamber user code. The vertical black lines separate detector's body from the stem and tip. It is not drawn to scale.

The NE2571 ion chamber consists of two parts; stem and body. The stem is composed of an aluminum electrode surrounded by PTFCE, graphite and Dural. The respective radii are 0.05, 0.175, 0.35 and 0.431 cm. The stem has a cylindrical shape for 0.9 cm at which point the Dural tapers off to 0.35 cm radius over a distance of 0.3 cm. The body is cylindrical for 2.24 cm, filled with air to a radius of 0.314 cm surrounding the 2.05 cm length aluminum electrode of radius 0.05 cm. The graphite walls are 0.036 cm thick to an outer radius of 0.35 cm. The cylindrical component of the body is attached to the tip with 0.16 cm length. At the tip, the graphite walls are 0.0183 cm thick followed by 0.0510 cm thick layer of PMMA which is not a part of the waterproof sleeve mentioned above. For in-water calculation, a waterproof sleeve was considered as a layer of PMMA with 0.1 cm thickness which covers the NE2571 ion chamber.

4.2 Exradin A16 Ion Chamber

The Exradin A16 ion chamber is a micro chamber which is capable of measuring extremely small field sizes. Figure 4.2 shows the geometry of the Exradin A16 ion chamber.

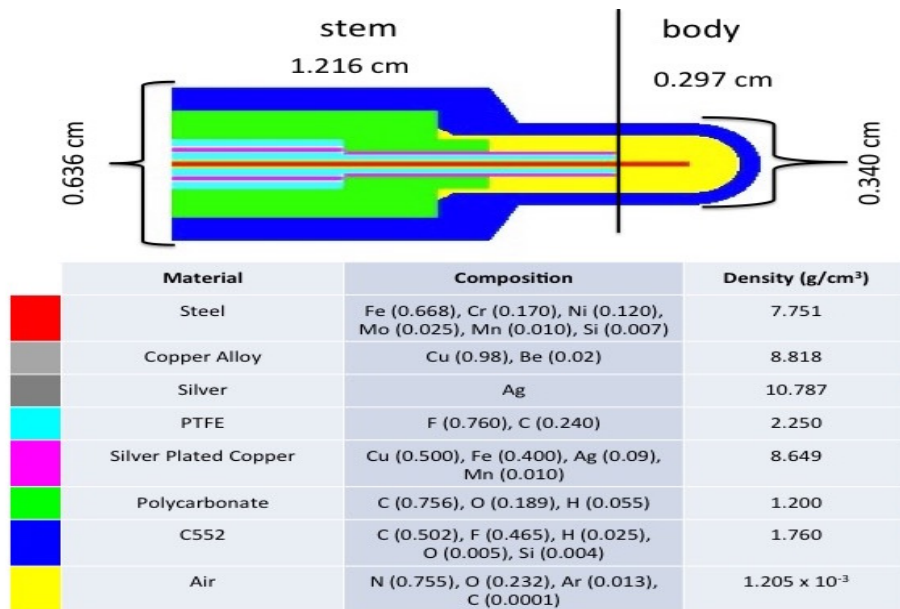


Figure 4.2: Same as fig 4.1 but for Exradin A16 ion chamber. Copper and silver are not visible in this resolution. The vertical black line separates detector's body from the stem.

The TG-61 protocol⁴ provides no information about this ion chamber and its correction factors. This was a motivation of studying this ion chamber for a range of kilovoltage x-ray beams. As well, a previous study by Muir and Rogers²² which indicated problems because of the high-Z electrode and suggested farther investigation.

The Exradin A16 ion chamber consists of a stem and body with 0.00917 cm^3 air cavity volume. The end of the stem is a cylinder with 0.881 cm length composed of steel, copper, silver, polytetrafluoroethylene (PTFE), braided silver plated copper, polycarbonate (PCARB), and C552 with radii of 0.01148 cm, 0.01435 cm, 0.01481 cm, 0.04953 cm, 0.06604 cm, 0.2223 cm and 0.318 cm respectively. Over a distance of 0.071 cm, the radius of C552 shrinks to 0.170 cm. Note that there is also an inactive air region in the stem where dose is not scored and has a length of 0.335 cm. The body is composed of a cylindrical and hemispherical sections. The cylinder part of the body is made of five radial layer of steel, copper, silver, air, and C552. It has a length of 0.127 cm. The radii of these layer are 0.0115 cm, 0.0144 cm, 0.0148 cm, 0.119 cm, and 0.170 cm respectively. The hemispherical section is made of air and C552 with respective outer radii of 0.119 cm and 0.170 cm.

4.3 Exradin W1 Plastic Scintillator Detector

The Exradin W1 detector is a plastic scintillator based detector which has a simpler structure compared to the two ion chambers. The Exradin W1 detector is made of water equivalent materials which produce less perturbation in the water phantom in comparison to the Exradin A16 and NE2571 ion chambers. The characteristics of plastic scintillator detector (PSD) have been studied for high energy beams where the response of a PSD was found to be energy independent over the range of 0.3 MeV to 2 MeV²³. The Exradin W1 plastic scintillator was considered in this thesis to study its behaviour for kilovoltage x-ray beams.

The geometry and materials of the Exradin W1 are shown in fig 4.3. The scintillator fiber is made of polystyrene surrounded by a plastic enclosure of ABS and a polyimide stem. It has a 0.00235 cm^3 sensitive volume with a cylinder shape. The Exradin W1 consists of a stem and body with length of 3.454 cm and 0.694 cm respectively. The stem is made of three cylinders attached to each others with a length of 2.858 cm, 0.114 cm, and 0.482 cm. The cylinder with 2.858 cm length is composed of PMMA,

Polyethylene, EPOXY, and Polyimide with respective radii of 0.05 cm, 0.112 cm, 0.132 cm, and 0.142 cm. The 0.112 cm long cylinder consists of PMMA, EPOXY, and Polyimide with 0.05 cm, 0.132 cm, and 0.142 cm radii respectively.

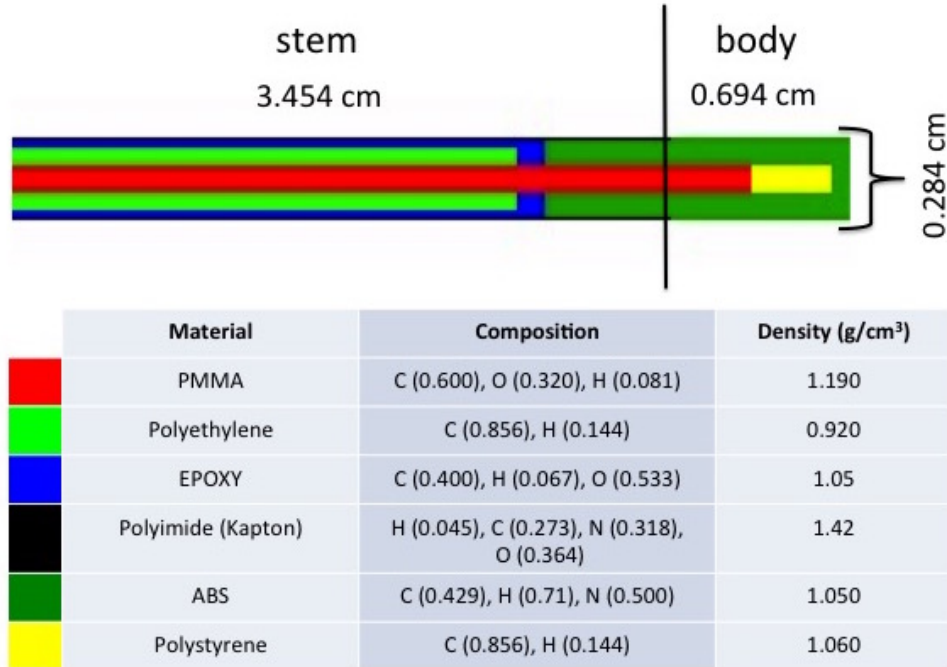


Figure 4.3: Same as fig 4.2 but for Exradin W1 PSD. The vertical black line separates detector's body from the stem.

The last part of the stem, which is attached to the body, is made of PMMA with a radius of 0.05 cm. It is surrounded by ABS and Polyimide with 0.132 cm and 0.142 cm radius. Right after the stem, over a distance of 0.318 cm, PMMA with a radius of 0.05 cm is surrounded by ABS with a radius of 0.142. It is followed by a cylinder with 0.300 cm length made of Polystyrene and ABS with 0.05 cm and 0.142 cm radii respectively. The last part is a ABS cylinder with a radius of 0.142 cm and length of 0.076 cm.

Note that the stem of the Exradin W1 plastic scintillator starts at 0.318 cm away from the sensitive cavity based on the company terminology as opposed to the NE2571 and Exradin A16 ion chambers in which stem starts right after the sensitive volume.

Chapter 5

Geometries and Monte Carlo simulations

5.1 Monte Carlo Method

The Monte Carlo method is a well known computational algorithm to calculate quantities which are too complicated to solve analytically. It generates random numbers and uses probabilistic models. This method has been used widely in the Medical Physics area for problems such as the calculation of dose distributions for a modern treatment planning system.

A typical radiation transport Monte Carlo simulation employs individual differential cross-sections for the interactions of particles in matter; the particle's trajectories can be produced using uniformly distributed random numbers. The goal of running a Monte Carlo simulation is to calculate the averaged macroscopic distribution of quantities such as absorbed energy in the medium. The nature of this averaging follows the Gaussian distribution of the averaged quantity. This distribution gives us an estimate of the mean (i.e. desired quantity such as dose) within the standard deviation, s , which decreases by increasing the number of particles (i.e histories) in the Monte Carlo simulation,

$$s \propto \frac{1}{\sqrt{N}} \quad (5.1)$$

where N is the number of histories in the simulation.

Another capability of the Monte Carlo method is to calculate quantities that can not be measured in an experiment such as the portion of particles undergoing specific interactions or the number of primary or scattered particles in the simulation.

5.2 The EGSnrc code system

The EGSnrc (Electron-Gamma-Shower) code system²⁴ is the upgraded version of the EGS4 code system¹². EGSnrc was developed by the National Research Council Canada. EGSnrc includes improvements of the charged particle transport and atomic scattering cross-section data²⁵. It also implements a C++ geometry library²¹ which is a powerful tool for the simulation of complex geometries and particle sources. There are a variety of user codes available in the EGSnrc code system such as DOSRZnrc, FLURZnrc²⁰, and egs_chamber. One can define different elements of the simulation for a specific user code; for example, the geometry of an ionization chamber as well as a collimated, point or parallel beam source.

This research mostly utilized the egs_chamber user code because of its ability to define complex geometries. DOSRZnrc and FLURZnrc were also used to obtain depth-dose curves, e.g., fig 3.3, and the particle fluence inside the cylindrical air cavity (see below).

5.2.1 egs_chamber user code

The egs_chamber user code is a powerful EGSnrc user code for the simulation of complex geometries and particle sources using the C++ class library, egspp²¹, which provides a geometry package for simulating a wide range of structures and a set of particle sources for simulating many of sources that are available with other user codes (e.g., DOSRZnrc).

Several features in the C++ library are used to define the input file of the egs_chamber user code. These features are as follows:

- EGS-ConeStack which models a series of cones stacked together to form a complex structure such as the ionization chamber detectors used in this study (i.e., NE2571 and Exradin A16).
- EGS-Spheres that can produce spherical geometries such as the tip of the Exradin A16 ionization chamber.

- EGS-Gunion to combine several geometries and create one geometry where the priority for each of the individual sub-geometries is defined.
- EGS-Box to model a water phantom.
- EGS-envelope to inscribe a smaller geometry into a larger one like the detector into a phantom or an enhancement region.

The EGS-Collimated-Source has been used for the particle source to define a square shaped collimator (which determines the field size of the beam on the surface of a phantom) using the EGS-Rectangle library.

DOSRZnrc and FLURZnrc use polar coordinates to define a geometry, i.e., one is able to define cylindrical shaped geometries. A cylindrical water phantom with 17 cm radius and 30 cm length is used to approximate the water phantom defined in the egs_chamber user code (i.e., $30 \times 30 \times 30 \text{ cm}^3$ box). A circular equivalent field size beam is considered in DOSRZnrc and FLURZnrc user codes instead of the square field size beam used in the egs_chamber user code. The relation between two equivalent field sizes is

$$\pi R^2 = A^2 \quad (5.2)$$

where R and A are the radius and side of the circular and squared field sizes respectively.

5.3 Variance reduction techniques (VRT)

To design a Monte Carlo algorithm two important parameters need to be considered; statistical uncertainty and the time required for the accomplishment of the simulation. One can decrease the statistical uncertainty by increasing the sample size, known as number of histories, which is probably the most straightforward method despite the fact that it increases the required time to complete the simulation as well; but in reality, timing in a simulation must be practical and has its limitations depending on one's priorities. The efficiency of a Monte Carlo simulation can be defined as

$$\epsilon = \frac{1}{s^2 T} , \quad (5.3)$$

where ϵ is the efficiency, s is the statistical uncertainty on the calculated quantity, and T is the computational time. Variance reduction techniques are powerful methods to enhance the efficiency of a Monte Carlo algorithm using adjustments to the probability distributions to produce more precise results without biasing them.²⁶

In this study, photon cross-section enhancement and range rejection techniques are used to optimize the efficiency of the simulations.

5.3.1 Photon cross-section enhancement technique (XCSE)

Calculation of the absorbed dose can take too much time especially once the scored region is so small that one needs to increase the density of the interactions near the region where absorbed dose is scored. In the photon cross-section enhancement technique, the user can keep the number of transported photons and increase the number of electrons set in motion by incident photons with a parameter that can be defined separately for each region. This parameter should be chosen to have the most efficient simulation which depends on the geometries and the materials being used.

This technique is also used in other user code of EGSnrc such as CAVRZnrc and DOSRZnrc but the advantage of the egs_chamber user code is that the user can set up different values for the parameter in various regions while it is not possible with the other user codes.

This technique improves the efficiency for the calculation of the detector dose at 2 cm depth in the water phantom by maximum ratio of 103, 8, and 117 for the Exradin W1 plastic scintillator, Exradin A16, and NE2571 ionization chambers respectively. The efficiency improvement for the Exradin A16 ion chamber is smaller than two other detectors which is most likely due to the large number of secondary electrons produced by photoelectric interactions of photons with the high Z materials in the Exradin A16's electrode. These secondary electrons slow down the Monte Carlo simulation. To obtain the best number for photon cross-section enhancement, several simulations were run each time with a different photon cross-section enhancement number such as 64, 128, 256, 512, or 1024. Efficiencies were compared with each other to obtain the maximum improvement in the calculation efficiency for each detector. The best photon cross-section enhancement numbers were 1024, 512 and 512 for Exradin W1 plastic scintillator, Exradin A16, and NE2571 ionization chambers respectively.

5.3.2 Range rejection and Russian roulette (RR) technique

The second technique used in this study, is the range rejection technique (rr). The idea behind it is to discard charged particles if the ranges or energies of the particles are not enough to pass the nearest boundary. This technique does not require additional calculation since the ranges of the particles and the distances from the closest boundary are known at each step in the EGSnrc simulation. The only problem is that it also ignores the possible radiation from the discarded charged particle such as bremsstrahlung or annihilation radiation; hence the range rejection technique is not a true variance reduction technique since in principle it introduces a bias to the final results.

To overcome the bias problem, a Russian Roulette (RR) game was implemented as part of the range rejection technique. Generally speaking, once a charged particle is selected to be discarded through the range rejection technique, Russian Roulette is played with a survival probability which is set by the user. A surviving particle carries a high statistical weight (called a fat particle) which has an inverse relation with the survival probability of the Russian Roulette game. This statistical weight contributes to the calculation of the quantity of interest (e.g., absorbed dose) and represents the radiative energy which was ignored by the range rejection technique.

The combination of the rr and RR techniques increased the efficiency of the Monte Carlo simulations in this study by the maximum ratio of 2, 3.4, and 3.3 for the Exradin W1 plastic scintillator, Exradin A16, and NE2571 ionization chambers respectively when calculating the detector dose at 2 cm depth in a water phantom. Note that for the calculation of the air kerma, range rejection and Russian Roulette techniques are irrelevant since there is no charged particle transport.

5.4 Air-Kerma calculation

The $P_{Q, cham}$ calculation, either using the direct method (see eqn 2.5, page 8) or the indirect method (see eqn 2.15, page 10), requires air kerma calculations in the air ($K_{air}^{free\ in-air}$) and in the water phantom (K_{air}^w) for two reasons. First, the detector is calibrated in terms of the air kerma free in-air, based on eqn 1.1 (page 1); second, the air kerma in the water phantom is needed to obtain the water kerma in a water phantom using eqn 2.6 (page 8). The TG-61 protocol recommends a depth of 2 cm in the water phantom as a reference depth ($z_{ref} = 2$ cm). This study considers the SSD (source

surface distance) to be equal to 50 cm for all simulations and the water phantom is $30 \times 30 \times 30 \text{ cm}^3$.

To calculate the water kerma and air kerma at the reference point, a cylindrical cavity was employed. To find the best cavity size, water kerma and air kerma were calculated using a cylindrical cavity with 1 mm diameter and different thickness between 1 mm to 5 mm. PCUT was set to 1 keV (photons with energy less than 1 keV deposit their energy in the local region) and electron transport was off. The results are shown in fig 5.1.

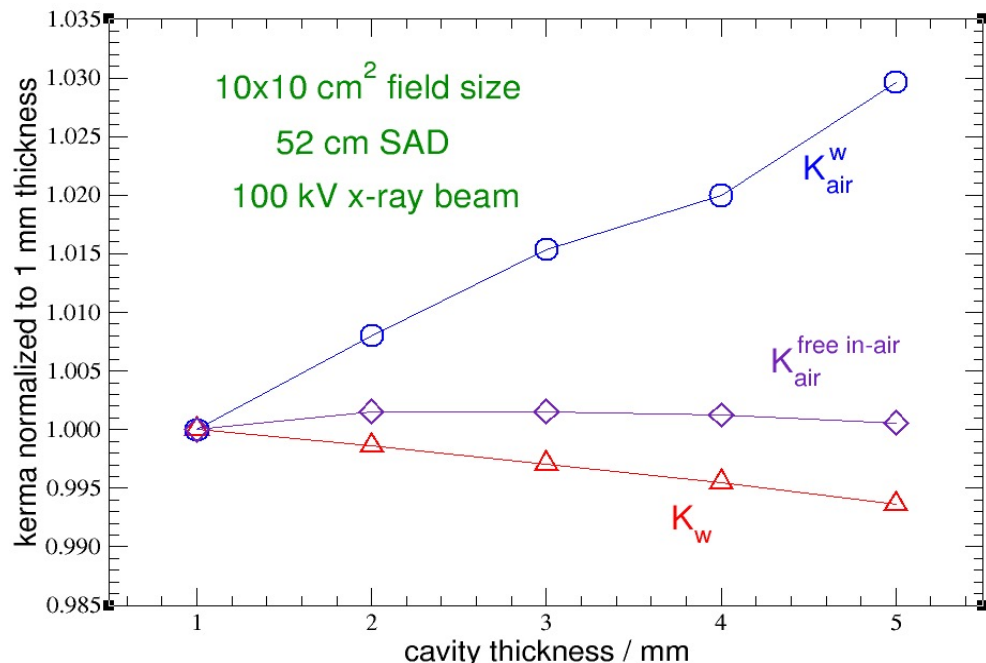


Figure 5.1: The variation of K_{water} , K_{air}^w , and $K_{air}^{free\ in-air}$ with thickness of the cylindrical cavity for 100 kV x-ray beam. The values are normalized to the result of the cavity with 1 mm thickness. The statistical uncertainties are 0.1%.

Fig 5.1 shows a 3% increase for the K_{air}^w values with an increase of the cavity thickness. As opposed to K_{air}^w , the values of K_{water} decrease by 0.6% as the thickness of the cavity increases. The variation of the $K_{air}^{free\ in-air}$ values with cavity thickness is negligible; hence $K_{air}^{free\ in-air}$ does not depend on the thickness of the cylindrical air cavity over the range of 1 mm to 5 mm thickness.

Fig 5.1 clearly indicates that one should be careful about the thickness of the cavity in order to obtain the water kerma and air kerma at the reference point of measurement in the water phantom. In this thesis, a cylindrical cavity with 1 mm thickness is

employed to achieve this goal while Seuntjens and Verheagen³ used a cavity with outer dimensions of the detector to calculate the $P_{Q, cham}$ correction factor.

The ratio for water to air of the mean mass energy absorption coefficients in the water phantom, $\left[\left(\frac{\bar{\mu}_{en}}{\rho} \right)_{air}^w \right]_{water}$, is presented in the TG-61 protocol^{4, 19} for x-ray beams with different HVLs (0.1 mm Cu to 5 mm Cu HVLs).

The ratio for water to air of the means mass energy absorption coefficients was studied in this thesis using following equation,

$$\left[\left(\frac{\bar{\mu}_{en}}{\rho} \right)_{air}^w \right]_{water} = \frac{K_{water}}{K_{air}^w}, \quad (5.4)$$

where K_{water} and K_{air}^w are the water kerma to the cylindrical water cavity and air kerma to the same cavity full of air in the water phantom respectively. The geometries for calculation of these two quantity are shown in fig 5.2. The electron transport was off and photons followed down to 1 keV, i.e., PCUT = 0.001 MeV.

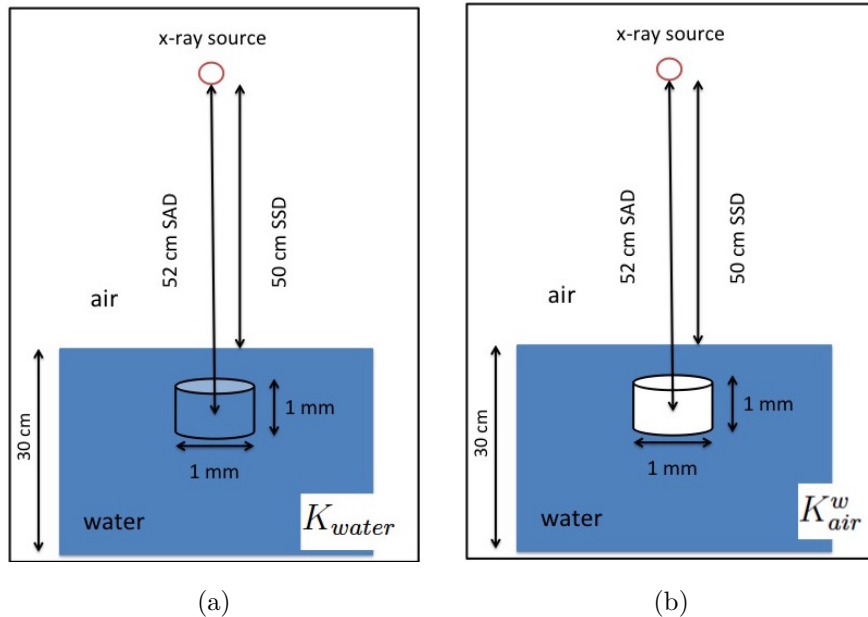


Figure 5.2: The geometry for the calculation of the water kerma, K_{water} (a) and the air kerma, K_{air}^w (b). Note that the air between x-ray source and the water phantom had been considered in the simulation of x-ray spectra using SpekCalc software.

Figs 5.3 and 5.4 shows the variation of $\left[\left(\frac{\bar{\mu}_{en}}{\rho} \right)_{air}^w \right]_{water}$ with HVL and depth in the water phantom for six different beam qualities (x-ray tube 100 kV - 300 kV).

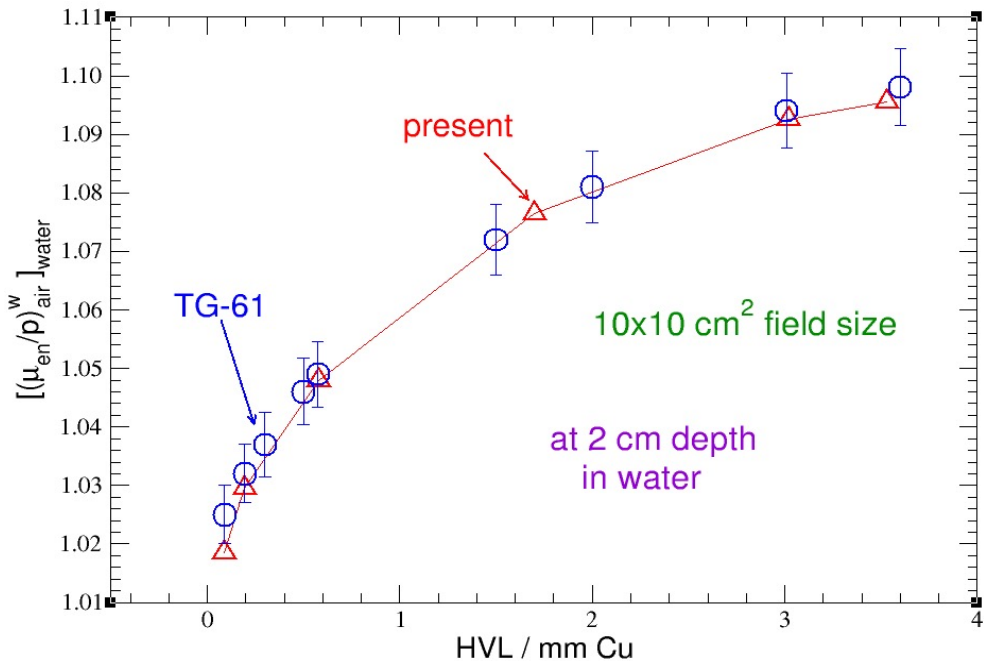


Figure 5.3: The variation of $\left[\left(\frac{\bar{\mu}_{en}}{\rho} \right)_{air}^w \right]_{water}$ with HVL in this thesis (present) and in the TG-61 protocol at 2 cm depth in the water phantom for 10 cm field size. The statistical uncertainties are 0.1% in this thesis and 0.5% for the values from TG-61.

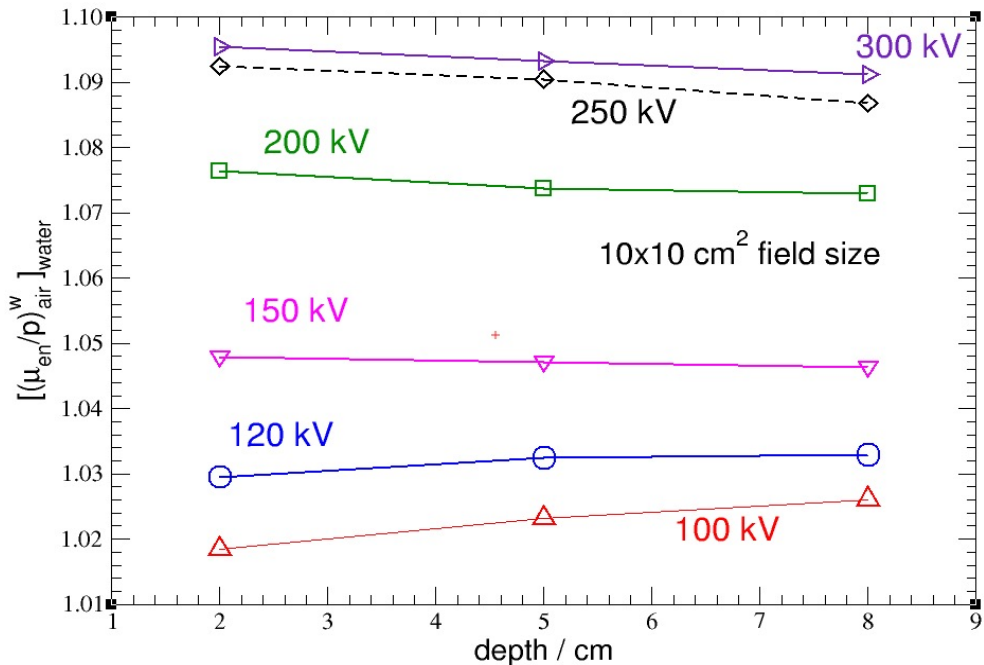


Figure 5.4: The variation of $\left[\left(\frac{\bar{\mu}_{en}}{\rho} \right)_{air}^w \right]_{water}$ with depth in the water phantom for six different beam qualities (x-ray tube potentials 100 kV - 300 kV). The statistical uncertainties are 0.1%.

The values of the $\left[\left(\frac{\bar{\mu}_{en}}{\rho} \right)_{air}^w \right]_{water}$ in this thesis at 2 cm depth in the water phantom are in agreement with those in the TG-61 protocol. The variation of the $\left[\left(\frac{\bar{\mu}_{en}}{\rho} \right)_{air}^w \right]_{water}$ with depth is up to 0.7% for the 100 kV x-ray beam (HVL: 0.088 mm Cu) as depth increases from 2 cm to 8 cm in the water phantom.

Fig 5.5 shows the geometry for the calculation of air kerma free in-air and in the water phantom.

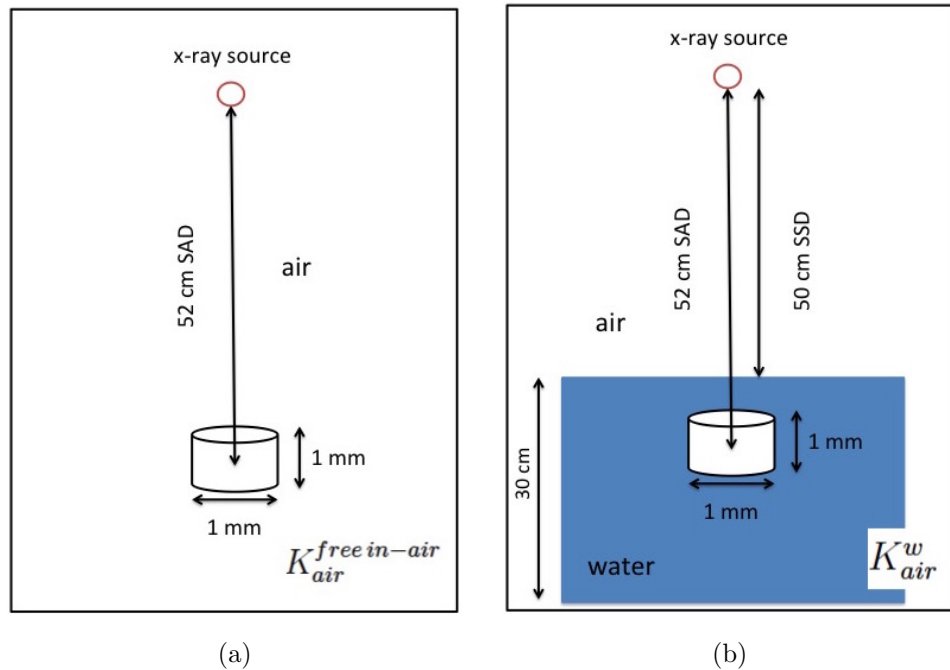


Figure 5.5: The geometry for the calculation of the air kerma free in-air, $K_{air}^{free\ in-air}$ (a) and in-water phantom, K_{air}^w (b). Note that the air between x-ray source and the cylindrical air cavity had been considered in the simulation of x-ray spectra using SpekCalc software.

The air kerma for free in-air and in-water calculations were scored using the egs_chamber user code with no electron transport in the cylindrical cavity full of air with 1 mm height and 1 mm diameter as shown in fig 5.5. Note that the centre (not the surface) of the cylindrical air cavity is at the reference depth (2 cm depth) in the water phantom. The kerma calculation requires only photon transport in the Monte Carlo simulations; for this reason, the electron transport was switched off using a high value of ECUT (1 MeV which is greater than the highest possible total energy of an electron. For example for the 300 kV x-ray beam, the maximum total energy of an electron is 811 keV) for all regions in the simulations. Photon cross-section enhancement was set

at 3,200,000 for the air cavity to maximize the efficiency (see section 5.3, page 23) of the Monte Carlo simulations for the air kerma calculations in-air and in-water phantom. Photon cross-section enhancement for air kerma calculations is greater in comparison to the detector dose calculations since size of the air cavity for air kerma calculations is much smaller than the detector's cavity. The smaller air cavity requires more interactions in the medium to obtain a result with low statistical uncertainty. In addition, electron transport is not off for the calculation of the detector's dose as opposed to the air kerma calculation. Secondary electrons from detector's wall and electrode contribute to the detector dose, hence there are more interactions in the detector air cavity and lower photon cross-section enhancement is required in comparison to the air kerma calculation.

The ratio of K_{air}^w to $K_{air}^{free\ in-air}$ variation with depth is shown in figs 5.6, 5.7, and 5.8 for 10 cm, 5 cm, and 1 cm field sizes respectively.

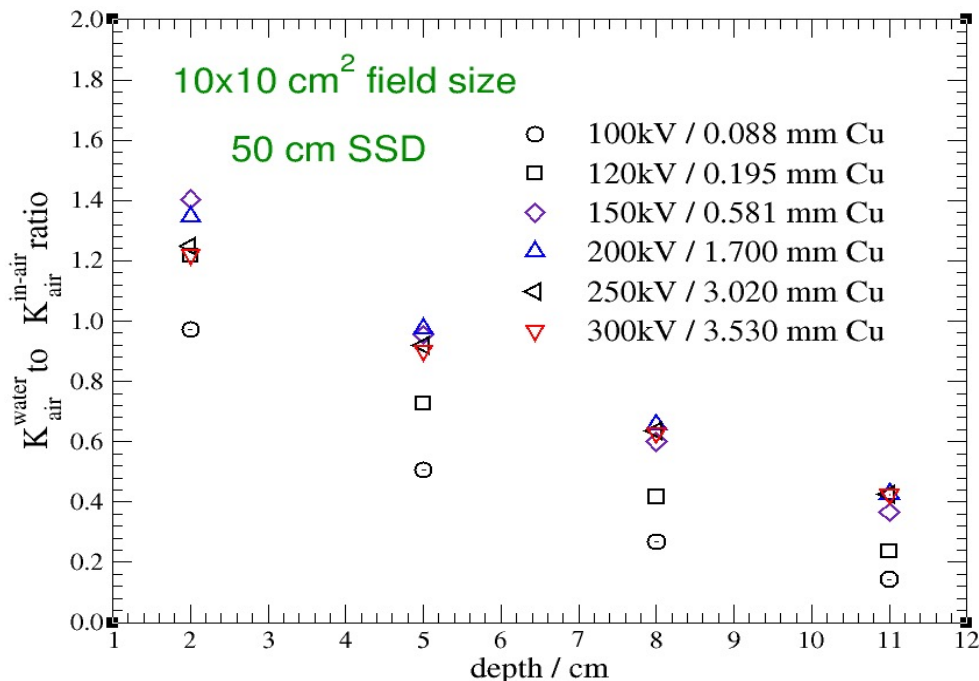


Figure 5.6: The ratio of the air kerma in-water to air kerma free in-air calculations with depth for six beam qualities with a 10 cm field size. The statistical uncertainties are less than 0.1%.

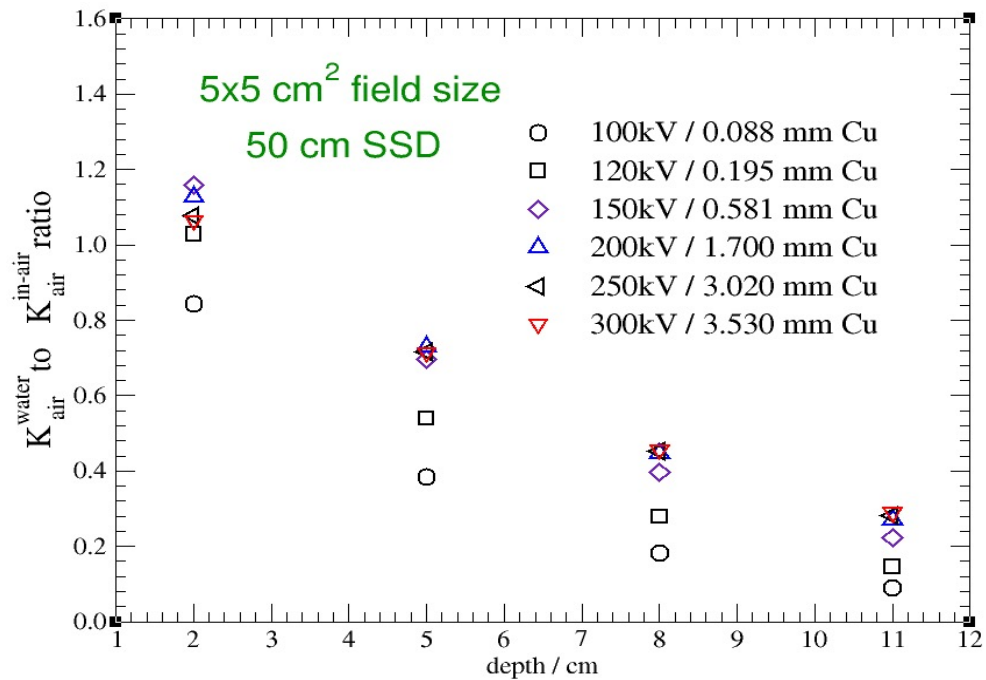


Figure 5.7: Same as fig 5.6 but for 5 cm field size beams.

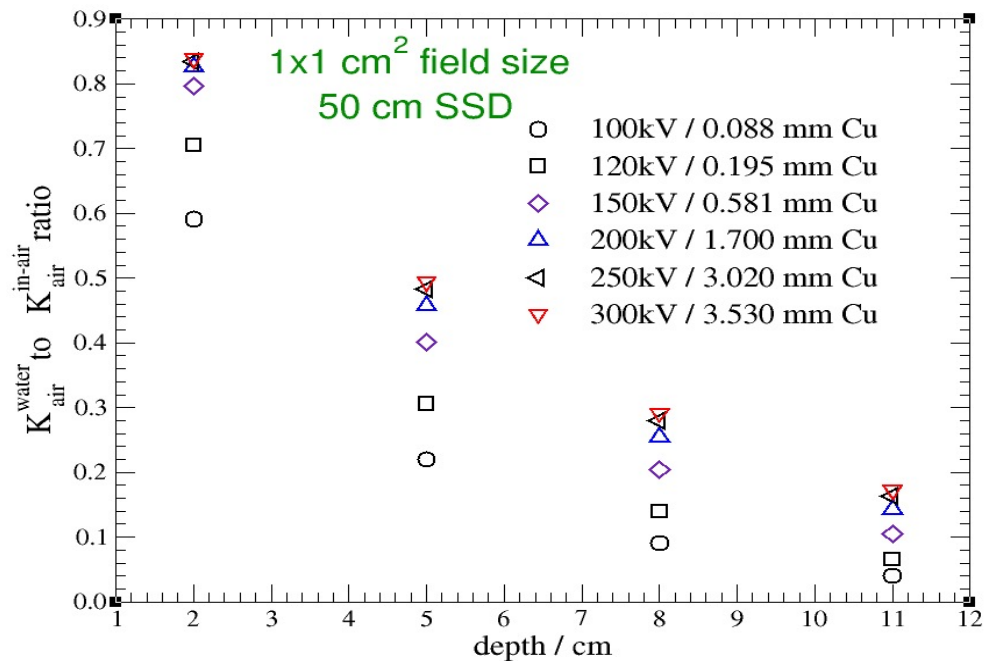


Figure 5.8: Same as fig 5.6 but for 1 cm field size beams.

Note that $K_{\text{air}}^{\text{free in-air}}$ is calculated at the reference depth (52 cm source axis dis-

tance (SAD)) since the detector is calibrated at the same reference point while the air kerma in-water (K_{air}^w) is calculated at 2, 5, 8, and 11 cm depth with 50 cm source surface distance (SSD). The statistical uncertainties on the ratios are less than 0.1 % for all depth and field sizes.

The variation of $\frac{K_{air}^w}{K_{air}^{free\ in-air}}$ with depth reveals the combination of attenuation, scattered and $\frac{1}{r^2}$ effects on the air kerma in-water calculation (see 5.5 (b)). In fig 5.6 at 2 cm depth in the water phantom, the ratios of $\frac{K_{air}^w}{K_{air}^{free\ in-air}}$ are larger than unity except for 100 kV x-ray (0.088 mm Cu) showing the effect of scattered photons is more important than the attenuation of primary photons at the 2 cm depth in the water phantom while for 100 kV x-ray beam (0.088 mm Cu) this is vice versa. Note that at 2 cm depth in the water phantom, $\frac{1}{r^2}$ variation has no effect since SAD equals 52 cm for the calculation of K_{air}^w and $K_{air}^{free\ in-air}$. By increasing the depth, the effect of $\frac{1}{r^2}$ appears since the SAD for the K_{air}^w calculation increases with depth but the $K_{air}^{free\ in-air}$ is calculated at 52 cm SAD. The $\frac{1}{r^2}$ effect causes 27% decrease going from 2 cm to 11 cm depth.

Figs 5.7 and 5.8 show the $\frac{K_{air}^w}{K_{air}^{free\ in-air}}$ versus depth in the water phantom for 5 cm and 1 cm field sizes respectively.

All the values of $\frac{K_{air}^w}{K_{air}^{free\ in-air}}$ at 2 cm depth decrease by about 20% for the 5 cm field size and another 38% for the 1 cm field size compared with the 10 cm field size (fig 5.6). This shows that the effect of scattered photons on the central axis for 5 cm and 1 cm field sizes is less than for the 10 cm field size.

5.5 Detector dose calculation

The air kerma calculations were discussed in the previous section; detector dose in air and in the water phantom are also needed for the $P_{Q, cham}$ calculation as mentioned in section 2.4 (page 7). The NE2571 and Exradin A16 ion chamber geometries as well as the geometry of the Exradin W1 plastic scintillator were defined in detail for the simulations of this section in chapter 4 (page 16).

The geometries for the calculations of dose to the detector cavity free in-air (D_{cav}^{air}) and in the water phantom (D_{cav}^w) are shown in fig 5.9.

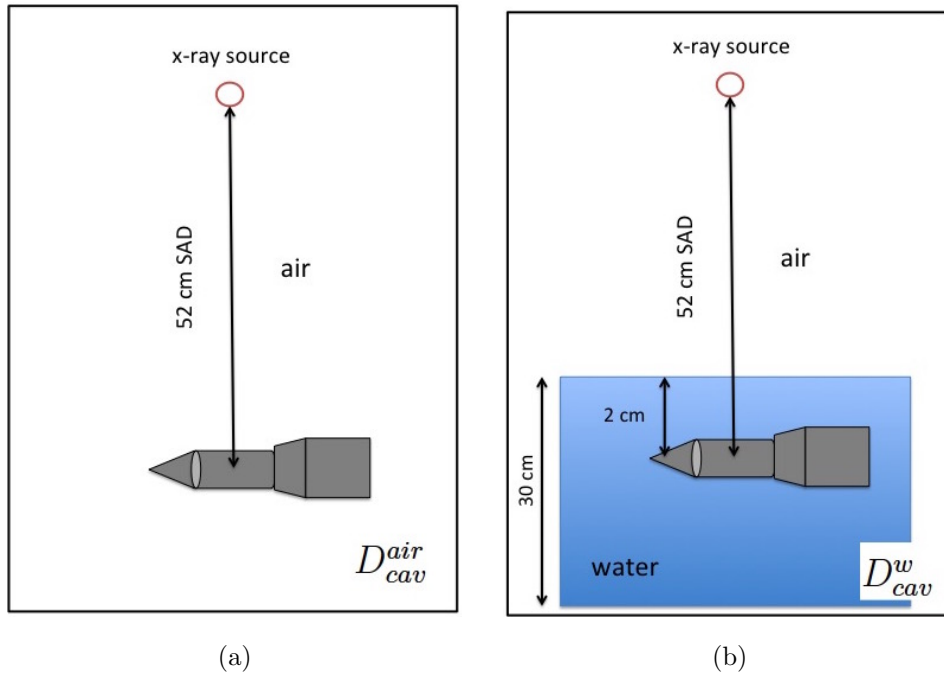


Figure 5.9: The geometry for the detector dose calculation in the air (a) and in the water phantom (b). Note that the air between source and the detector was considered in the spectrum simulation using SpekCalc software.

The detector in fig 5.9 is not a specific detector and can be the NE2571 ion chamber, Exradin A16 ion chamber, or Exradin W1 plastic scintillator. The centre of the sensitive volume of the detector is placed at 52 cm away from the collimated x-ray point source for the in-air and in-water calculations. Similar to the calculation of the air kerma in air, the detector dose for the in-air case is calculated only at 52 cm SAD but in the in-water phantom, it is calculated at 2, 5, 8, and 11 cm depth.

To increase the efficiency of the simulation, the photon cross-section enhancement was employed and the range rejection technique with Russian roulette were used (see section 5.3.2, page 24). The ECUT value was 0.521 MeV (electrons with total energy less than 0.521 MeV deposit their energy in the local region) and the PCUT value was 0.01 MeV (photons with energy less than 0.01 MeV deposit their energy in the local region). This study did not consider the 1 cm field size beam for the NE2571 ionization chamber since it does not cover the NE2571 ion chamber's sensitive air cavity which is 2.40 cm in length.

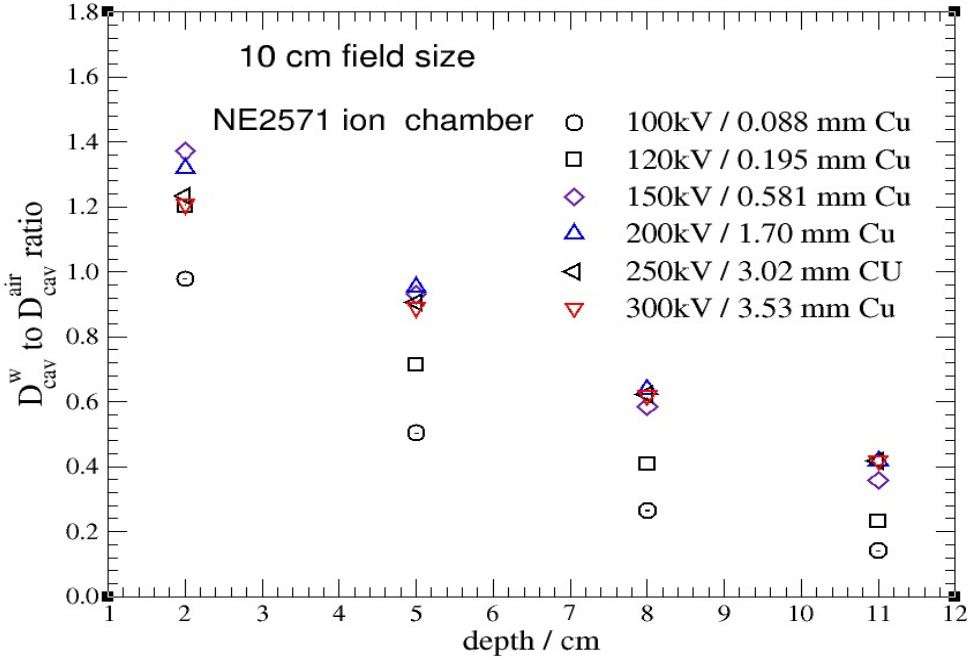


Figure 5.10: The ratio of the NE2571 ion chamber dose in-water to the in-air calculation with depth for the six beam qualities for the 10 cm field size. The statistical uncertainties are less than 0.1%

Fig 5.10 shows the ratio of D_{cav}^w (detector dose for the in-water calculation) to D_{cav}^{air} (detector dose for the in-air calculation) for the NE2571 ionization chamber in the 10 cm field size beam. For beams at 120 kV and above, the ratios of D_{cav}^w to D_{cav}^{air} are larger than unity at 2 cm depth in the water phantom showing that the effect of scattered particles dominates the attenuation effect while it is opposite for the 100 kV x-ray beam (0.088 mm Cu); as a result, the value of $\frac{D_{cav}^w}{D_{cav}^{air}}$ is less than unity.

Note that the values in fig 5.6 looks the same as fig 5.10 for a specific beam quality and depth. This indicates that the $P_{Q,cham}$ correction factor is expected to be close to unity for the NE2571 ion chamber.

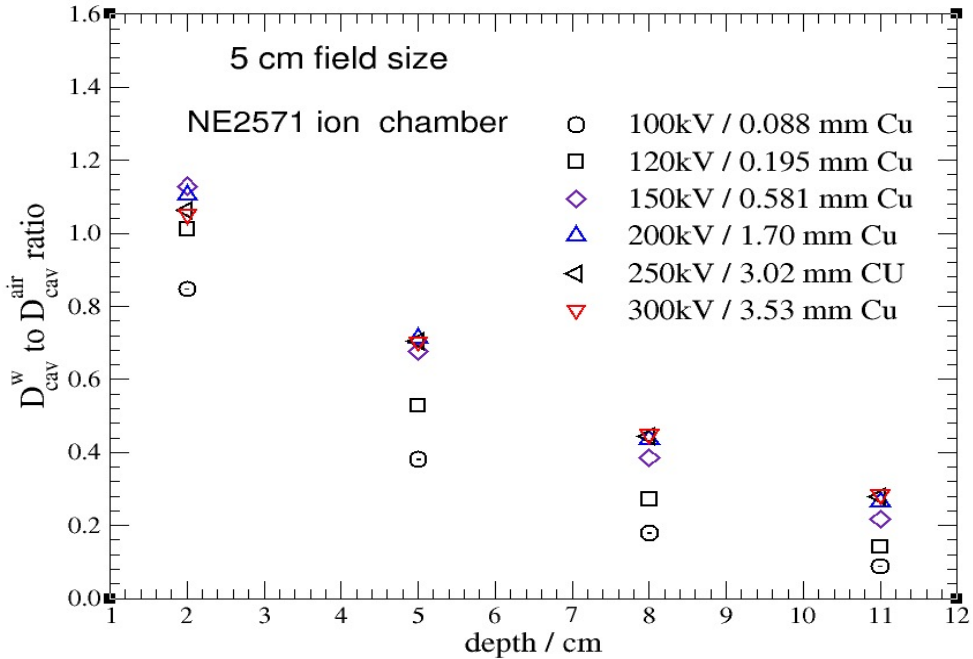


Figure 5.11: Same as fig 5.10 but for 5 cm field size.

Fig 5.11 shows the variation of $\frac{D_{cav}^w}{D_{cav}^{air}}$ versus depth for 5 cm field size. Comparing the 10 cm field size (fig 5.10) with 5 cm field size results (fig 5.11), one can see a downward shift for the values of $\frac{D_{cav}^w}{D_{cav}^{air}}$ from 10 cm field size to 5 cm field size which is related to the decreasing effect of scattered particles in the detector dose at smaller field size which is similar to the air kerma results in figs 5.7 and 5.8. The effect of the $\frac{1}{r^2}$ law (r is the distance between the source and the reference point of measurement) comes into play as the depth increases.

The values of the $P_{Q,cham}$ correction factor is expected to be close to unity for 5 cm field size beam since the values in fig 5.7 and 5.11 are close to each other for a specific beam quality and depth.

The variation of $\frac{D_{cav}^w}{D_{cav}^{air}}$ with depth for the Exradin A16 ion chamber is also calculated for 6 different x-ray beams. Since the sensitive air cavity of this ion chamber is small enough (i.e., 0.246 cm length), the 1 cm field size is also considered (fig 5.14) as well as 5 cm (fig 5.13) and 10 cm (fig 5.12) field sizes.

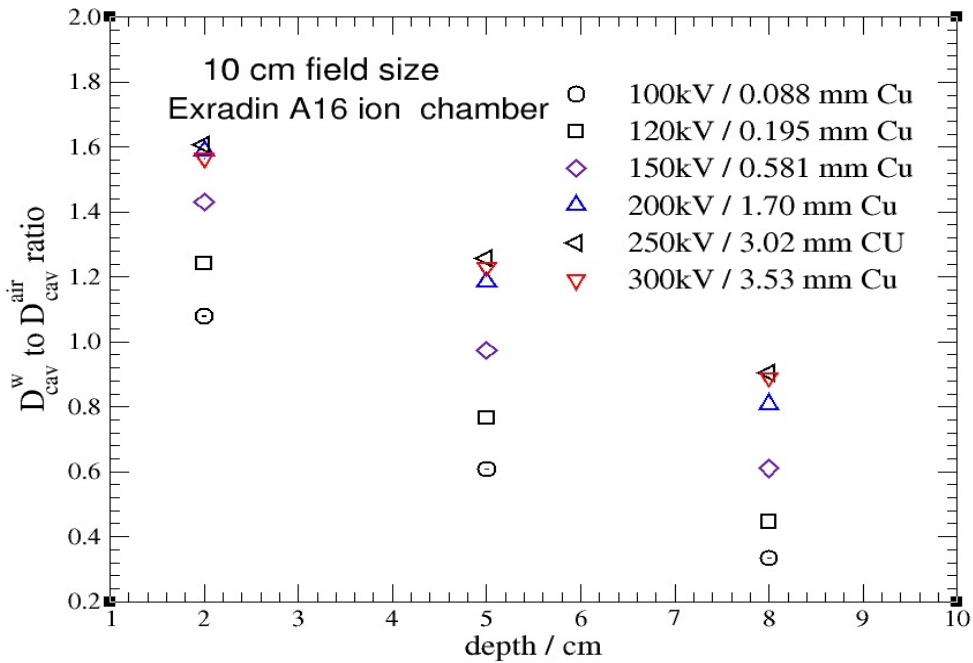


Figure 5.12: The ratio of the Exradin A16 ion chamber dose in-water to the in-air calculation with depth for the six beam qualities for the 10 cm field size. The statistical uncertainties are less than 0.1%.

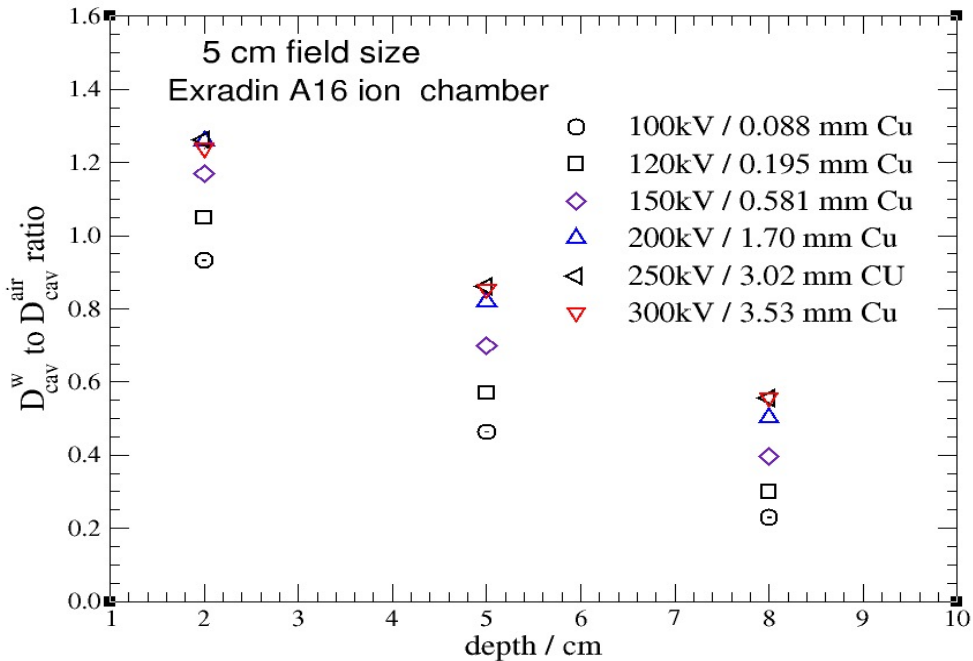


Figure 5.13: Same as fig 5.12 but for 5 cm field size beam.

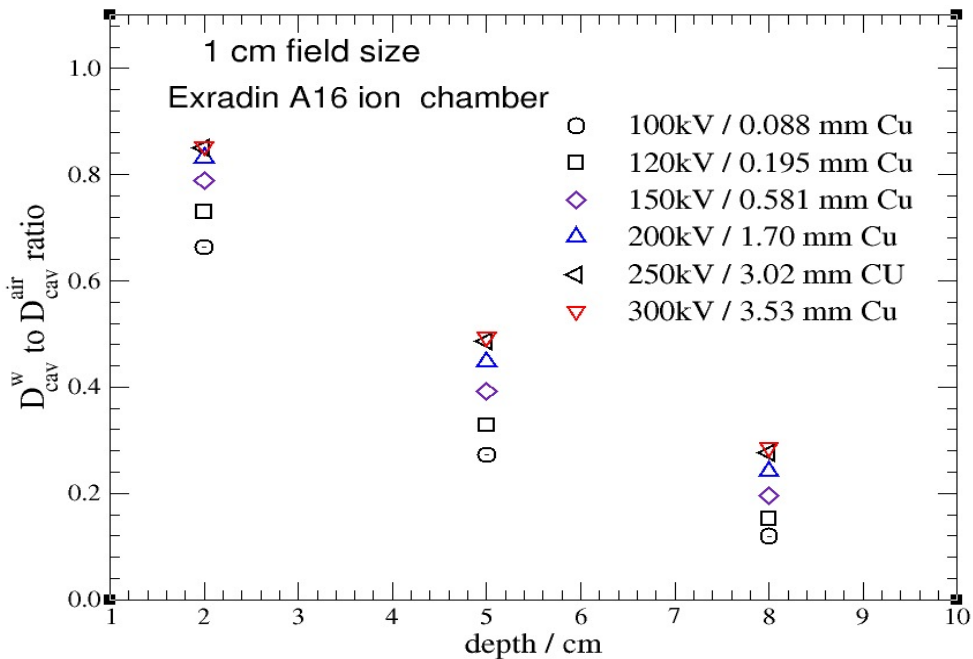


Figure 5.14: Same as fig 5.13 but for 1 cm field size beam.

The main difference between the ratio of D_{cav}^w to D_{cav}^{air} for the Exradin A16 ion chamber compared to for the NE2571 ion chamber is that this ratio is larger for the Exradin A16 ion chamber for all depths .This difference is related to the secondary electrons produced by the electrode of the Exradin A16 ion chamber due to the photo-electric interaction between photons and the high-Z materials in the Exradin A16 ion chamber's electrode. These secondary electrons contribute to the dose at the air cavity of the Exradin A16 ion chamber and increase the amount of dose. This will be discussed in chapter 6 (page 53).

Also, the maximum and minimum values of $\frac{D_{cav}^w}{D_{cav}^{air}}$ between the 6 different x-ray beams at 2 cm depth in the water phantom, are different by less than 40% for the NE2571 ion chamber while it is about 50% for the Exradin A16 ion chamber for the 10 cm field size beam.

Finally the values of $\frac{D_{cav}^w}{D_{cav}^{air}}$ versus depth for Exradin W1 plastic scintillator are shown for 10 cm (fig 5.15), 5 cm (fig 5.16), and 1 cm (fig 5.17) field sizes.

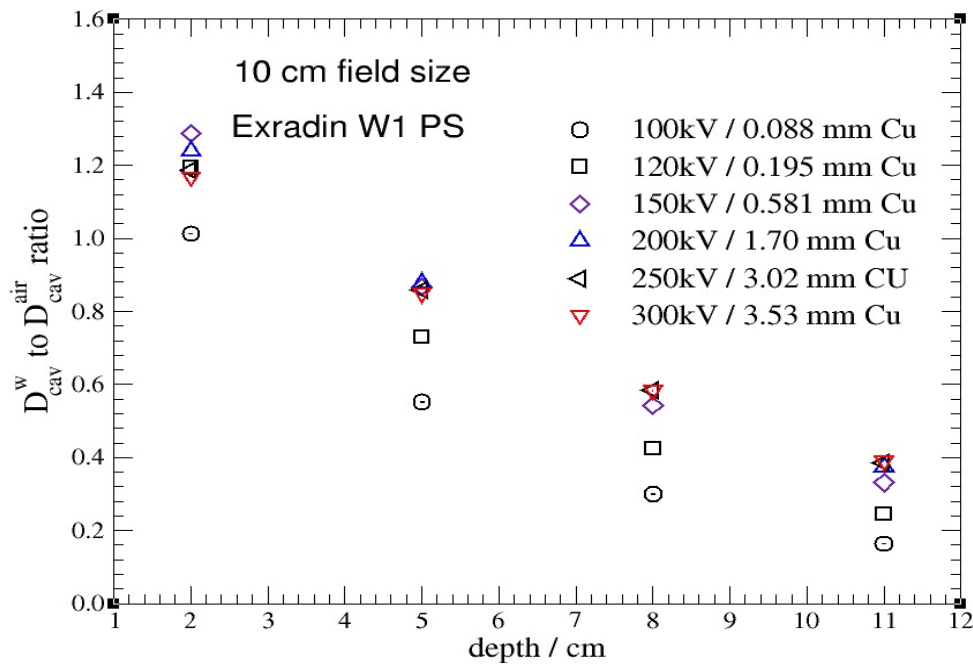


Figure 5.15: The ratio of the Exradin W1 plastic scintillator dose in-water to the in-air calculation with depth for the six beam qualities for the 10 cm field size beam. The statistical uncertainties are less than 0.1%.

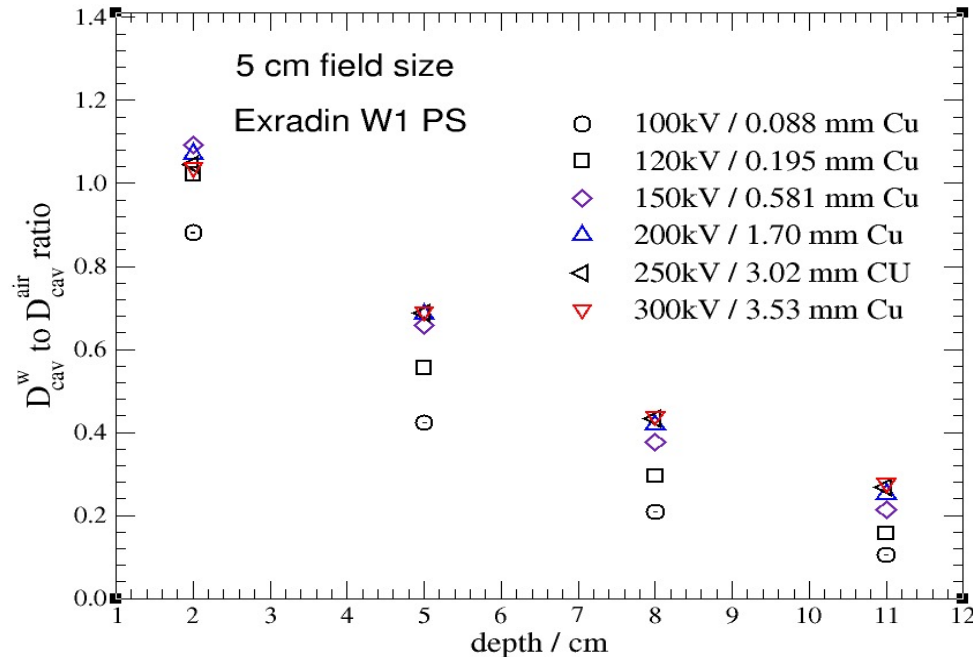


Figure 5.16: Same as fig 5.15 but for 5 cm field size beam.

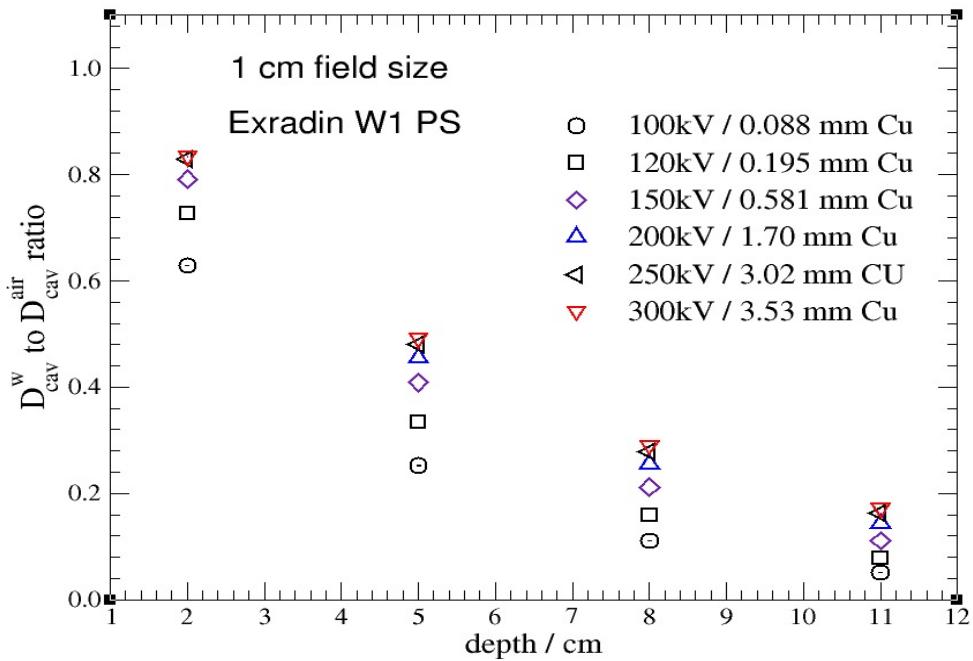


Figure 5.17: Same as fig 5.15 but for 1 cm field size beam.

The ratios of D_{cav}^w to D_{cav}^{air} decrease as the field size decreases from 10 cm to 1 cm for the Exradin W1 plastic scintillator (PS) as for the Ne2571 and Exradin A16 ion chambers which indicates the effect of scattered photons. The sensitive volume of the Exradin W1 plastic scintillator is made of polystyrene as opposed to the NE2571 and the Exradin A16 ion chambers where the sensitive volume is air. Polystyrene is well known for its water equivalent property for photon beams with energies between 0.3 MeV and 3 MeV²³. This property was investigated in this thesis and will be discussed in chapter 6 for the kilo-voltage x-ray beams between 100 kV and 300 kV.

5.6 $P_{Q,cham}$ calculation

As mentioned earlier in chapter 2, there are two ways to do the $P_{Q,cham}$ calculation; direct and indirect methods. For the direct calculation of $P_{Q,cham}$ the following equation is used,

$$P_{Q,cham} = \frac{\frac{K_{air}^w}{K_{air}^{free\ in-air}}}{\frac{D_{cav}^w}{D_{cav}^{air}}} . \quad (5.5)$$

The numerator and denominator of the eqn 5.5 was discussed in section 2.4 and the corresponding values were presented in sections 5.4 and 5.5. The direct calculation of the $P_{Q,cham}$ is now straight forward since it is just the ratio of the two ratios. This method was originally used by Ma and Nahum² to calculate the overall correction factor, incorporating all changes in chamber response between the calibration in-air and the in-water measurement i.e., their k_{ch} which is equivalent to the $P_{Q,cham}$ correction factor.

The second method of calculating a $P_{Q,cham}$ directly is similar to the previous method but instead of calculating detector dose, one can perform an experiment and obtain the detector signal for the in-air and in-water measurements and use them instead of the calculated ratio of detector dose in eqn 5.5. The air kerma for the free in-air and in-water measurements can be obtained using a reference dosimeter to be employed instead of calculated ratio of air kerma in eqn 5.5. Seuntjens et al¹¹ used this method to study the $P_{Q,cham}$ correction factor for several ion chambers where they considered an NE2571 ion chamber as a reference dosimeter to calculate the air kerma free in-air and in-water. Note that the $P_{Q,cham}$ values for the reference dosimeter (i.e., the NE2571 ion chamber) must be known in order to obtain the $P_{Q,cham}$ correction factor for other detectors.

Another way to calculate the overall correction factor ($P_{Q,cham}$) is to employ a combination of measurements and Monte Carlo calculations. The angular-energy dependency of a detector response as well as the stem effect can be found through experiment and Monte Carlo simulations can be used to calculate the photon fluence distribution and the displacement effect due to the cavity of the detector.³

The indirect method in this thesis is similar to the last method mentioned above but only Monte Carlo simulations are employed and more calculations are required to obtain $P_{E,\theta}$, P_{dis} , and $P_{stem,w}$. Once these components are determined, the $P_{Q,cham}$

correction factor can be achieved by multiplying the components using eqn 2.15 (page 10).

5.6.1 $P_{E,\theta}$ calculation

The first component of the $P_{Q,cham}$ correction factor is the $P_{E,\theta}$ correction which takes into account the difference in detector reading for the in-water measurement relative to the in-air calibration due to the change of the beam quality caused by the presence of water. The TG-61 protocol indicates⁵ that for the calculation of $P_{E,\theta}$ correction, the effect of stem should not be considered; hence the correction due to the presence of stem must be calculated separately i.e., $P_{stem,w}$. This means that the $P_{E,\theta}$ correction factor must be calculated using a stemless detector.

Considering a stemless detector, the effect of detector's wall and electrode is considered in the in-air calibration coefficient (N_K^{air}). This effect is the ratio of the air kerma free in-air to the cavity dose of the stemless detector ($K_{air}^{free\ in-air}/D_{cav}^{air,stemless}$). Fig 5.18 (a) and (b) show the geometries for the calculations of air kerma free in-air and the stemless detector's dose respectively. In order to use the same detector for the in-water measurement, one must consider the change of the detector's wall and electrode effects relative to the in-air calibration due to the presence of water. To do this, the ratio of air kerma in the water phantom to the stemless detector dose in the same phantom is calculated $\bar{K}_{air}^w/D_{cav}^{w,stemless}$. Fig 5.18 (c) and (d) show the geometry for the calculations of the air kerma in the water phantom and stemless detector dose in the same phantom respectively. The effects of the detector's wall and electrode for in-water measurement relative to the in-air calibration (i.e., $P_{E,\theta}$ correction factor) can be obtained using the following steps. By definition

$$\bar{K}_{air}^w = D_{cav}^{w,stemless} N_K^{air,stemless} P_{E,\theta} , \quad (5.6)$$

where \bar{K}_{air}^w is the air kerma at the small cylindrical air cavity shown in fig 5.18 (d). The size of the small air cavity is the same as the one for the calculation of the air kerma for in-water phantom and in-air calculation, see fig 5.5 (i.e., 0.1 cm thickness and 0.1 cm diameter). Note that the small air cavity is surrounded by the larger air cavity with the outer dimensions of the detector used in fig 5.18 (c).

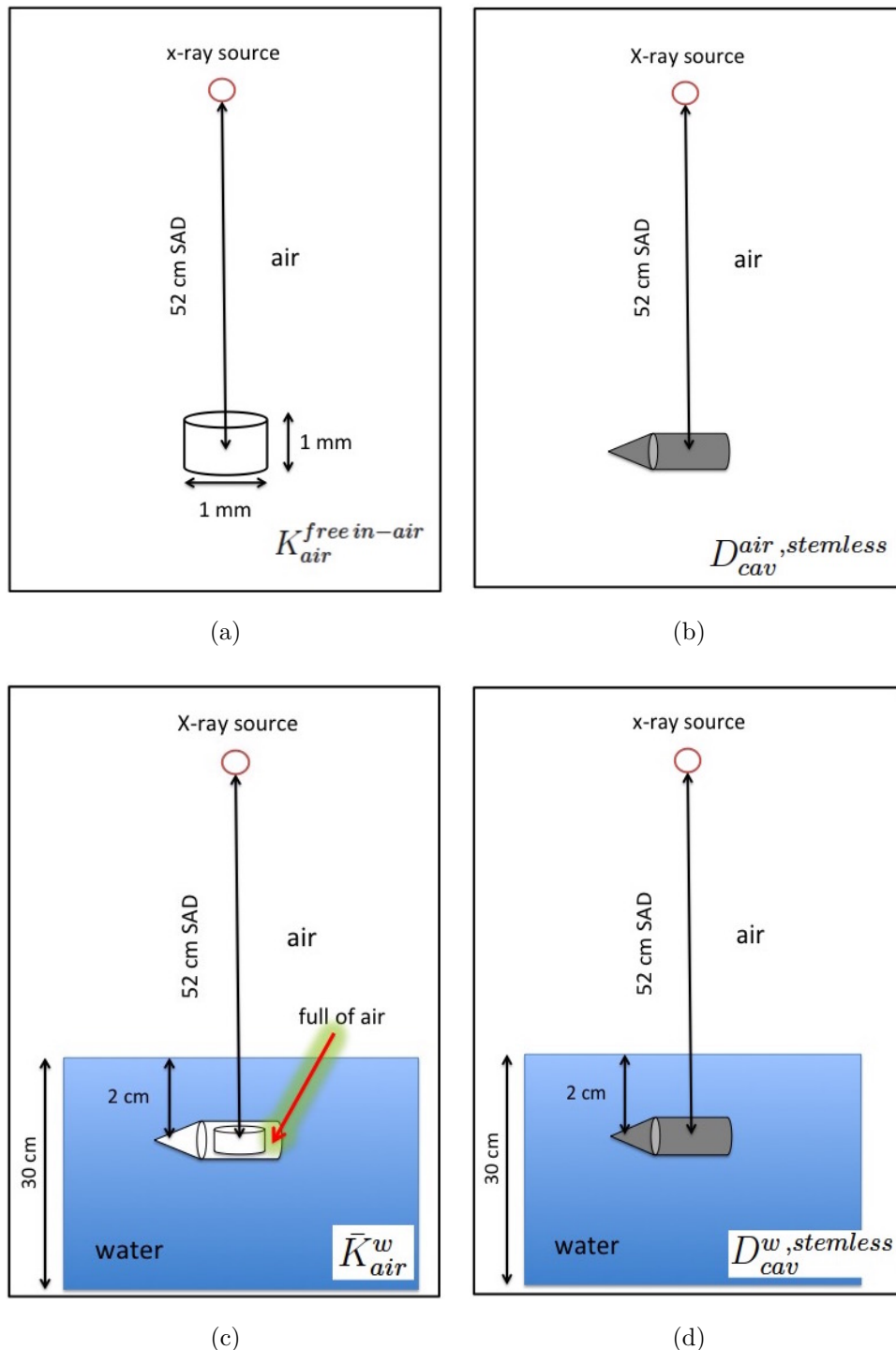


Figure 5.18: The geometries for the calculation of the $P_{E,\theta}$ correction factor. The right panels calculate the dose to the detector's cavity free in-air (b) and in-water (d), and the left panels calculate the air kerma free in-air (a) and the air kerma at the small cylindrical air cavity surrounded by a larger air cavity (c). Note that electron transport is off for the calculations in (a) and (c).

In eqn 5.6, $N_K^{air,stemless}$ is the air kerma calibration coefficient for a stemless detector for free-in-air,

$$N_K^{air,stemless} = \frac{K_{air}^{free\ in-air}}{D_{cav}^{air,stemless}} . \quad (5.7)$$

One can insert the $N_K^{air,stemless}$ calibration coefficient from eqn 5.7 into eqn 5.6 to calculate the $P_{E,\theta}$ correction factor as :

$$P_{E,\theta} = \frac{\frac{\bar{K}_{air}^w}{D_{cav}^{w,stemless}}}{\frac{K_{air}^{free\ in-air}}{D_{cav}^{air,stemless}}} = \frac{\frac{\bar{K}_{air}^w}{K_{air}^{free\ in-air}}}{\frac{D_{cav}^{w,stemless}}{D_{cav}^{air,stemless}}} . \quad (5.8)$$

The equivalent of the $P_{E,\theta}$ correction factor, called k_α , was determined by Seuntjens and Verhaegen³ at depths of 2 cm and 5 cm in a water phantom by performing an experiment where they first measured the combined angular-energy response for angles between -135 to 135 degree and fitted it with polynomials to obtain response function. This response function was used in a Monte Carlo simulation to calculate the k_α correction factor considering a parallel photon fluence spectrum while in this thesis, a collimated point source beam is considered.

5.6.2 $P_{stem,w}$ calculation

The $P_{stem,w}$ correction factor is the second component of the $P_{Q,cham}$ which takes into account the effect of the stem on the detector's response for the in-water measurement relative to the in-air calibration. The in-air calibration coefficient includes the stem effect for the in-air measurement i.e., $P_{stem,air}$. One can calibrate a detector with stem and without stem for free-in-air measurement using following eqns,

$$K_{air}^{free\ in-air} = N_K^{air} D_{cav}^{air} , \quad (5.9)$$

and

$$K_{air}^{free\ in-air} = N_K^{air,stemless} D_{cav}^{air,stemless} , \quad (5.10)$$

where eqns 5.9 and 5.10 represent the air kerma calibration for a detector with stem and without stem respectively. Dividing eqns 5.9 and 5.10 gives:

$$\frac{N_K^{air}}{N_K^{air,stemless}} = \frac{D_{cav}^{air,stemless}}{D_{cav}^{air}} . \quad (5.11)$$

As mentioned above, the N_K^{air} calibration coefficient includes the stem correction factor for free-in-air measurement while $N_K^{air,stemless}$ does not; hence

$$N_K^{air} = N_K^{air,stemless} P_{stem,air} . \quad (5.12)$$

Using eqns 5.11 and 5.12, the $P_{stem,air}$ correction factor can be calculated as

$$P_{stem,air} = \frac{D_{cav}^{air,stemless}}{D_{cav}^{air}} . \quad (5.13)$$

where $D_{cav}^{air,stemless}$ and D_{cav}^{air} are the dose to the detector's cavity for free-in-air calculation without stem and with stem respectively (see fig 5.19 (d) and (c)).

The stem correction factor for the in-water measurement ($\bar{P}_{stem,w}$) can be approached using the same methodology discussed above but for the in-water calibration instead of the free-in-air. One can show

$$\bar{P}_{stem,w} = \frac{D_{cav}^{w,stemless}}{D_{cav}^w} , \quad (5.14)$$

where $D_{cav}^{w,stemless}$ and D_{cav}^w are dose to the detector's cavity for in-water calculation without stem and with stem respectively (see fig 5.19 (b) and (a)).

In order to use a free-in-air calibrated detector for in-water measurement, one must consider the stem effect for the in-water measurement ($\bar{P}_{stem,w}$) relative to the in-air calibration which is the $P_{stem,w}$ correction factor and can be calculated as,

$$P_{stem,w} = \frac{\bar{P}_{stem,w}}{P_{stem,air}} . \quad (5.15)$$

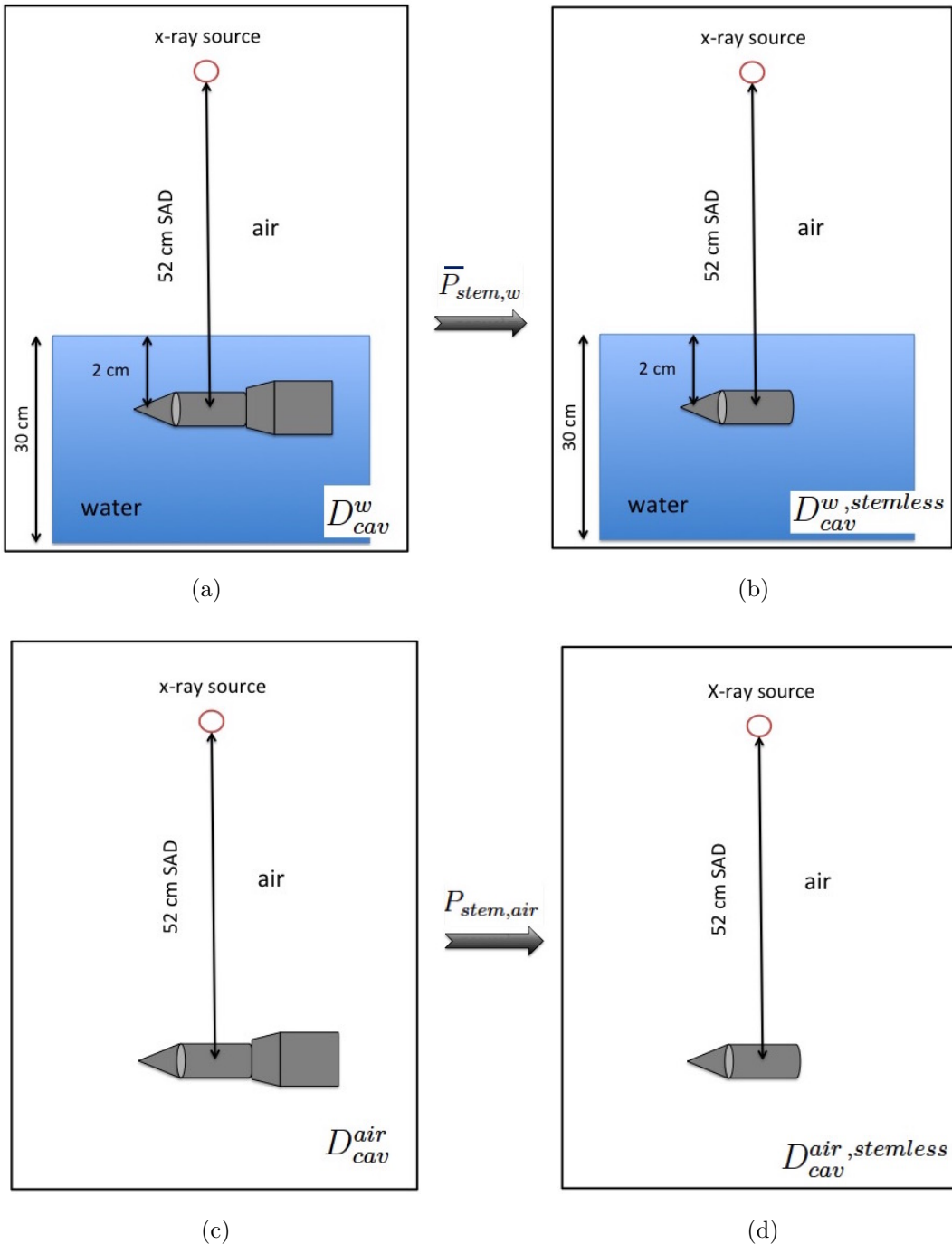


Figure 5.19: The geometries for the calculation of the $\bar{P}_{stem,w}$ and $P_{stem,air}$ corrections. (a) shows the detector with stem in the water phantom for D_{cav}^w calculation and (b) is the same detector but without the stem for $D_{cav}^{w,stemless}$ calculation. (c) and (d) represent the detector free in-air with and without the stem for calculation of D_{cav}^{air} and $D_{cav}^{air,stemless}$ respectively. Dose to the detector's cavity is calculated for all geometries. Note that the air between the x-ray source and the water phantom has been considered for the simulation of the x-ray spectrum using SpekCalc software.

Eqn 5.15 indicates that $P_{stem,w}$ correction factor is the ratio of stem effect on the detector responds for in-water measurement respect to the in-air calibration and can be written as,

$$P_{stem,w} = \frac{\frac{D_{cav}^{w,stemless}}{D_{cav}^w}}{\frac{D_{cav}^{air,stemless}}{D_{cav}^{air}}} \quad (5.16)$$

Seuntjens and Verhaegen³ used a combination of experiment and Monte Carlo simulation to determine the $P_{stem,w}$ for an NE2571 ion chamber. They defined the following equation for the stem correction factor ($P_{stem,w}$),

$$P_{stem,w} = \frac{p_{st}(z, d)}{k_{st}} \quad , \quad (5.17)$$

where k_{st} is defined below and $p_{st}(z,d)$ is the ratio of water kerma in a cylindrical water cavity without stem to water kerma in the same water cavity with stem at depth z and field size d,

$$p_{st}(z, d) = \frac{K_w^{stemless}}{K_w^{stem}} \quad . \quad (5.18)$$

The values of k_{st} in eqn 5.16 was measured using a dummy stem in a free in-air measurement as follows,

$$k_{st} = \frac{M_{s,a}}{M_{2s,a}} \quad , \quad (5.19)$$

where $M_{s,a}$ and $M_{2s,a}$ are the detector signals for the free in-air measurements with stem and with an extra dummy stem respectively.

The method is clearly different with the approach of this thesis. Seuntjens and Verhaegen³ used the ratio of water kerma in a cylindrical water cavity without the stem to water kerma in the same water cavity with the stem instead of using the ratio of detector signal without stem to the detector signal with stem. As they discussed, the main reason for this choice was due to the specific difficulties for stem positioning and the presence of the waterproof sleeve in the water phantom which limited the accuracy of the overall stem correction factor. In addition, they used a full aluminium bar to simulate the stem for the calculation of the $p_{st}(z, d)$ in eqn 5.18 while in this thesis a full geometry of the stem is considered.

Ma and Nahum²⁷ introduced the global stem effect correction factor ($k_{stem,global}$)

which is equivalent to the $P_{stem,w}$ in this thesis. They calculated the $k_{stem,global}$ for an NE2571 ion chamber by Monte Carlo simulations in a manner equivalent to eqn 5.16.

Ma and Nahum²⁷ employed the EGS4 user code DOSIMETER²⁸ which was limited to planar-cylindrical geometries; as a result, for the NE2571 ion chamber, simplified stem geometries were simulated while in this thesis the exact stem geometries are considered. In addition to the simplified stem geometries, they used aluminium and PMMA as the stem materials for their simulations but the realistic stem is made of aluminum, PTFCE, graphite, and Dural (see fig 4.1 page 16).

5.6.3 P_{dis} calculation

The last component of the $P_{Q,cham}$ is the P_{dis} correction factor which is a correction factor for the change in the air kerma due to displacement of water by the detector body.

As fig 5.20 shows, the P_{dis} correction factor replaces the air cavity with the detector's outer dimensions surrounding the small cylindrical air cavity (a) with water (b) and can be calculated using

$$P_{dis} = \frac{K_{air}^w}{\bar{K}_{air}^w}, \quad (5.20)$$

where K_{air}^w and \bar{K}_{air}^w are the air kerma in the water phantom scored in the small cylindrical air cavity (i.e., 0.1 cm length and 0.1 cm diameter) in fig 5.20 (a) and (b) respectively without electron transport. Note that the P_{dis} correction factor does not depend on the materials of a detector but only the size of the detector's body.

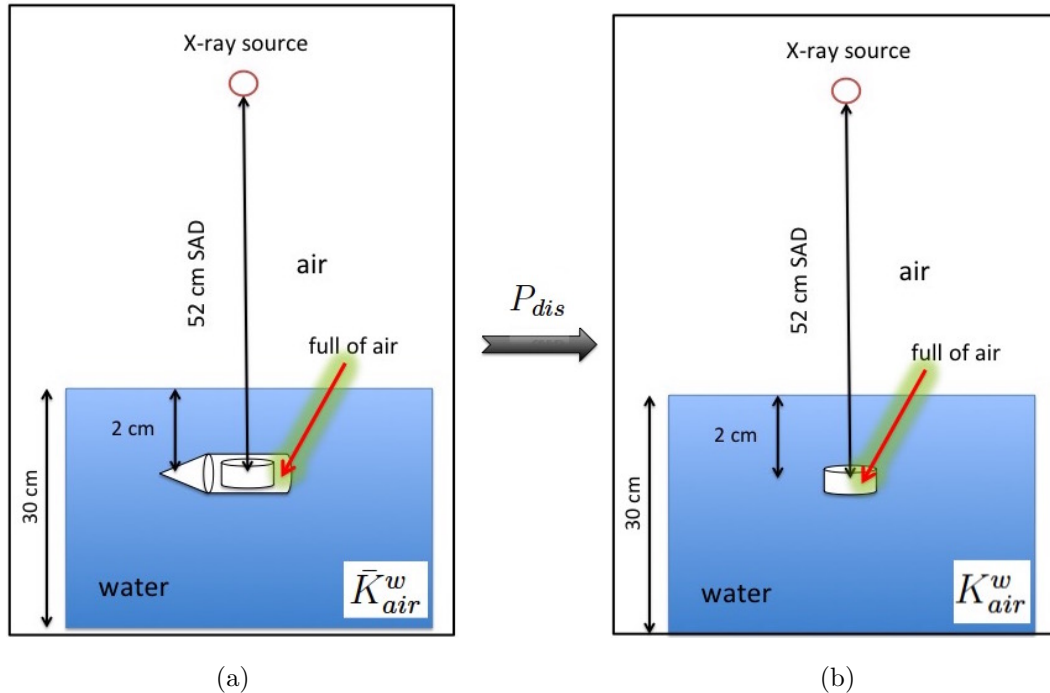


Figure 5.20: The geometries for the calculation of the P_{dis} . (a) the geometry for \bar{K}_{air}^w calculation consist of a small cylindrical air cavity with 0.1 cm length and 0.1 cm diameter surrounded by another air cavity with the outer dimensions of the detector body in the water phantom and is the same as fig 5.18 (c). (b) the geometry for calculation of K_{air}^w and is the same small cylindrical air cavity in the water phantom which is the same as fig 5.5 (b) for 2 cm depth. Air kerma is scored in the small cylinder for both geometries without electron transport.

Nahum and Knight¹ introduced the P_{dis} correction factor as a ratio of air kermas

$$P_{dis}^{NK} = \frac{K'_a}{K_a}, \quad (5.21)$$

where K'_a is the air kerma in a cylinder with the outer dimensions of the detector body filled with air having water density centred at the reference point, and K_a is the air kerma in the same air cavity with air density. Ma and Nahum²⁹ showed that instead of the ratio of air kermas, the ratio of water kermas can be used to define P_{dis}^{MN} as,

$$P_{dis}^{MN} = \frac{K_{w,u}}{K'_{w,u}}, \quad (5.22)$$

where $K_{w,u}$ and $K'_{w,u}$ are the water kerma at the centre of the cylinder with the detector's outer dimensions full of water with water and air densities respectively. The values of P_{dis}^{NK} and P_{dis}^{MN} are consistent within the 0.1 % as reported by Seuntjens and Verhaegen³ who employed the ratio of water kerma (see fig 6.12, page 66) to calculate the P_{dis} correction factor for an NE2571 ion chamber and their values only agreed at the 1% level (see fig below).

The main differences between the method of this thesis, and those of Seuntjens and Verhaegen and Nahum and Knight for calculating the P_{dis} correction factor are substantial. In this thesis, air kerma is scored in a small cylindrical air cavity with 0.1 cm thickness and 0.1 cm diameter surrounded by another air cavity with the outer dimensions of the detector (see fig 5.20, page 47), while Seuntjens and Verhaegen calculated water kerma at the centre of a water cylinder with outer dimensions of the detector and Nahum and Knight used an air cylinder with the outer dimensions of the detector to calculate air kerma; hence both groups considered absorbed energy averaged over the whole volume with the outer dimensions of the detector.

Considering the displacement effect due to the presence of the detector's body for the in-water measurement, three individual effects contribute to the displacement correction factor :

- the decreased attenuation of the primary photons
- the decreased attenuation of the scattered photons
- the decreased creation of scattered photons from the displaced water

The first two effects increase the air kerma at the centre of the air cavity with the detector's outer dimensions (see fig 5.20 (a)) while the third effect decreases it. The contribution of these effects depends on quality of the radiation, size of the detector (i.e., displaced water volume), and the depth of the reference point of measurement in the water phantom. As stated by Nahum³⁰, Linden employed a theoretical expression for the fractional increase in primary photon fluence due to the displaced water which is,

$$\alpha = e^{\mu r} \left[1 - \mu r \left(1 - \frac{8}{3}\pi \right) \right] - 1 , \quad (5.23)$$

where μ is the total linear attenuation coefficient for the primary radiation and r is the radius of the detector. He estimated a similar expression for the other two effects

using equation 5.23 for different depths in water and x-ray beams with 0.35 mm Cu or 0.2 mm Cu HVLs. He considered a 100 cm² field size beam with 60 cm SAD as well as a chamber with 2.5 cm length and 1.35 cm diameter. He predicted an increase of the chamber reading by 3.8%, 4.7%, and 5.5% for an x-ray beam with 2.0 mm Cu HVL at 1.3, 5 and 8 cm in the water phantom respectively. The corresponding values for the x-ray beam with a HVL of 0.35 mm Cu are 8.3% and 11.6% at 1.3 cm and 8 cm depth in a water phantom. Hence, for the cases considered, Linden³¹ showed that the decreased attenuation of the primary and scattered photons dominated the decreased creation of scattered photons from the displaced water.

This thesis uses a different approach to study the three individual effects which contribute to the P_{dis} correction factor. Generally speaking, one can find the difference between the air kermas (K_{air}^w and \bar{K}_{air}^w) in the small cylindrical air cavities in fig 5.20 (b) and (a) by calculating a combination of the three individual effects mentioned above. The values of K_{air}^w can be found using the calculated \bar{K}_{air}^w values as follows,

$$K_{air}^w = \bar{K}_{air}^w + \Delta K_{air}^w, \quad (5.24)$$

where ΔK_{air}^w is the increase in K_{air}^w due to displaced water i.e., adding the contributions of three individual effects together. Instead of considering these three effect separately, consider the effect of decreased attenuation of the primary from the displaced water, namely $\Delta_p K_{air}^w$, and the combination of the decreased attenuation and creation of the scattered photons from the displaced water, namely $\Delta_s K_{air}^w$, from the displaced water. Eqn 5.24 can be rewritten as

$$K_{air}^w = \bar{K}_{air}^w + \Delta_p K_{air}^w + \Delta_s K_{air}^w. \quad (5.25)$$

K_{air}^w and \bar{K}_{air}^w can be written as

$$K_{air}^w = (K_{air}^w)_p + (K_{air}^w)_s \quad (5.26)$$

and

$$\bar{K}_{air}^w = (\bar{K}_{air}^w)_p + (\bar{K}_{air}^w)_s \quad (5.27)$$

where p and s indicate the respective contributions of primary and scattered photons

to the air kerma.

Using eqns 5.25, 5.26 and 5.27, the contribution of the primary photons and scattered photons can be written separately as,

$$(K_{air}^w)_p = (\bar{K}_{air}^w)_p + \Delta_p K_{air}^w, \quad (5.28)$$

and

$$(K_{air}^w)_s = (\bar{K}_{air}^w)_s + \Delta_s K_{air}^w. \quad (5.29)$$

To implement this method, the FLURZnrc user code was employed to score the primary photon fluence at the small cylindrical air cavity with length of 0.1 cm and 0.1 cm diameter. This user code is limited to planar cylindrical geometries, hence the geometry of fig 5.20 is not possible using FLURZnrc. To overcome this problem, a different geometry was implemented which is shown in fig 5.21 (b).

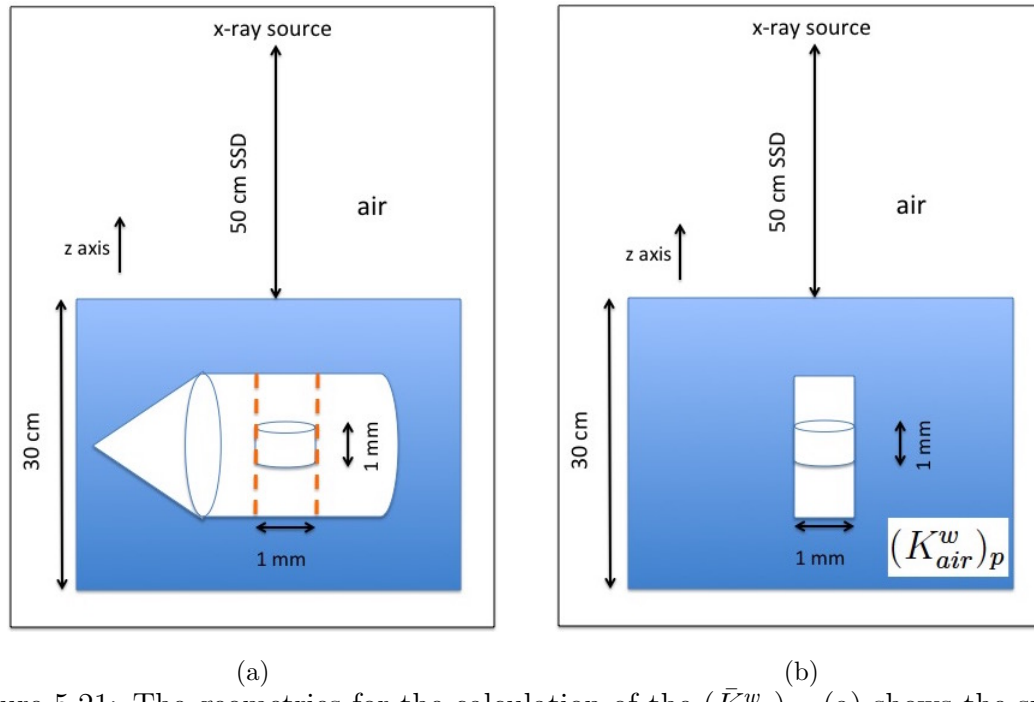


Figure 5.21: The geometries for the calculation of the $(\bar{K}_{air}^w)_p$. (a) shows the small cylindrical air cavity with 0.1 cm length and 0.1 cm diameter surrounded by another air cavity with the outer dimensions of the detector body in the water phantom. This geometry can not be modeled using FLURZnrc. (b) is the geometry for air kerma calculation using primary photons in the same small cylindrical air cavity in the water phantom surrounded by a cylinder filled with air with the length to be equal to the diameter of the detector and 0.1 cm diameter.

Fig 5.21 (a) shows that the effect of decreased attenuation of the primary photons depends on the displaced water within the dashed lines, hence the other parts of displaced water do not contribute to the change in the primary photon fluence in the small cylindrical air cavity and can be ignored as shown in fig 5.21 (b) where the small cylindrical air cavity is surrounded by another cylinder filled with air in the water phantom. Fig 5.21 (a) also implies that the change in the primary photon fluence in the small cylindrical air cavity is field size independent as long as the field size covers the cavity, and the change only depends on the radius of the detector. This geometry (fig 5.21 (b)) was simulated using the FLURZnrc user code to score the primary photon fluence for different depths in the water phantom and the six x-ray beams. The water phantom is considered as a cylinder with radius of 17 cm and length of 30 cm. A collimated point source was employed with a 1 cm diameter circular field size and 50 cm SSD. To determine the air kerma, the kermadp user code was employed which uses the photon fluence spectrum to calculate the air kerma. The values of $(K_{air}^w)_p$ was calculated similar to the calculation of $(\bar{K}_{air}^w)_p$ using the geometry of fig 5.20 (b) (page 47) except that a cylindrical water phantom was considered and only air kerma due to the primary photons were scored.

Using eqn 5.28, $\Delta_p K_{air}^w$ is,

$$\Delta_p K_{air}^w = (K_{air}^w)_p - (\bar{K}_{air}^w)_p \quad (5.30)$$

which is < 0 and represents the decreased attenuation of the primary photons caused by displaced water.

To calculate the portion of air kerma from scattered photons, eqns 5.26 and 5.27 should be rewritten as,

$$(K_{air}^w)_s = K_{air}^w - (K_{air}^w)_p , \quad (5.31)$$

and

$$(\bar{K}_{air}^w)_s = \bar{K}_{air}^w - (\bar{K}_{air}^w)_p , \quad (5.32)$$

where the right hand sides of these two equations are known as above. Finally, eqn 5.29 is needed to find the combination of decreased attenuation and creation of scattered

photons due to the displaced water, $\Delta_s K_{air}^w$,

$$\Delta_s K_{air}^w = (K_{air}^w)_s - (\bar{K}_{air}^w)_s = K_{air}^w - \bar{K}_{air}^w - [(K_{air}^w)_p - (\bar{K}_{air}^w)_p] \quad (5.33)$$

Note that the effect of scattered photon fluence depends on the total geometry of the detector's body, not only the radius, as well as the field size of the radiation unlike the effects due to the primary photons fluence. To understand the variation of the P_{dis} correction factor, it is important to derive a direct relation between P_{dis} , $\Delta_p K_{air}^w$, and $\Delta_s K_{air}^w$. This can be done using eqns 5.20 and 5.25 as follows

$$P_{dis} = \frac{K_{air}^w}{\bar{K}_{air}^w} \implies P_{dis} = \frac{\bar{K}_{air}^w + \Delta_p K_{air}^w + \Delta_s K_{air}^w}{\bar{K}_{air}^w} , \quad (5.34)$$

i.e.,

$$P_{dis} = 1 + \frac{\Delta_p K_{air}^w + \Delta_s K_{air}^w}{\bar{K}_{air}^w} , \quad (5.35)$$

which connects P_{dis} to $\Delta_p K_{air}^w$ (eqn 5.30), and $\Delta_s K_{air}^w$ (eqn 5.33) directly which is used for the analysis of the displacement correction factor in the next chapter.

Once the three components of the $P_{Q,cham}$ are calculated, the result of their product should be equal to the $P_{Q,cham}$ correction factor i.e.,:

$$P_{E,\theta} \times P_{stem,w} \times P_{dis} = \frac{\frac{\bar{K}_{air}^w}{K_{air}^{free in-air}}}{\frac{D_{cav}^{w,stemless}}{D_{cav}^{air,stemless}}} \times \frac{\frac{D_{cav}^{w,stemless}}{D_{cav}^{air,stemless}}}{\frac{D_{cav}^{air}}{D_{cav}^{air}}} \times \frac{\frac{K_{air}^w}{\bar{K}_{air}^w}}{\frac{K_{air}^{free in-air}}{D_{cav}^{air}}} = \frac{K_{air}^w}{\frac{D_{cav}^w}{D_{cav}^{air}}} = P_{Q,cham}. \quad (5.36)$$

Numerical values and analysis of the correction factors discussed here are presented in the next chapter.

Chapter 6

$P_{Q,cham}$ correction factor

In chapter 5, the methods of $P_{Q,cham}$ correction factor calculation were explained including the direct and indirect methods. In this chapter, the numerical values of the $P_{Q,cham}$ correction factor are presented including the $P_{E,\theta}$, P_{dis} , and $P_{stem,w}$ correction factors for the NE2571 ion chamber, Exradin A16 ion chamber, and Exradin W1 plastic scintillator. A discussion of the $P_{Q,cham}$ variation considering its components is also provided in this chapter.

6.1 The NE2571 ion chamber

The measurement of absorbed dose in a water phantom requires a proper employment of equation 2.2, i.e.,

$$D_{w,z=2cm} = M_w N_K^{air} P_{Q,cham} P_{sheath} \left[\left(\frac{\bar{\mu}_{en}}{\rho} \right)_{air}^w \right]_{water}, \quad (6.1)$$

which means the evaluation of $P_{Q,cham}$, P_{sheath} , and $\left[\left(\frac{\bar{\mu}_{en}}{\rho} \right)_{air}^w \right]_{water}$ must be done using the same incident spectrum which has been used to calculate the free in-air calibration coefficient (N_K^{air}). The quality of a spectrum, as mentioned in chapter 2, should be specified using the x-ray tube potential and the HVL of the beam. Considering this fact, the six different beams used in this study (see table 3.2,p 14) have been chosen to be consistent with the beams used for the calculation of the $\left[\left(\frac{\bar{\mu}_{en}}{\rho} \right)_{air}^w \right]_{water}$ values¹⁹ in the TG-61 protocol. This consistency does not exist between the qualities of the spectra used to obtain the $\left[\left(\frac{\bar{\mu}_{en}}{\rho} \right)_{air}^w \right]_{water}$ and $P_{Q,cham}$ values¹¹ in the TG-61 protocol and thus the $P_{Q,cham}$ values calculated here are not for the same beam qualities as presented in TG-61.

The TG-61 protocol includes the $P_{Q,\text{cham}}$ values obtained by Seuntjens et al¹¹ at 2 cm depth in water for beams with HVLs between 0.1 - 4.0 mm Cu for several ion chambers. They used the NE2571 ion chamber as a reference dosimeter to find relative $P_{Q,\text{cham}}$ correction factors for other ion chambers (i.e., NE2561, NE2611, NE2581, PTW N3001, Exradin A12, and Capintec PR-06C) in which the values of the $P_{Q,\text{cham}}$ correction factor for the NE2571 ion chamber used by TG-61 were deduced from Seuntjens and Verhaegen's paper³ discussed in section 5.6 (page 39). A comparison is shown in fig 6.1 between the $P_{Q,\text{cham}}$ correction factors from the present calculations and the TG-61 protocol for the NE2571 ion chamber.

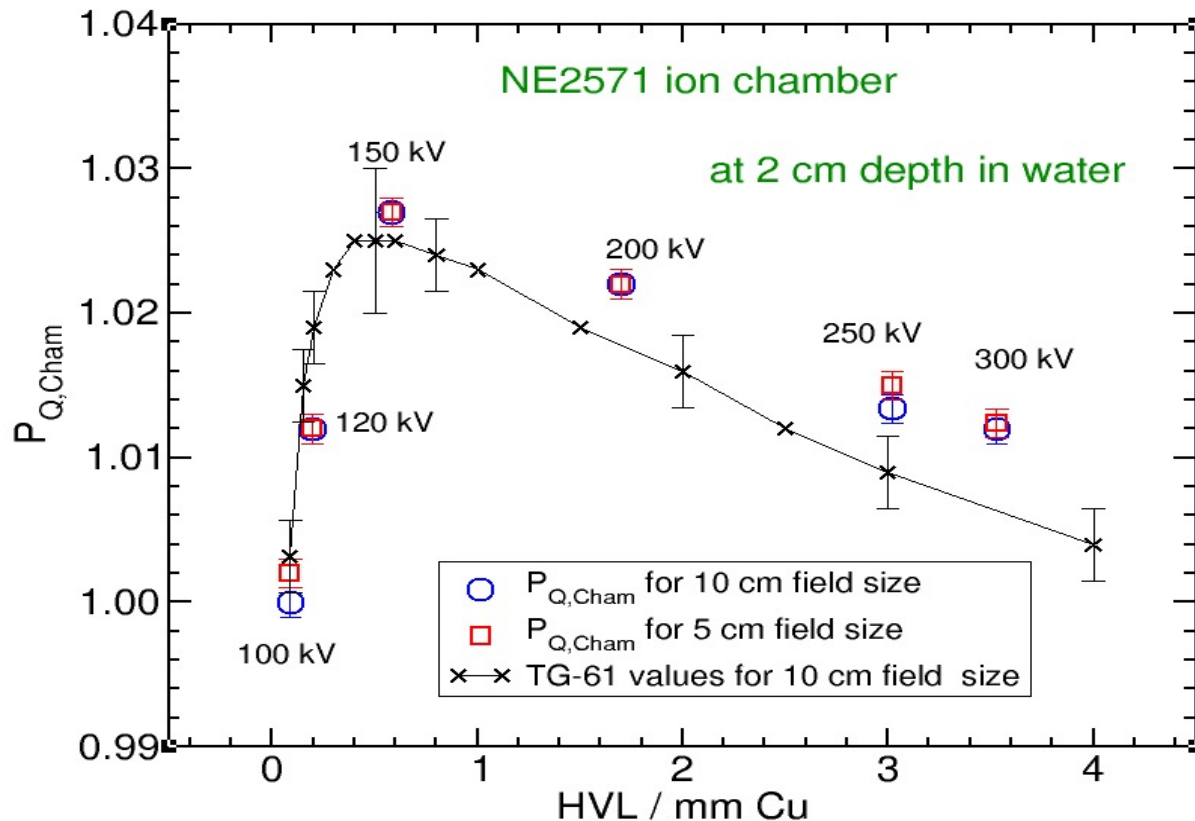


Figure 6.1: The $P_{Q,\text{cham}}$ values for a NE2571 ion chamber at 2 cm depth for 5 cm and 10 cm field sizes and x-ray tube potentials between 100 kV - 300 kV in this study. The $P_{Q,\text{cham}}$ values in the TG-61 for 10 cm field size are also provided. The statistical uncertainties on the values of this thesis are less than 0.1%. The uncertainties for the values of Seuntjens et al¹¹ are shown.

The values of the $P_{Q,\text{cham}}$ correction factors for 5 cm and 10 cm field sizes in this

thesis have a maximum deviation from each other of 0.25% for the 100 kV x-ray beam (HVL: 0.088 mm Cu) close to the 0.1% statistical uncertainty. This deviation decreases to 0.15% for the 250 kV x-ray beam (HVL: 3.02 mm Cu) which is within the 0.1% statistical uncertainty and is negligible for other x-ray beams. Fig 6.1 shows that our $P_{Q,cham}$ correction factor values are not in agreement with the TG-61 values within the statistical uncertainties except for the 150 kV x-ray beam (HVL: 0.581 mm Cu). The overall uncertainty on the $P_{Q,cham}$ correction factor was reported to be 1.5% in the TG-61 protocol. This thesis employed the EGSnrc code system which has a systematic uncertainty of 0.1% relative to its own cross-sections²⁴. There are inconsistencies between the specification of the beam qualities in this thesis and Seuntjens and Verhaegen's work³ where neither the x-ray tube potentials nor added filtration are the same as those chosen in this thesis. This could be one of the reasons for the disagreements between our results and those of the TG-61 protocol. The $P_{Q,cham}$ correction factor was calculated for a 70 kV x-ray beam obtained using the SpekCalc software¹⁵ considering a 3.42 mm aluminum filter and with the same HVL as the 100 kV x-ray beam (HVL: 0.088 mm Cu). This was used to study the effect of x-ray tube potential on the $P_{Q,cham}$ correction factor for two x-ray beams with the same HVL. The results show that the $P_{Q,cham}$ value at 2 cm depth in water for the 70 kV x-ray beam is 0.3% higher than that for the 100 kV x-ray beam with the same HVL (0.088 mm Cu) with a 0.1% statistical uncertainty. The $P_{Q,cham}$ value for the 70 kV x-ray beam (HVL: 0.088 mm Cu) is in agreement with the one from the TG-61 protocol which was calculated using an 80 kV x-ray beam.

The variation of the $P_{Q,cham}$ values with the beam quality (HVL) in water can be explained by the variation of its components namely $P_{E,\theta}$, $P_{stem,w}$, and P_{dis} with beam quality and depth in water.

The values of $P_{Q,cham}$, $P_{E,\theta}$, $P_{stem,w}$, P_{dis} for 5 cm and 10 cm field sizes at 2 cm depth in water are shown in fig 6.2 (page 56) where E_{mean} values are also presented (i.e. the average energy of the photon fluence at the small cylindrical air cavity, fig 5.20 (b), at 2 cm depth in water where the absorbed dose is scored).

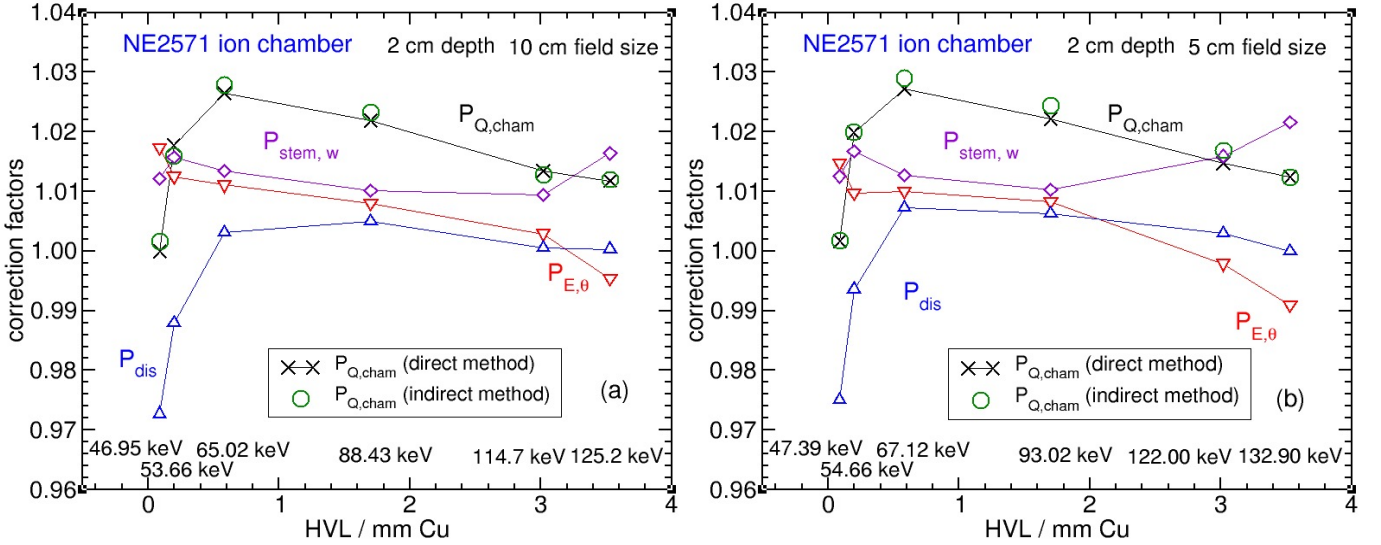


Figure 6.2: The variation of the $P_{Q,\text{cham}}$ correction factor and its components for the NE2571 ion chamber with beam quality at 2 cm depth in water for 10 cm (a) and 5 cm (b) field sizes. The average energies (E_{mean}) of the x-ray beams at 2 cm depth in the water phantom are provided. The statistical uncertainties are 0.1% for all values.

The maximum variation of the $P_{Q,\text{cham}}$ correction factor with HVL is 2.6% for 10 cm and 5 cm field sizes. At lower energy (i.e. lower HVLs), the P_{dis} correction factor dominates the other two components for 10 cm and 5 cm field sizes. As the energy of the beam increases the effect of P_{dis} correction factor decreases and the $P_{E,\theta}$ and $P_{\text{stem},w}$ factors become more important. Note that the E_{average} for each beam increases as the field size decreases, indicating that the contribution of the scattered photons in the spectrum at the central axis of the beam is larger for 10 cm field size in comparison with the 5 cm field size beam.

The variation of the $P_{Q,\text{cham}}$ correction factor and its components at 5 cm, 8 cm, and 11 cm depth are shown in figs 6.3, 6.4, and 6.5 respectively.

The maximum variation of the $P_{Q,\text{cham}}$ correction factor with HVL at 5 cm depth is 1.6% which is 1% lower than at 2 cm depth (i.e., 2.6%) for both 10 cm and 5 cm field sizes. At low energies, the P_{dis} correction factor has a larger contribution to the $P_{Q,\text{cham}}$ correction factor while at higher energies $P_{\text{stem},w}$ dominates the other two components.

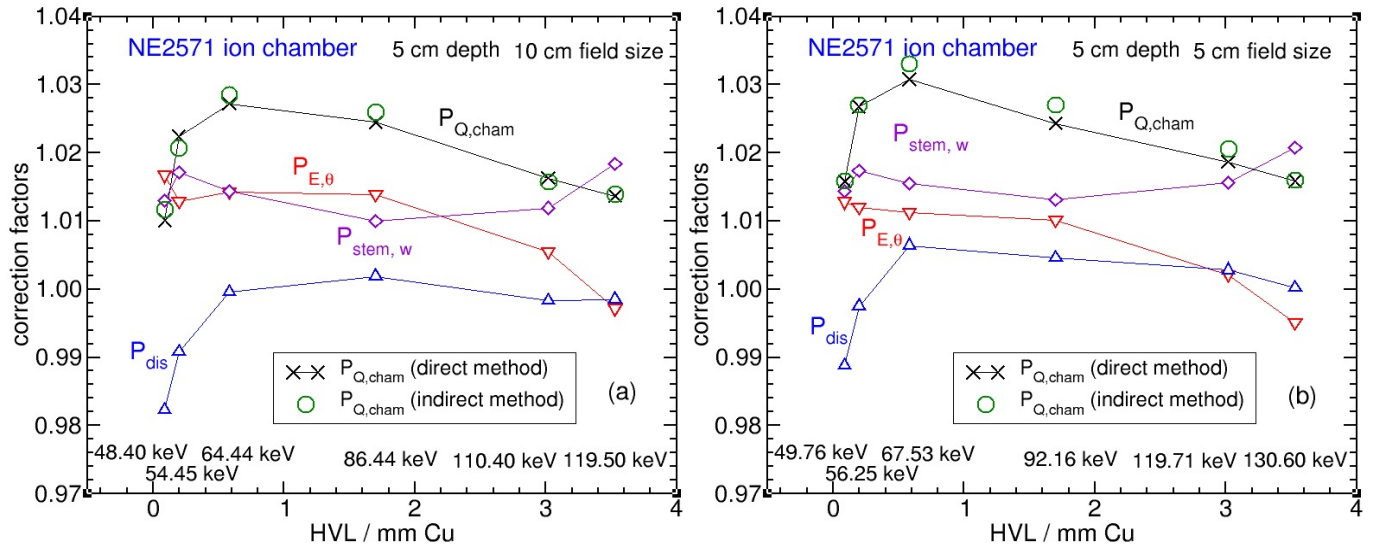


Figure 6.3: Same as fig 6.2 but at 5 cm depth. The statistical uncertainties are 0.1% for all values

The value of E_{mean} increases for 100 kV (HVL: 0.088 mm Cu) and 120 kV(HVL: 0.195 mm Cu) x-ray beams at 5 cm depth in water for 10 cm field size in comparison to the 2 cm depth (fig 6.2 (a)) due to the absorption of lower energy photons (i.e., beam hardening effect), but decreases for higher energy x-ray beams due to the domination of the increased scattered photons over the beam hardening effect. The same comparison but for 5 cm field size shows that the scattered photons domination over the beam hardening effect starts with the 150 kV (0.581 mm Cu) x-ray beam and continue for higher energies. Figs 6.4 and 6.5 show that the increasing or decreasing of the E_{mean} at 8 cm and 11 cm depth are in the same fashion as at 5 cm depth in the water phantom.

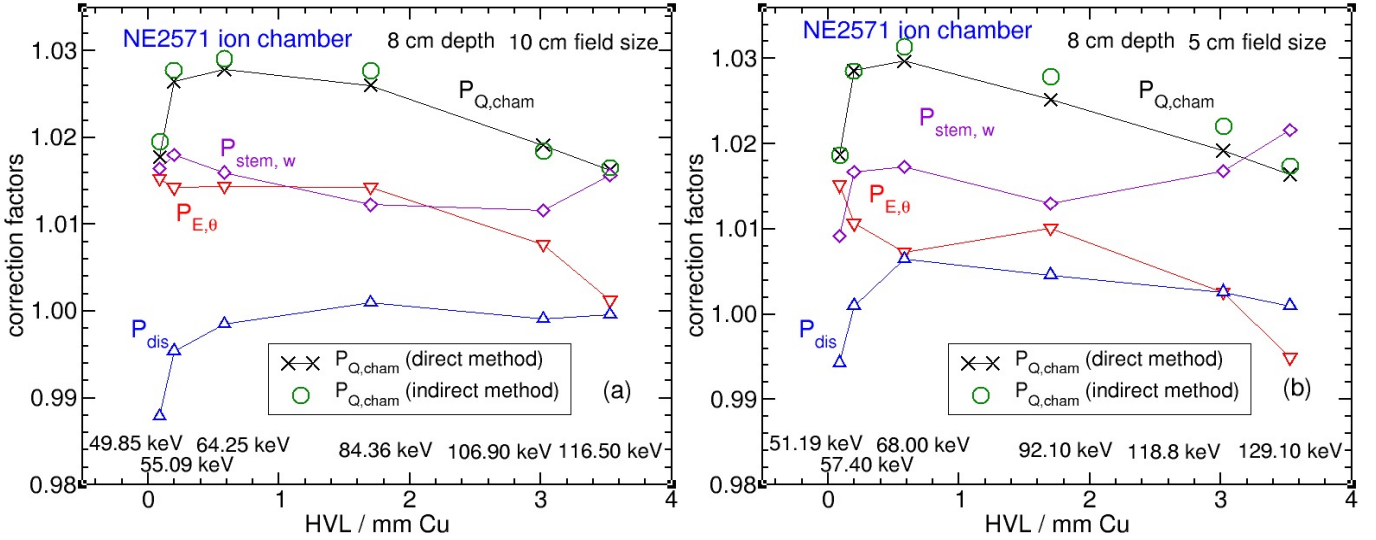


Figure 6.4: Same as fig 6.3 but at 8 cm depth in water. The statistical uncertainties are 0.1% for all values.

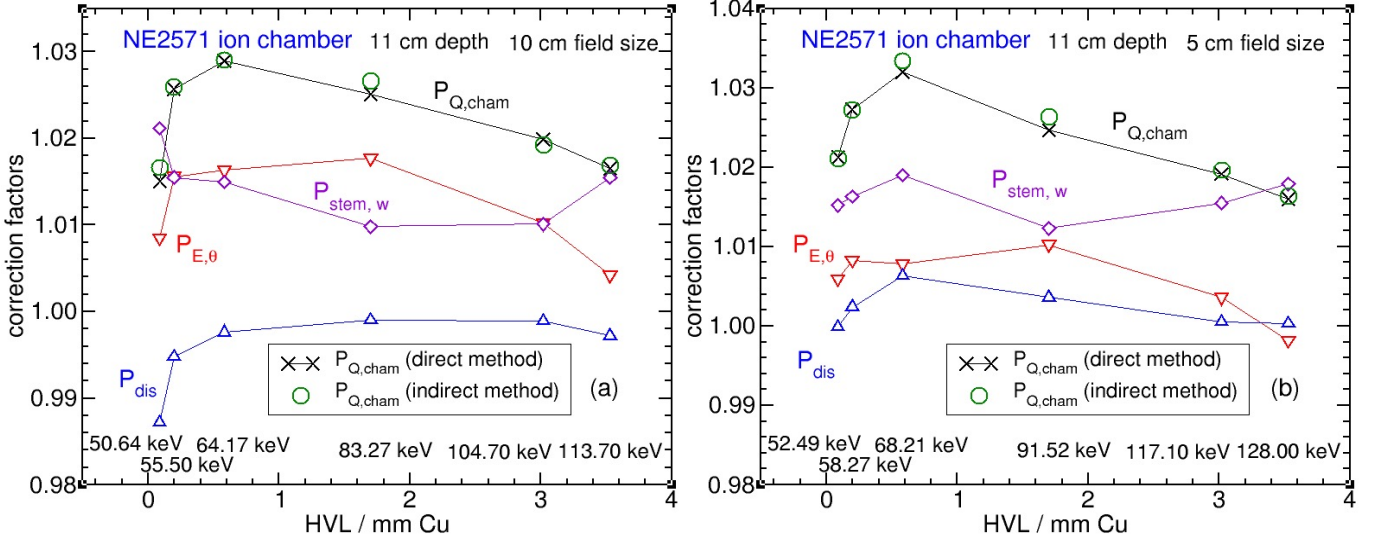


Figure 6.5: Same as fig 6.4 but at 11 cm depth in water. The statistical uncertainties are 0.1% for all values.

A comparison of $P_{Q,\text{cham}}$ values at depths of 5 cm, 8 cm, and 11 cm between 5 cm and 10 cm field size beams shows a variation of up to 0.6 % in the $P_{Q,\text{cham}}$ values which is 0.4 % more than the same comparison at the 2 cm depth in water which indicates that the field size dependency of the $P_{Q,\text{cham}}$ correction factor plays a more important role at greater depths in the water phantom for a NE2571 ionization chamber. The maximum variation of the $P_{Q,\text{cham}}$ correction factor with depth for a NE2571 ion chamber is 1.8%

from 2 cm to 11 cm depth in water and belongs to the 100 kV (HVL: 0.088 mm Cu) x-ray beam.

The variation of the $P_{Q,cham}$ correction factor with depth in water and field sizes for six different beam qualities have been discussed so far for a NE2571 ionization chamber. Now, the variation of the $P_{Q,cham}$ components i.e., $P_{E,\theta}$, P_{dis} , $P_{stem,w}$ for a NE2571 ionization chamber will be discussed individually.

6.1.1 The $P_{E,\theta}$ correction factor

The first component of the $P_{Q,cham}$ correction factor is $P_{E,\theta}$ which is the correction due to the change in the beam quality caused by water in comparison to the free in-air calibration coefficient beam quality. The $P_{E,\theta}$ calculation as discussed in section 5.6 is:

$$P_{E,\theta} = \frac{\frac{\bar{K}_{air}^w}{K_{air}^{free\ in-air}}}{\frac{D_{cav}^{w,stemless}}{D_{cav}^{air,stemless}}} , \quad (6.2)$$

where \bar{K}_{air}^w and $K_{air}^{free\ in-air}$ are the air kerma at the small cylindrical air cavity for in-water and the air kerma in-air respectively (see figs 5.18 (b) and 5.5 (a), pages 39 and 26); $D_{cav}^{w,stemless}$ and $D_{cav}^{air,stemless}$ are the stemless detector dose for the in-water and in-air calculations.

Generally speaking, the variation of the $P_{E,\theta}$ correction factor depends on the variation of the stemless detector dose in the water phantom ($D_{cav}^{w,stemless}$) in respect to the change of the beam quality caused by the water. Figs 6.2 - 6.5, show that the E_{mean} value of the x-ray beam changes with depth in water due to the beam hardening effect and scattered photons where the first one increases the E_{mean} value and the second one decreases it. The change of the E_{mean} value (i.e., change of the beam quality) affects the stemless detector's response in comparison to the free in-air calibration, in two ways; changing the secondary electrons produced in the detector's wall and electrode which contribute to the stemless detector dose, and changing the absorbed dose in the detector's wall in the water phantom relative to the free in-air calibration.

Considering a stemless NE2571 ion chamber, it is constructed with an aluminum central electrode with 0.1 cm diameter and a graphite wall with 0.036 cm thickness. The photoelectric cross-section is proportional to $\frac{1}{E^3}$ where E is the energy of the

incident photon beam. For a specific photon beam, the photoelectric cross-section of the stemless NE2571 ion chamber in the water phantom relative to the in-air calibration is proportional to

$$(\sigma_{pe})_{air}^{water} = \left(\frac{E_{air}}{E_w} \right)^3 \quad (6.3)$$

where E_{air} and E_w are the photon beam's energies for in-air and in-water-phantom calibration respectively. As mentioned above, using the E_{mean} of the x-ray beams, one can approximately calculate the change of the photoelectric cross-section for the stemless NE2571 ion chamber in the water respect to the in-air calibration. If the average energy of a beam increases with depth in water, eqn 6.3 tells us that the relative photoelectric cross-section decreases which means fewer secondary electrons from photoelectric interactions, are produced in the wall and electrode; as a result, there would be an under response from the NE2571 ion chamber respect to the in-air calibration which increases the $P_{E,\theta}$ correction factor (see eqn 6.2). An over response corresponds to a x-ray beam in which the E_{mean} decreases with depth in the water phantom and decreases the $P_{E,\theta}$ correction factor.

The percentage of the secondary electrons contribution to the stemless detector dose required a separate study with a full consideration of the change in the beam quality (i.e., the change in the angular distribution of the photons should be considered in addition to the change in the E_{mean}). In addition to the photoelectric effect, Compton scattering is also important in the range of energy used in this thesis. The energy absorption in the detector wall due to the change in the beam quality in the water phantom respect to the in-air calibration is another reason for the variation of the $P_{E,\theta}$ correction factor. The mass-energy absorption coefficient ratio of graphite to air shows a rapid increase (i.e., from 0.4 to 1.0) for photon energies between 40 keV - 100 keV. Knight and Nahum³² showed that for a graphite walled detector, this effect can be considerable.

A comparison of $P_{E,\theta}$ correction factor in this thesis with the same correction factor calculated by Seuntjens and Verhaegen³ (as discussed in chapter 5, page 20) is shown in fig 6.6.

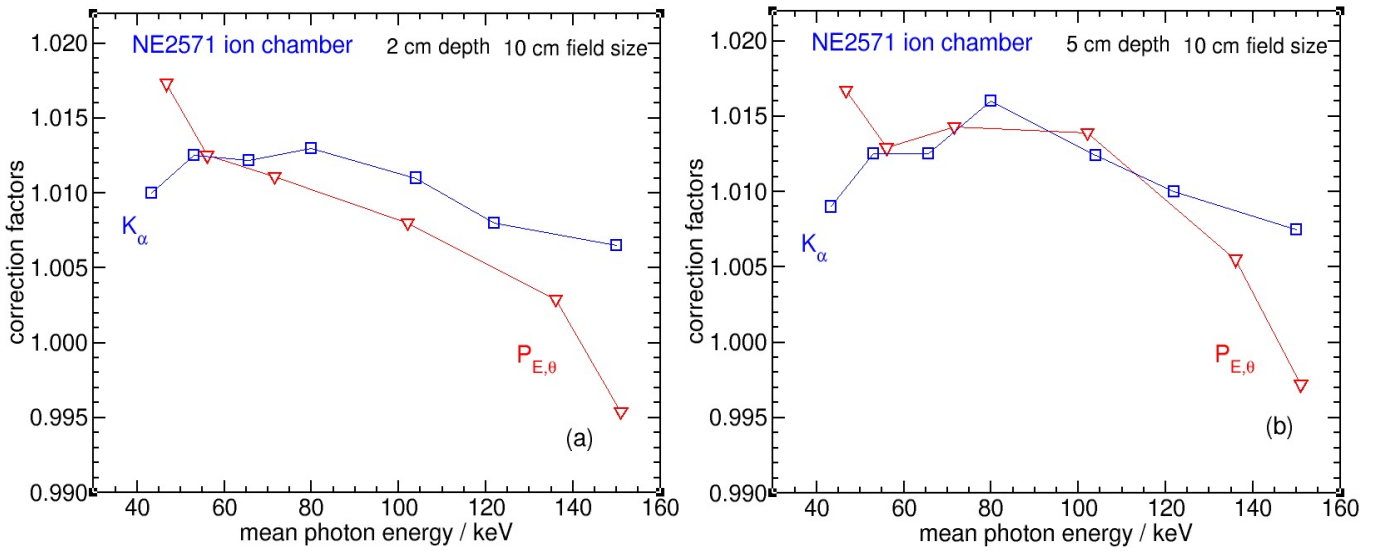


Figure 6.6: The variation of $P_{E,\theta}$ correction factor with the mean energy of the incident photon beam at 2 cm (a) and 5 cm (b) depth in water for 10 cm field size. K_{α} is the same correction factor calculated by Seuntjens and Verhaegen³. The statistical uncertainties are 0.1% for all values.

At 2 cm depth in water, the $P_{E,\theta}$ correction factor is always decreasing with the mean energy of the incident photon beams and the maximum variation is 2.3%. The variation of the $P_{E,\theta}$ value at 5 cm depth in water is up to 2%. The disagreement between our $P_{E,\theta}$ values and K^{SV} is greater at 2 cm depth in comparison to the 5 cm depth in water. The most likely reason for the disagreement is that the x-ray tube potentials and filtrations are different between their work and ours. The maximum deviation between the values of this thesis and K^{SV} is 1.1% for both 2 cm and 5 cm depth in water.

6.1.2 The $P_{stem,w}$ correction factor

$P_{stem,w}$ is another component of the $P_{Q,cham}$ correction factor and calculated using eqn 5.15 (page 43). It accounts for the displacement of water caused by the stem part of the detector relative to the stem effect for the in-air calibration. In general, the number of scattered photons produced in the stem affects the detector's cavity dose. For example, for in-water measurement, dose to the detector's cavity increases (decreases) if there are more (fewer) scattered photons produced in the stem than in water. This also applies to the in-air measurement but the number of scattered photons produced in the

stem is always larger than in air. The $P_{stem,w}$ correction factor is the effect of stem for the in-water measurement relative to the in-air calibration. The $P_{stem,w}$ values for the NE2571 ion chamber are shown in figs 6.2 - 6.5. The values of $P_{stem,w}$ correction factor is always larger than unity for all beam qualities, depths, and field sizes indicating that the stem effect for in-water measurement is always larger than the in-air calibration. For 5 cm field size, the $P_{stem,w}$ increases up to 3% as depth increases from 2 cm to 11 cm at lower energy beam while this variation decreases for higher energy beam. A comparison between the stem correction factors in this thesis and the values of Seuntjens and Verhaegen is shown in fig 6.7.

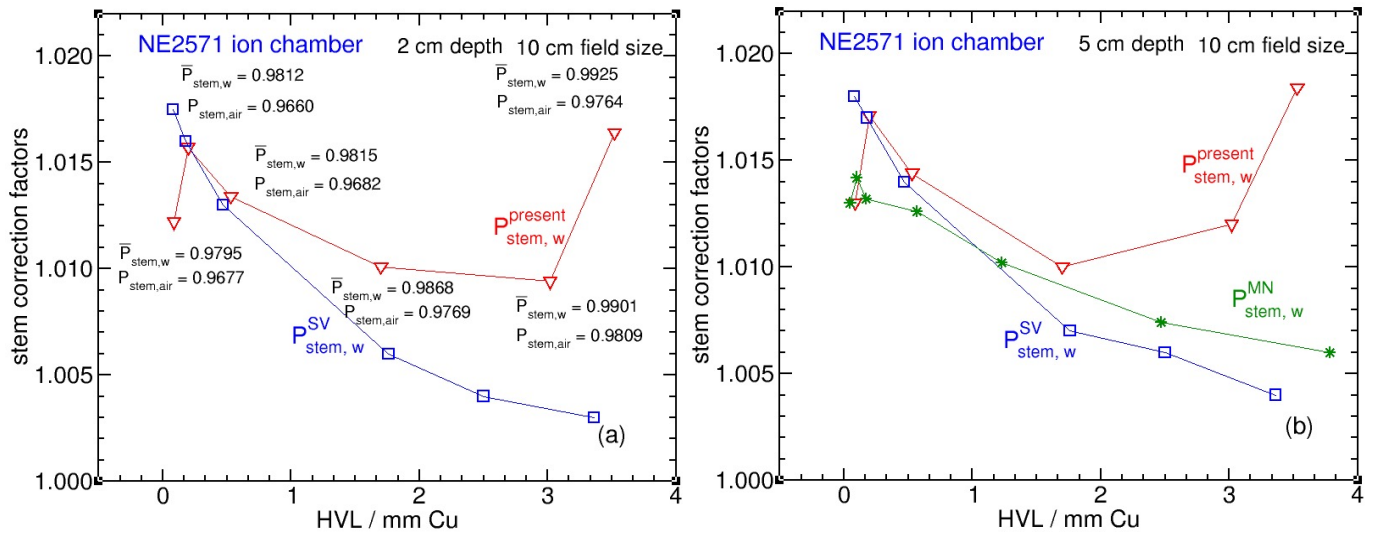


Figure 6.7: A comparison between the stem correction factors in this thesis ($P_{stem,w}^{present}$), the values of Seuntjens and Verhaegen³ ($P_{stem,w}^{SV}$), and calculated values of Ma and Nahum²⁷, at 2 cm depth(a) and 5 cm depth in water (b). The values of the $\bar{P}_{stem,w}$ and $P_{stem,air}$ components of $P_{stem,w}$ as calculated in this thesis are also shown in the left panel. The statistical uncertainties are less than 0.1% for all values.

Fig 6.7 shows 1% and 2% deviations between our calculation and the $P_{stem,w}^{SV}$ at 2 cm depth for the lowest and highest energies respectively. This inconsistency which can also be seen at 5 cm depth in water, might be a consequence of the differences between the beam qualities (i.e., x-ray tube potentials and filtrations) in these two studies. In addition, the definition of the $P_{stem,w}$ is different in this thesis and Seuntjens and Verhaegen work which was discussed in section 5.6 (page 45). Another reason for this inconsistency must be due to the geometry of the stem which was considered as a full aluminum bar in Seuntjens and Verhaegen's work instead of the full geometry used

in this thesis.

6.1.3 The P_{dis} correction factor

The last component of the $P_{Q, cham}$ correction factor is the P_{dis} correction which takes into account the change in the air kerma in water from the displacement of water caused by the detector body. This correction factor does not depend on the materials of the detector but the size.

As discussed in the previous chapter, the variation of the P_{dis} correction factor is investigated by separating the effect of the primary photons and the scattered photons on the P_{dis} correction factor (see eqn 5.25, page 49). Figs 6.8 - 6.12 show the values of $\Delta_p K_{air}^w$, $\Delta_s K_{air}^w$, and \bar{K}_{air}^w at 2 cm, 5 cm, 8 cm and 11 cm depth in a water phantom for the NE2571 ion chamber.

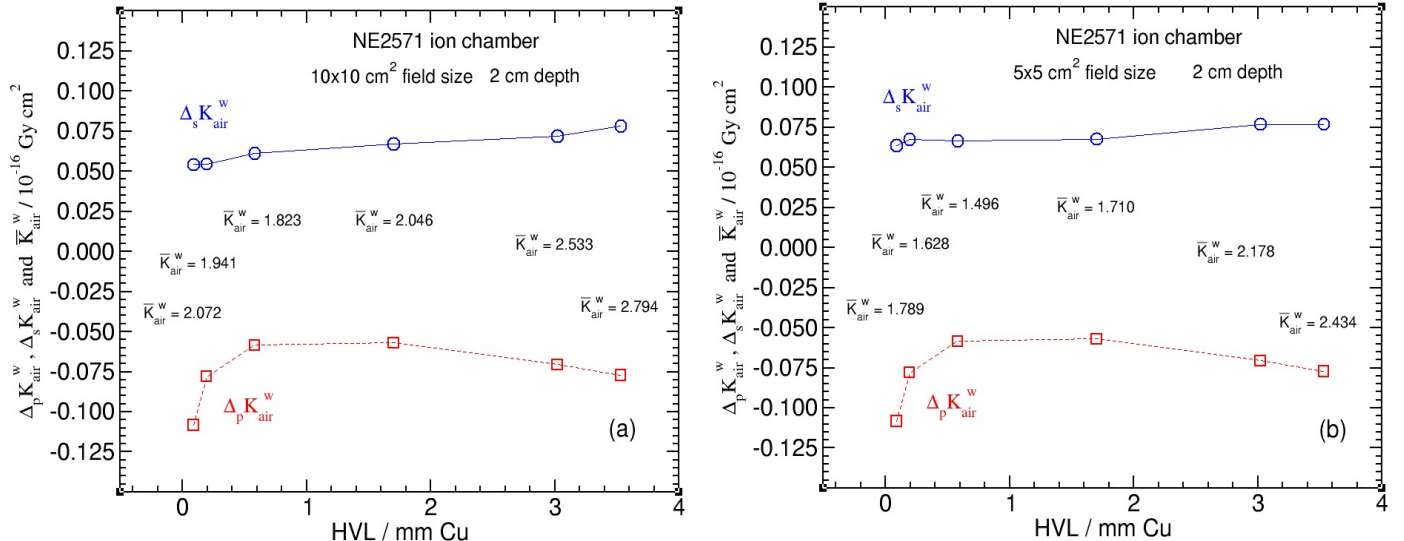


Figure 6.8: Calculated values for $\Delta_p K_{air}^w$ (eqn 5.30), $\Delta_s K_{air}^w$ (eqn 5.33), and \bar{K}_{air}^w (eqn 5.27) at 2 cm depth in water are shown for six different x-ray beams with 10 cm (a) and 5 cm (b) field sizes. The statistical uncertainties are less than 0.1 %.

Note that for a particular depth in the water phantom, $\Delta_p K_{air}^w$ is the same for 10 cm and 5 cm field size beams, thus $\Delta_p K_{air}^w$ is not field size dependent while the $\Delta_s K_{air}^w$ varies with the field size. The number of primary photons decreases as depth increases; as a result, $|\Delta_p K_{air}^w|$ is depth dependent and decreases with increasing depth.

Figs 6.8, 6.9, 6.10 and 6.12 indicate that the values of $\Delta_p K_{air}^w$ and $\Delta_s K_{air}^w$ get closer to each other with increasing depth in the water phantom. This is due to the decreasing

of the total number of photons as depth increases.

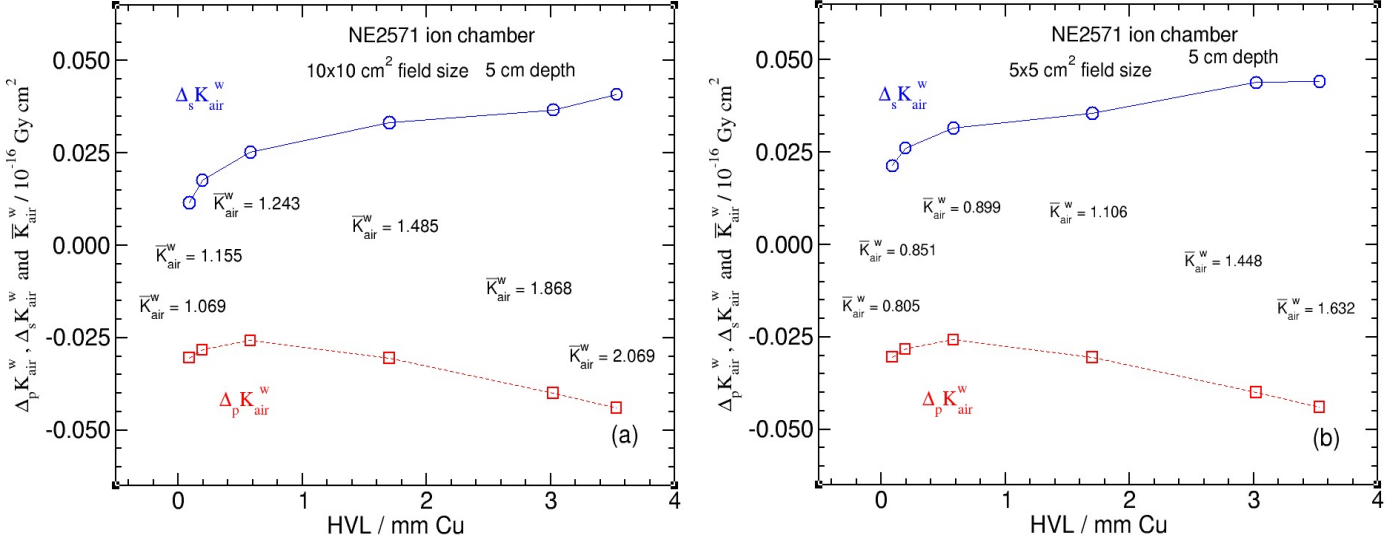


Figure 6.9: Same as fig 6.8 but at 5 cm depth.

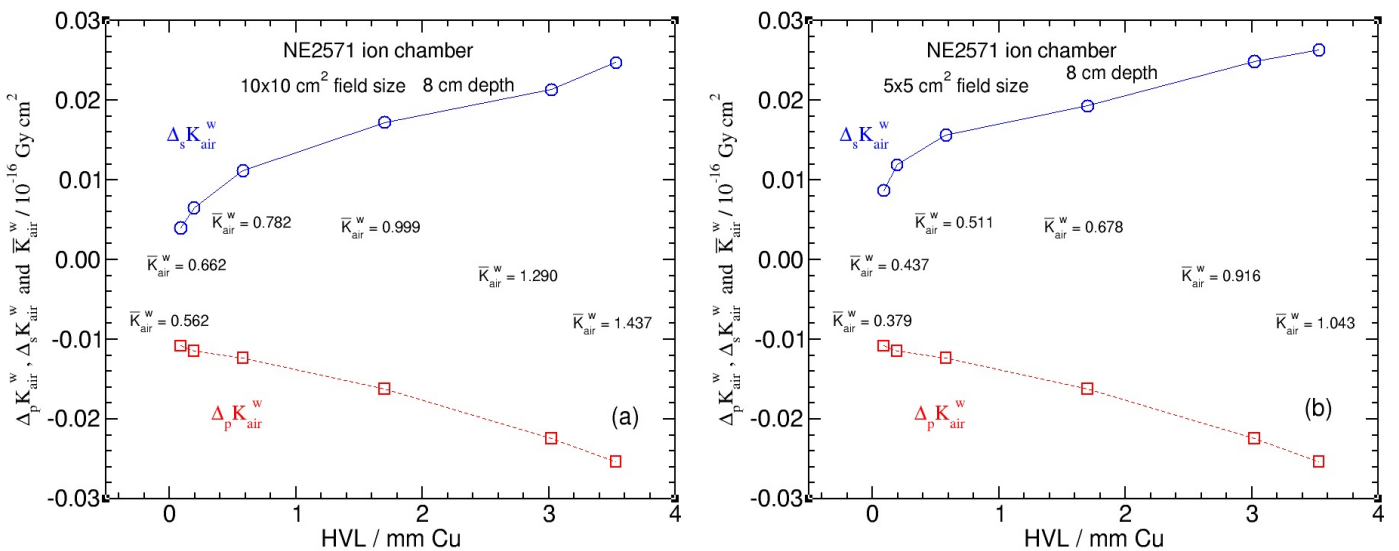


Figure 6.10: Same as fig 6.8 but at 8 cm depth.

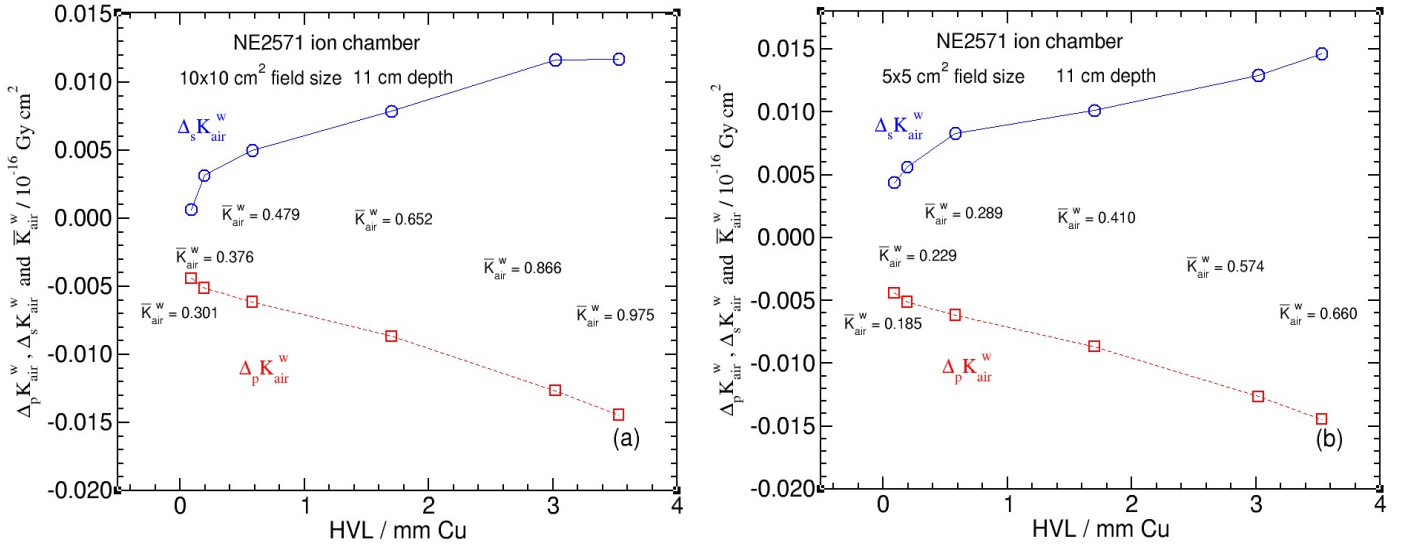


Figure 6.11: Same as fig 6.8 but at 11 cm depth.

One can calculate the P_{dis} correction factor for the NE2571 ion chamber at a desired point using the equation 5.35 (page 52) and the data in figs 6.8 - 6.12. For example P_{dis} for 100 kV (HVL: 0.088 mm Cu) x-ray beam and 10 cm field size at 2 cm depth in the water phantom can be obtained as follows :

$$P_{dis} = 1 + \frac{\Delta_p K_{air}^w + \Delta_s K_{air}^w}{\bar{K}_{air}^w} = 1 + \frac{-0.108 + 0.054}{2.072} = 0.974 \quad (6.4)$$

which is consistent with the value of P_{dis} in fig 6.2 (a). This is an example where attenuation effect dominated the effect of scattered photons since $|\Delta_p K_{air}^w| > \Delta_s K_{air}^w$ and $P_{dis} < 1$.

An opposite effect can be seen for 150 kV x-ray beam (HVL: 0.581 mm Cu) for 5 cm field size at 11 cm depth (see fig 6.5 (b), page 58). Using fig 6.12, one can calculate the P_{dis} as follows,

$$P_{dis} = 1 + \frac{\Delta_p K_{air}^w + \Delta_s K_{air}^w}{\bar{K}_{air}^w} = 1 + \frac{-0.00615 + 0.00829}{0.289} = 1.007 \quad (6.5)$$

In this case, $|\Delta_p K_{air}^w| < \Delta_s K_{air}^w$ and $P_{dis} > 1$ which indicates that the effect of scattered photons dominated the attenuation effect.

A comparison between displacement correction factor calculated in this study (P_{dis}), Ma and Nahum², and Seuntjens and Verhaegen³ is shown in fig 6.12.

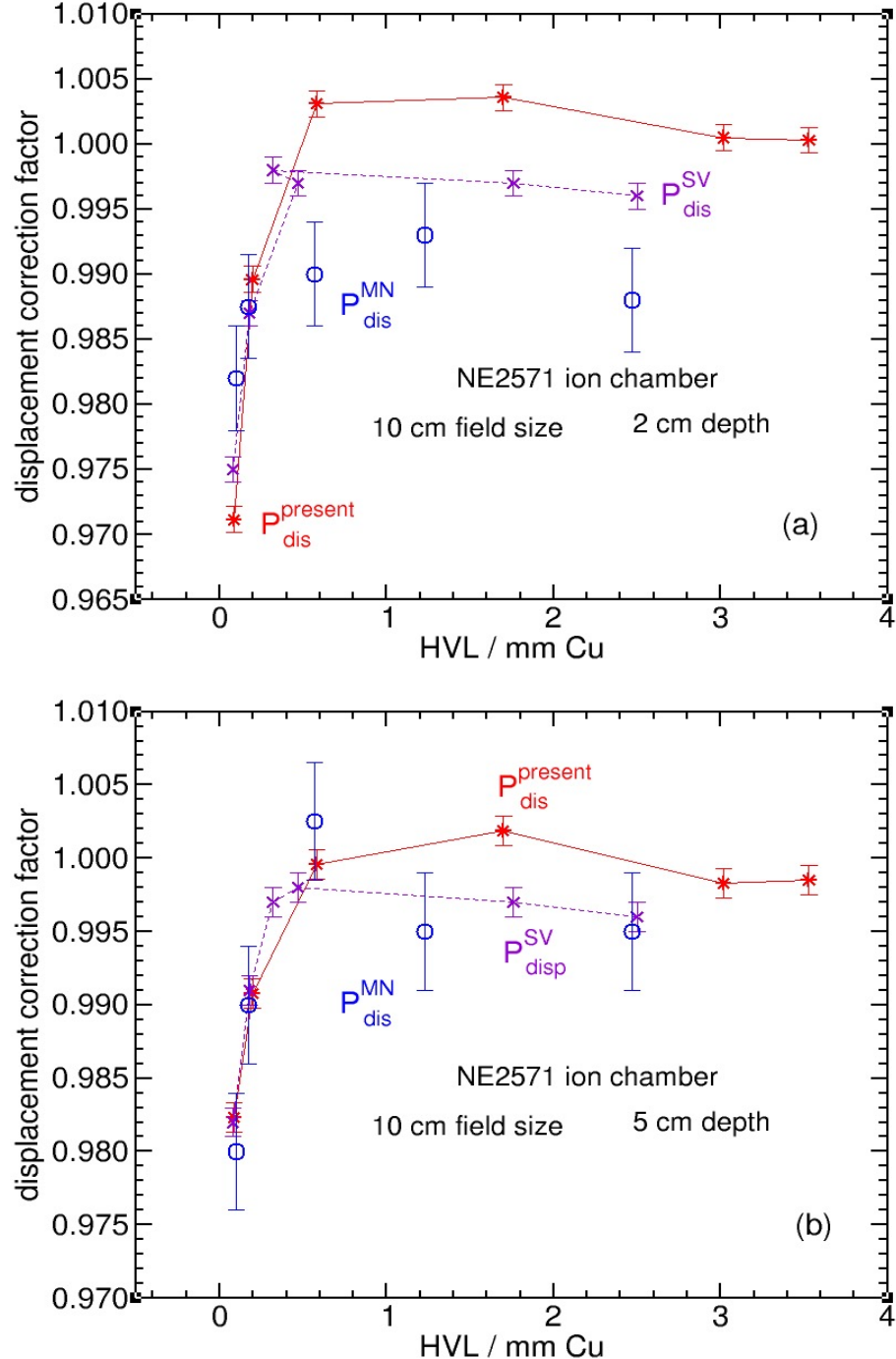


Figure 6.12: Displacement correction factor for an NE2571 ion chamber at 2 cm (a) and 5 cm (b) depth in a water phantom. For comparison, the displacement correction factors calculated by Ma and Nahum² (P_{dis}^{MN}), and Seuntjens and Verhaegen³ (P_{dis}^{SV}) are also presented.

At 2 cm depth in water there are up to 1.5 % disagreement between the results of this study and the other two papers. This inconsistency is lower at 5 cm depth where the disagreement is less than 0.8 %. The most likely reason for this differences is that the x-ray beams are not exactly the same in terms of x-ray tube potentials and the filtrations used for the beam quality specifications which shows neither x-ray tube potential nor HVL are suitable to specify uniquely beam quality.

Considering the three different components of the $P_{Q,chl}$ correction factor (i.e., $P_{E,\theta}$, $P_{stem,w}$, and P_{dis}) at 2 cm depth with 10 cm field size, for the 100 kV x-ray beam (HVL: 0.088 mm Cu) the value of the $P_{E,\theta}$ correction factor in this thesis is greater than the values of Seuntjens and Verhaegen by a 0.7% (see fig 6.6, page 61) while the values of $P_{stem,w}$ and P_{dis} are less than their values by a 0.5% and a 0.4% respectively (see figs 6.7 (a) and 6.12 (a), pages 59 and 63). For 120 kV (HVL: 0.195 mm Cu) and 150 kV (HVL: 0.581 mm Cu) x-ray beams, our values of these three components are almost in agreement with Seuntjens and Verhaegen's values. For higher energy x-ray beams, our $P_{E,\theta}$ values are less than their values and the maximum deviation is up to 1.1% for the 300 kV x-ray beam (HVL: 353 mm Cu) while our values for the $P_{stem,w}$ and P_{dis} correction factors are greater than Seuntjens and Verhaegen's value with maximum deviations of a 1.5% and 0.7% respectively. Considering these differences discussed above, the overall correction factor, $P_{Q,chl}$, is less than the TG-61 values for the 100 kV (HVL: 0.088) x-ray beam. For 120 kV (HVL: 0.195 mm Cu) and 150 kV (HVL: 0.581 mm Cu) x-ray beams the $P_{Q,chl}$ correction factors are in agreement with the values of the TG-61 protocol and for higher energy beam our $P_{Q,chl}$ values are somewhat greater (see fig 6.1, page 54).

6.2 The Exradin A16 ion chamber

The second ion chamber studied is the Exradin A16 ion chamber. Its air cavity is 0.014 times that of an NE2571 ion chamber and is categorized as a micro-chamber. In this section, the values of the $P_{Q,cham}$ correction factor and its components with field size, depth, and beam quality are presented.

The variation of the $P_{Q,cham}$ correction factor with HVLs for three different field sizes is shown in fig 6.13.

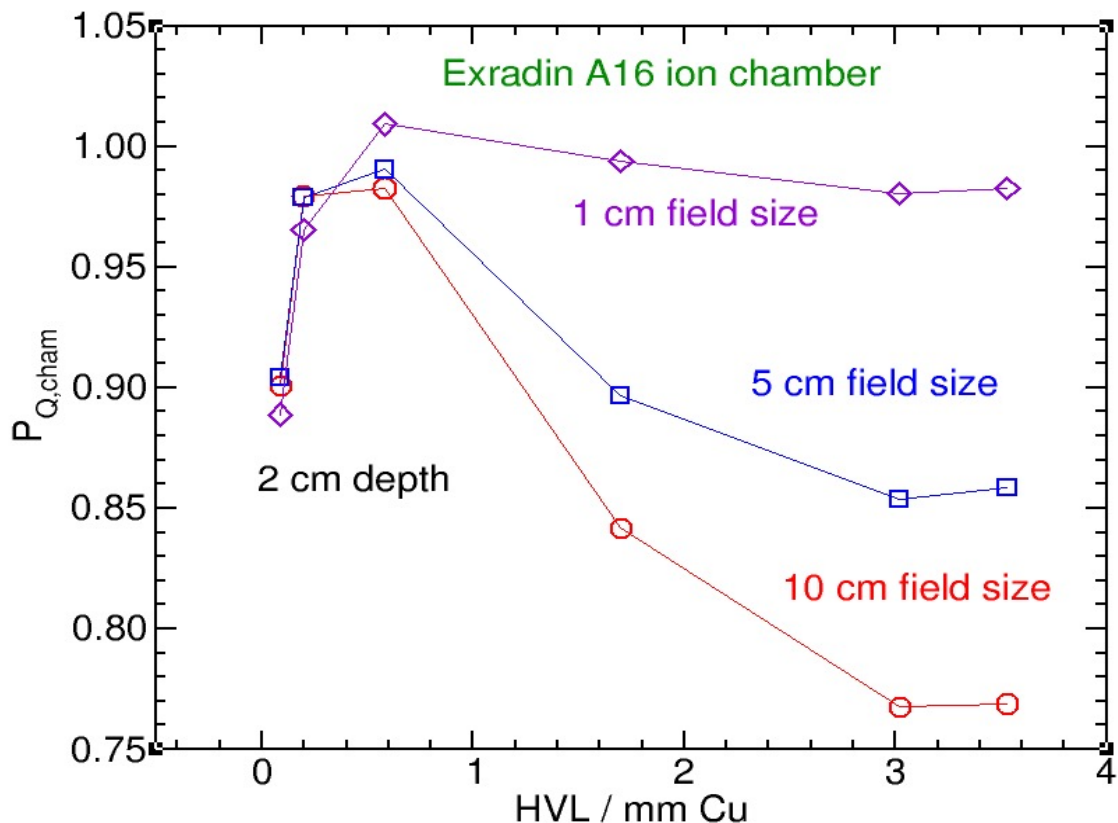


Figure 6.13: The $P_{Q,cham}$ values for the Exradin A16 ion chamber at 2 cm depth for 1 cm, 5 cm and 10 cm field sizes and x-ray tube potential between 100 kV - 300 kV. The statistical uncertainties on the values are less than 0.1%.

For 100 kV (HVL: 0.088 mm Cu) and 120 kV(HVL: 0.195 mm Cu) x-ray beams, the $P_{Q,cham}$ correction factor varies by up to 2% between 1 cm to 10 cm field sizes. This variation increases for x-ray beams with greater HVLs and its maximum is 26% for the 300 kV x-ray beam (HVL: 3.53 mm Cu).

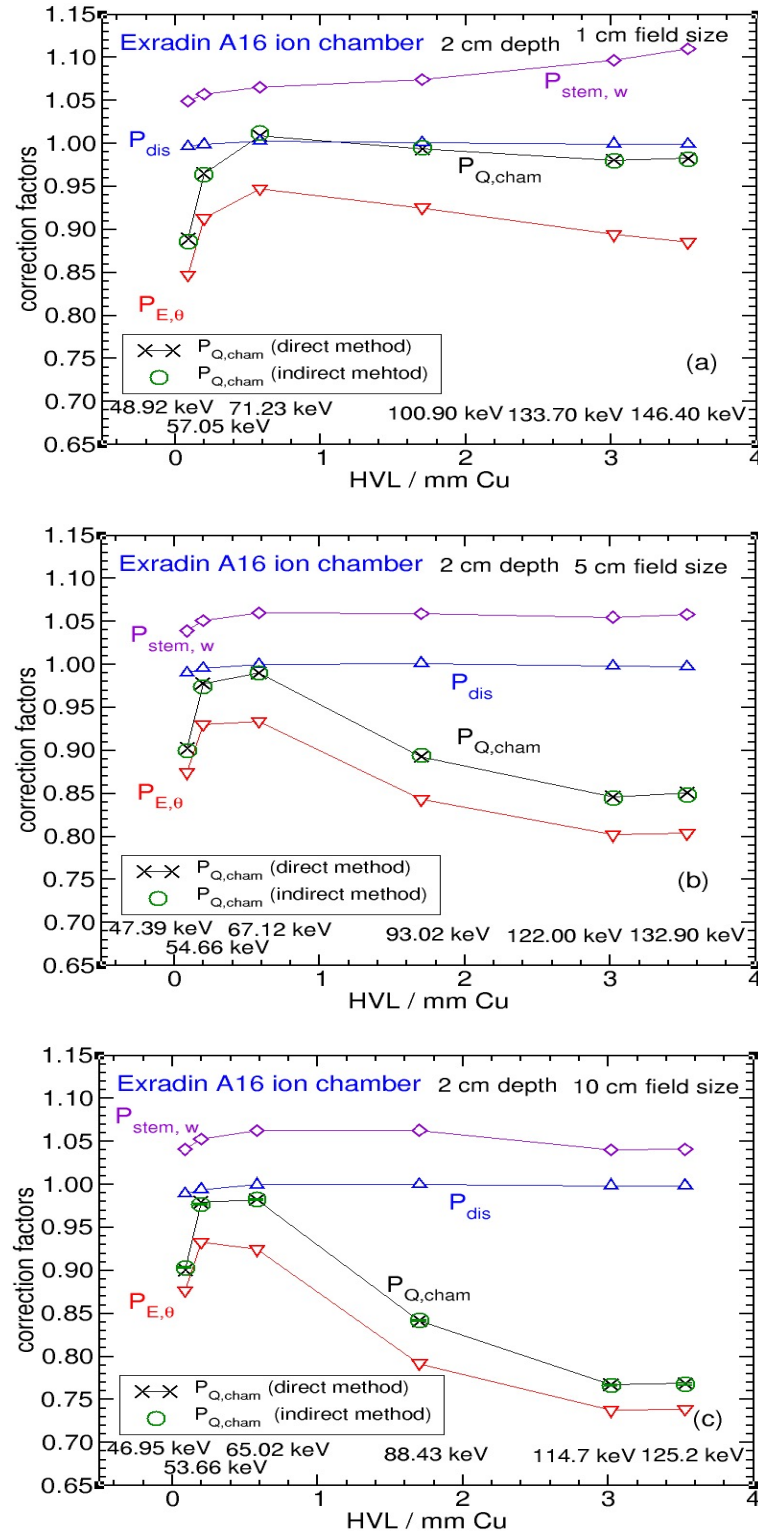


Figure 6.14: The variations of the $P_{Q,\text{cham}}$ correction factor and its components for the Exradin A16 ion chamber with HVLs and for 1 cm (a), 5 cm (b), and 10 cm (c) field sizes at 2 cm depth in the water phantom.

To understand the behaviour of the $P_{Q,cham}$, variations of the $P_{E,\theta}$, $P_{stem,w}$, and P_{dis} correction factors have been studied for an Exradin A16 ion chamber and the results at 2 cm depth are shown in fig 6.14. Unlike the case of the NE2571 ion chamber where there were minor discrepancies, the values from the direct and indirect methods are in very good agreement as should be the case.

Fig 6.14 shows that the P_{dis} correction factor is not as important as the $P_{E,\theta}$ and $P_{stem,w}$ correction factors since its values are close to unity with a maximum 1% deviation for the 100 kV x-ray beam (HVL: 0.088 mm Cu). This reflects the small size of the chamber. The contribution of the $P_{stem,w}$ correction factor to the overall correction factor (i.e., $P_{Q,cham}$) is larger than 5% due to the more important effect of stem correction factor for free-in-air calculation ($P_{stem,air}$). The variation of the $P_{stem,w}$ correction with HVL is more dramatic at smaller field sizes; its variation is up to 7% for a 1 cm field between 100 kV and 300 kV x-ray beams. Considering the field sizes in fig 6.14, the variation of the $P_{E,\theta}$ correction factor plays a more important role in the $P_{Q,cham}$ correction factor in comparison with the other two components for higher energies. The individual components are discussed in the following sections.

The maximum variation of the $P_{E,\theta}$ correction factor with depth for the 1 cm field size is 15.5% from 2 cm to 8 cm depth for the 100 kV x-ray beam (HVL: 0.088 mm Cu). This variation is up to 13% for 5 cm and 10 cm field sizes.

The variation of the $P_{Q,cham}$ correction factor and its components for the Exradin A16 ion chamber with HVLs for three different field sizes at depth 5 cm and 8 cm in the water phantom are shown in figs 6.15 and 6.16 respectively.

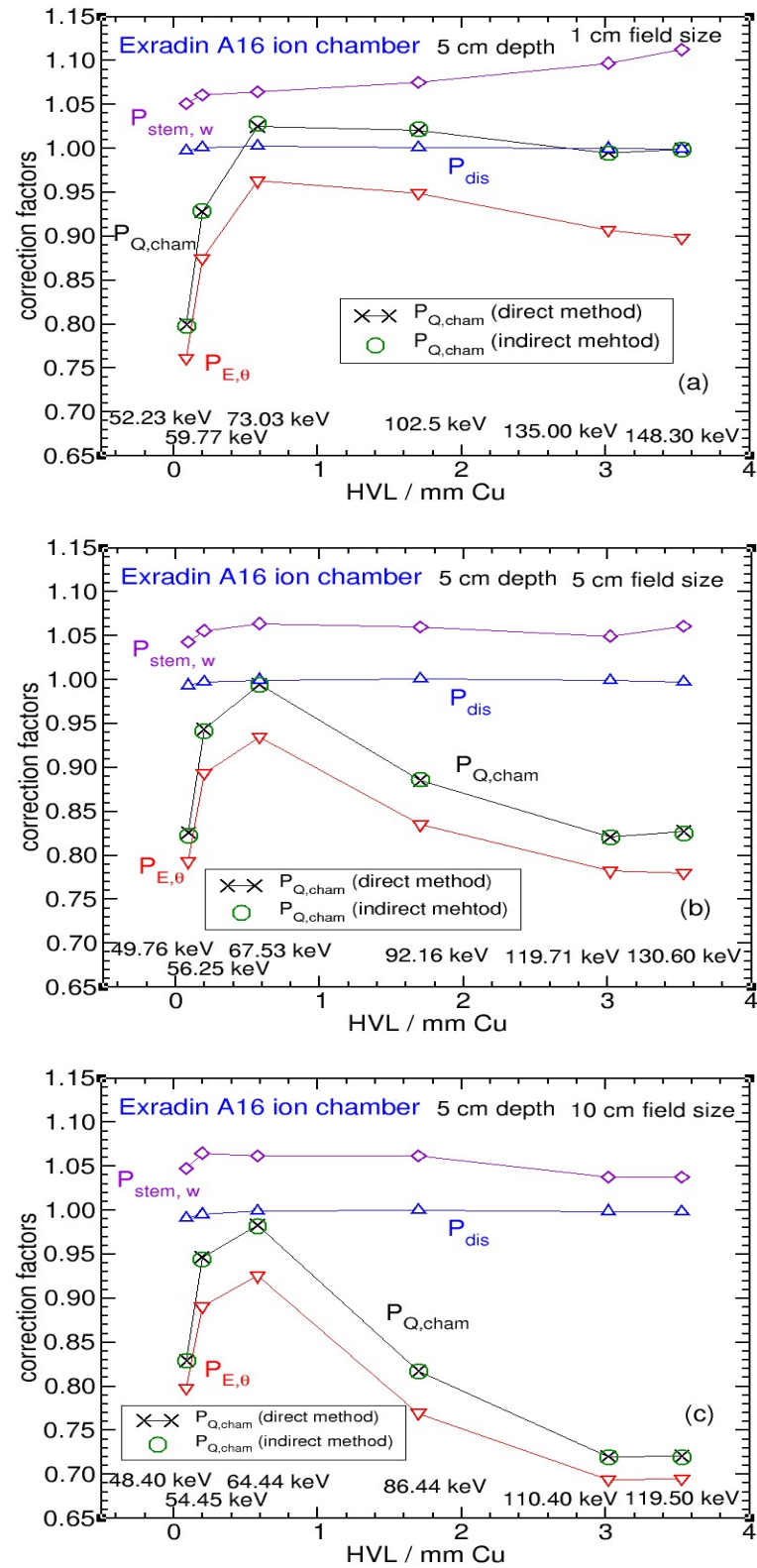


Figure 6.15: Same as fig 6.14 but at 5 cm depth in the water phantom.

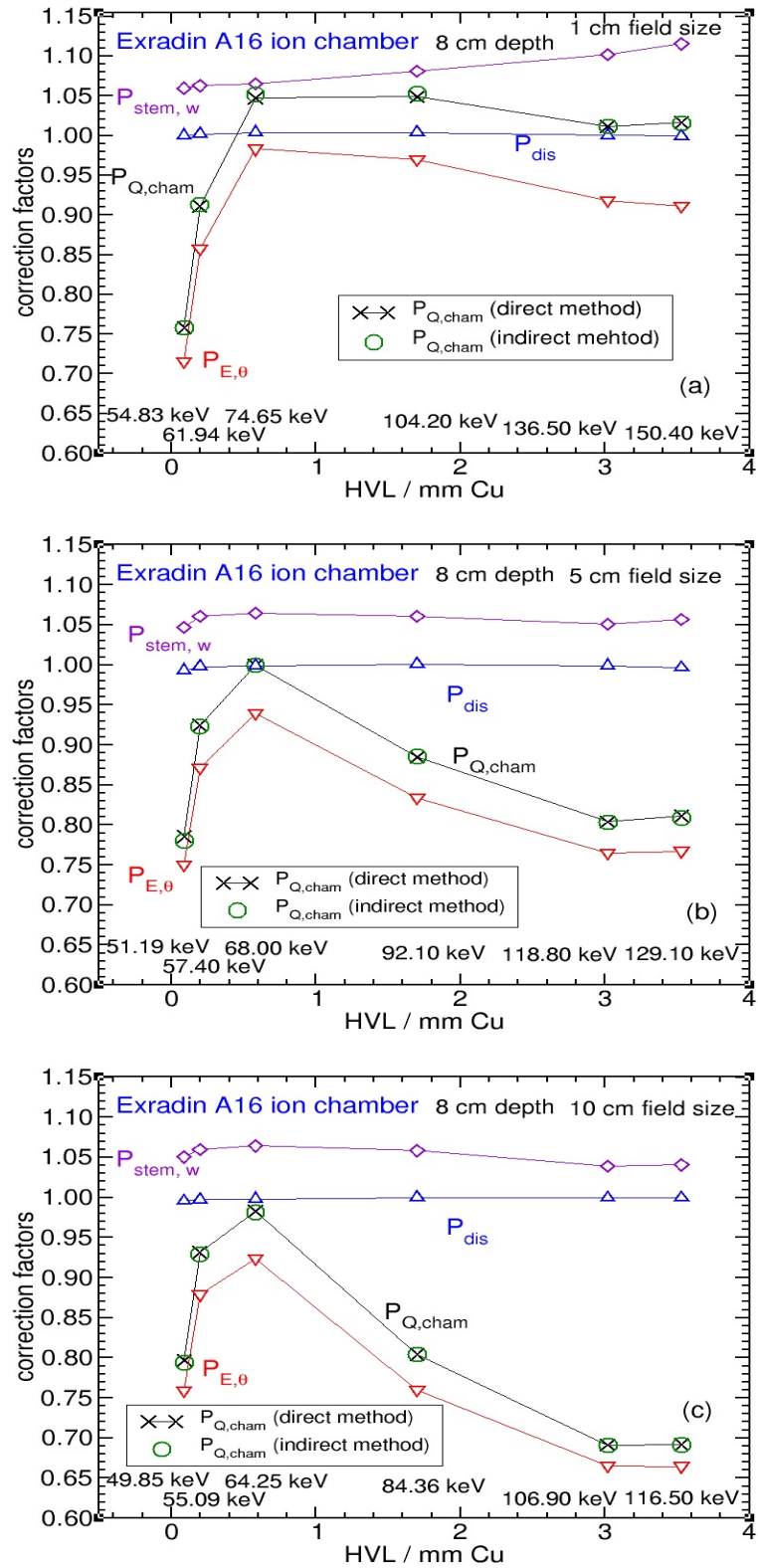


Figure 6.16: Same as fig 6.14 but at 8 cm depth in the water phantom.

6.2.1 The $P_{E,\theta}$ correction factor

As explained in section 5.6, the $P_{E,\theta}$ correction factor can be calculated using the following equation,

$$P_{E,\theta} = \frac{\frac{K_{air}^w}{K_{air}^{free\ in-air}}}{\frac{D_{cav}^{w,stemless}}{D_{cav}^{air,stemless}}} \quad (6.6)$$

Eqn 6.6 shows the relation between the $P_{E,\theta}$ and the cavity dose in the stemless detector (i.e., the Exradin A16 ion chamber) in the water phantom ($D_{cav}^{w,stemless}$). Generally speaking, for kilo-voltage x-ray beams, the photoelectric interaction becomes important especially in the high-Z electrode detector. The Exradin A16 ion chamber has an electrode made of high-Z materials such as silver which produce lots of secondary electrons due to the photoelectric interaction between photons and electrode materials. These secondary electrons contribute to the cavity dose of the Exradin A16 ion chamber and increase it. Considering the over-reading of the Exradin A16 ion chamber due to the photoelectric interaction, the $P_{E,\theta}$ correction factor decreases from unity as opposed to the NE2571 ion chamber where the $P_{E,\theta}$ correction factor is almost always above unity. Note that the electrode of the NE2571 ion chamber is made of aluminum which is not a high-Z material in comparison to the Exradin A16 ion chamber electrode. At larger field size, the $P_{E,\theta}$ correction factor decreases more dramatically due to the increase of the scattered photons at the central axis of the beam. These scattered photons have lower energy where there are more photoelectric interactions in comparison to the in-air calculation. As a result, the ratio of $\frac{D_{cav}^{w,stemless}}{D_{cav}^{air,stemless}}$ increases and the $P_{E,\theta}$ correction factor decreases.

The effect of high-Z materials in the electrode of the Exradin A16 ion chamber for kilo-voltage x-ray beams had been studied by Muir and Rogers²² as well as Snow et al³³ where they concluded that high-Z materials should not be used in the electrode of an ionization chamber and chambers containing high-Z components may not be suitable for kilo-voltage x-ray dosimetry.

To investigate the effect of secondary electrons from the central electrode on the $P_{Q,cham}$ correction factor (i.e., due to the $P_{E,\theta}$ variation) for the Exradin A16 ion chamber, the $P_{Q,cham}$ factor was calculated using an identical Exradin A16 ion chamber but with an ECUT = 1 MeV in the electrode to make sure that none of the

secondary electrons produced in the electrode contribute to the cavity dose. Also, the Exradin A16 ion chamber with graphite and air electrodes was considered with ECUT=0.521 MeV. The results are shown in fig 6.17.

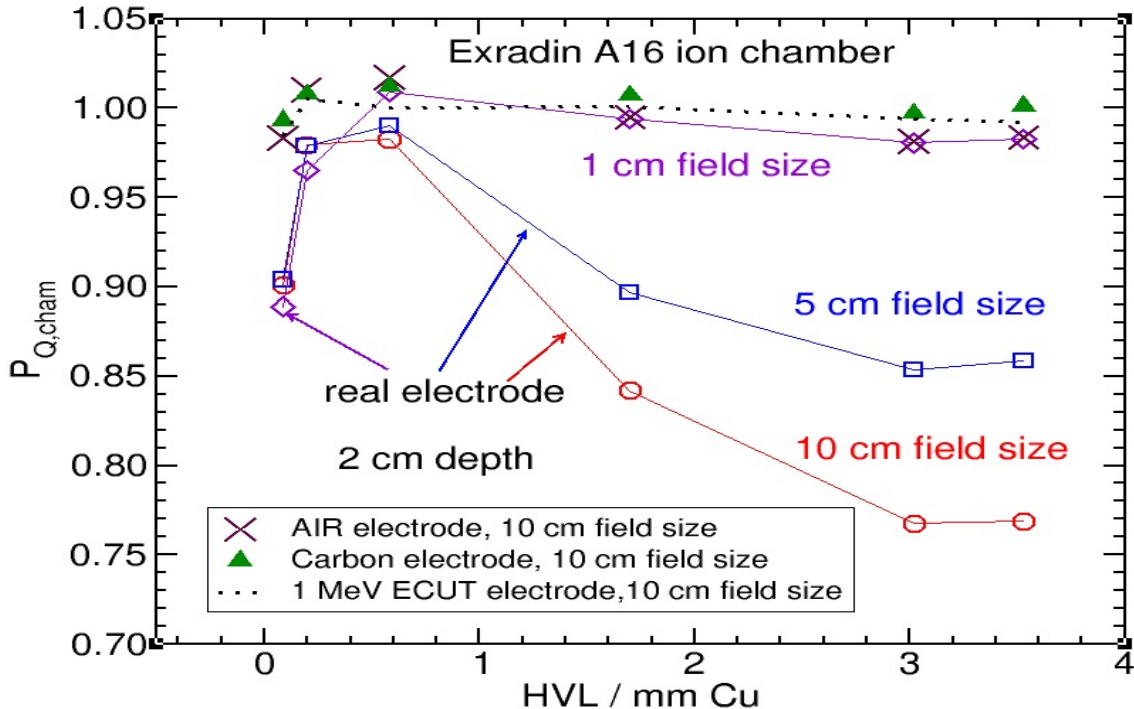


Figure 6.17: The $P_{Q,\text{cham}}$ values for the Exradin A16 ion chamber with different electrodes at 2 cm depth for 1 cm, 5 cm and 10 cm field sizes and x-ray tube potential between 100 kV - 300 kV used in this study. The statistical uncertainties on the values are less than 0.1%

Fig 6.17 shows the dependency of the $P_{Q,\text{cham}}$ correction factor on the materials of the Exradin A16's electrode. The variation of the $P_{Q,\text{cham}}$ values with HVL decreases significantly either by eliminating the secondary electrons produced in the electrode of the Exradin A16 ion chamber or by having an air electrode or a carbon electrode.

6.2.2 The $P_{\text{stem},w}$ correction factor

The $P_{\text{stem},w}$ correction factor for the Exradin A16 ion chamber is large in comparison with the NE2571 ion chamber. As discussed in section 5.6 (page 39), the $P_{\text{stem},w}$

correction factor can be calculated using

$$P_{stem,w} = \frac{\bar{P}_{stem,w}}{P_{stem,air}} = \frac{\frac{D_{cav}^{w,stemless}}{D_{cav}^w}}{\frac{D_{cav}^{air,stemless}}{D_{cav}^{air}}} \quad (6.7)$$

where $\bar{P}_{stem,w}$ and $P_{stem,air}$ are the stem correction for the in-water and free in-air measurements. Fig 6.18 shows the $P_{stem,w}$ correction factor at 2 cm depth in the water phantom with the contribution of the $\bar{P}_{stem,w}$ and $P_{stem,air}$ factors for the 1 cm and 10 cm field size beam.

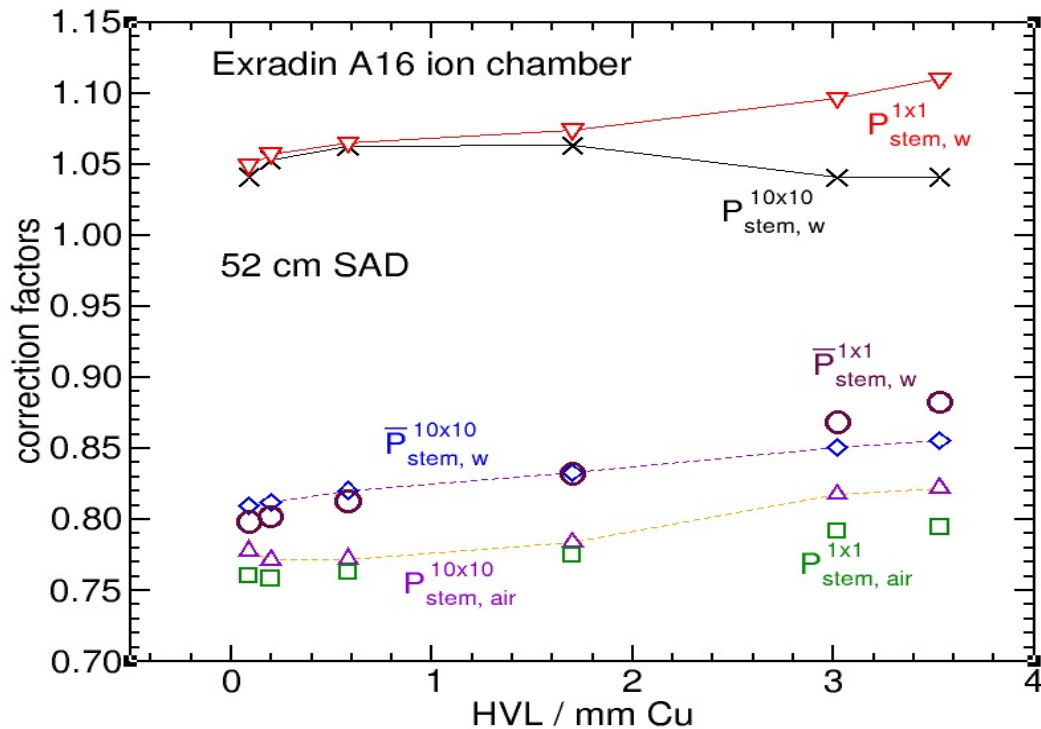


Figure 6.18: The $P_{stem,w}$ values for the Exradin A16 ion chamber with the contribution of the $\bar{P}_{stem,w}$ and $P_{stem,air}$ at 2 cm depth for 1 cm and 10 cm field sizes and x-ray tube potential between 100 kV - 300 kV. The statistical uncertainties on the values are 0.1%

Fig 6.18 shows that the $\bar{P}_{stem,w}$ correction factor is larger (closer to unity) than $P_{stem,a}$ for all HVLs and 2 different field sizes (i.e., 1x1 cm² and 10x10 cm²). For low energy beams, the stem correction factor for the in water and free in-air measurements are greater (closer to unity) for larger field size while this is vice-versa at higher energy beams.

The $P_{stem,w}$ correction factor for the Exradin A16 ion chamber is always above unity indicating that the stem effect is smaller for the in-water measurement relative to the in-air calibration. For the 1 cm field size, a maximum increase of 1% for $P_{stem,w}$ with increasing depth is observed at the lowest energy. The $P_{stem,w}$ correction factor always increases with increasing the HVLs at 1 cm field size as opposed to the 5 cm and 10 cm field sizes where the $P_{stem,w}$ value is almost constant or decreases slightly at greater HVLs. The maximum variation of the $P_{stem,w}$ correction factor with HVL is 5.5% and occurs for the 1 cm field size and 2 cm depth. A comparison between the $P_{stem,w}$ correction factors of the Exradin A16 and NE2571 ion chambers shows that the values of $P_{stem,w}$ are greater for the Exradin A16 since its stem is made of high-Z materials relative to the stem of the NE2571 ion chamber.

6.2.3 The P_{dis} correction factor

The last component of the $P_{Q,cham}$ correction factor is the P_{dis} correction. Since the cavity size of the Exradin A16 ion chamber is so small, its P_{dis} correction factor has a smaller effect on the variation of the $P_{Q,cham}$ values in comparison to the other two components for the Exradin A16 ion chamber. The maximum deviation of the P_{dis} correction factor is 1% for the 100 kV x-ray beam (HVL: 0.088 mm Cu) and 10 cm field size at 2 cm depth. This variation is much smaller relative to the P_{dis} correction factor of the NE2571 ion chamber which is due to the smaller size of detector's body of the Exradin A16 ion chamber (see chapter 4) resulting a smaller displaced water value.

To explain the variation of the P_{dis} correction factor for the Exradin A16 ion chamber, the effects of the primary photons and scattered photons were studied using the same method as used for the NE2571 ion chamber.

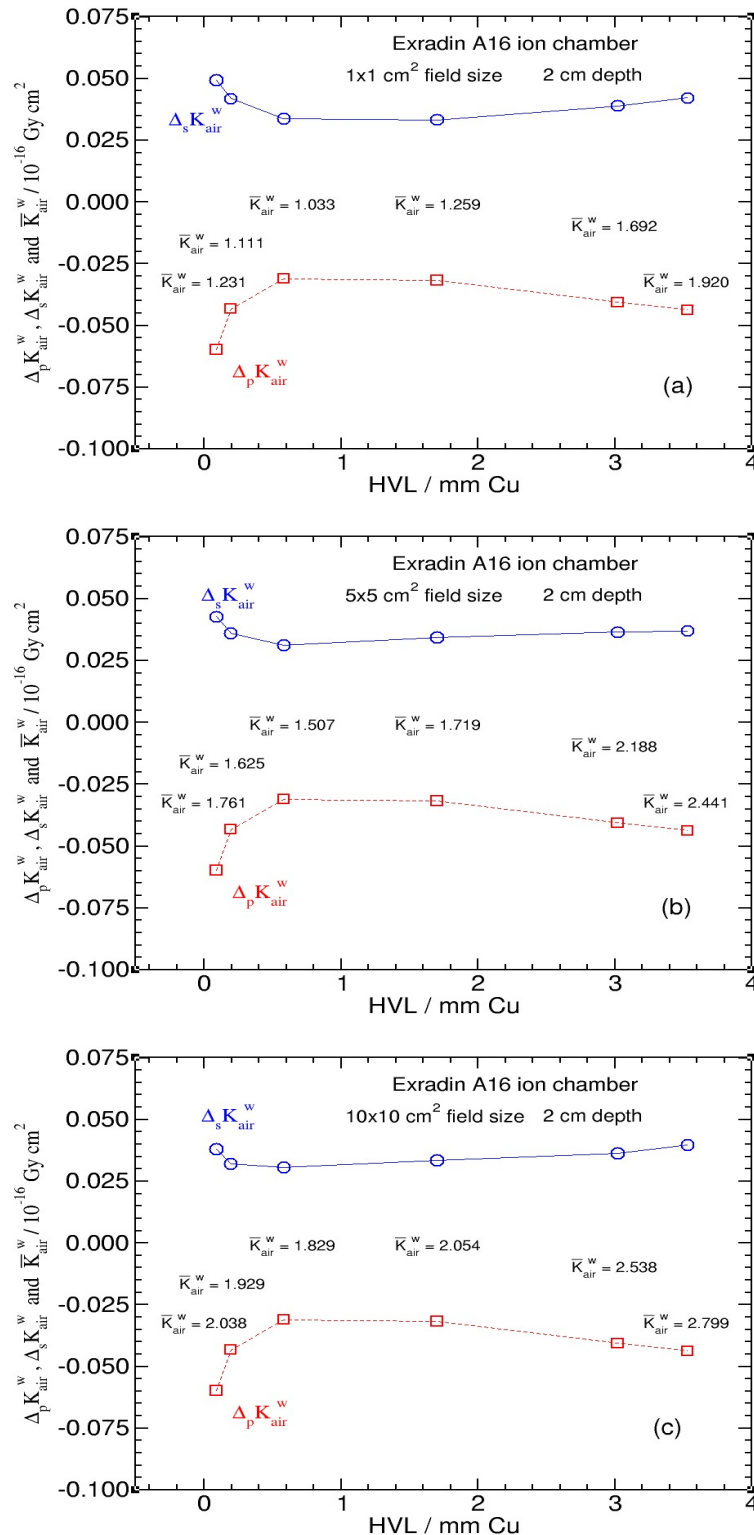


Figure 6.19: Calculated values for $\Delta_p K_{air}^w$ (eqn 5.30), $\Delta_s K_{air}^w$ (eqn 5.33), and \bar{K}_{air}^w (eqn 5.27) at 2 cm depth in water are shown for six different x-ray beams with 1 cm (a), 5 cm (b), and 10 cm field sizes. The statistical uncertainties are less than 0.1%.

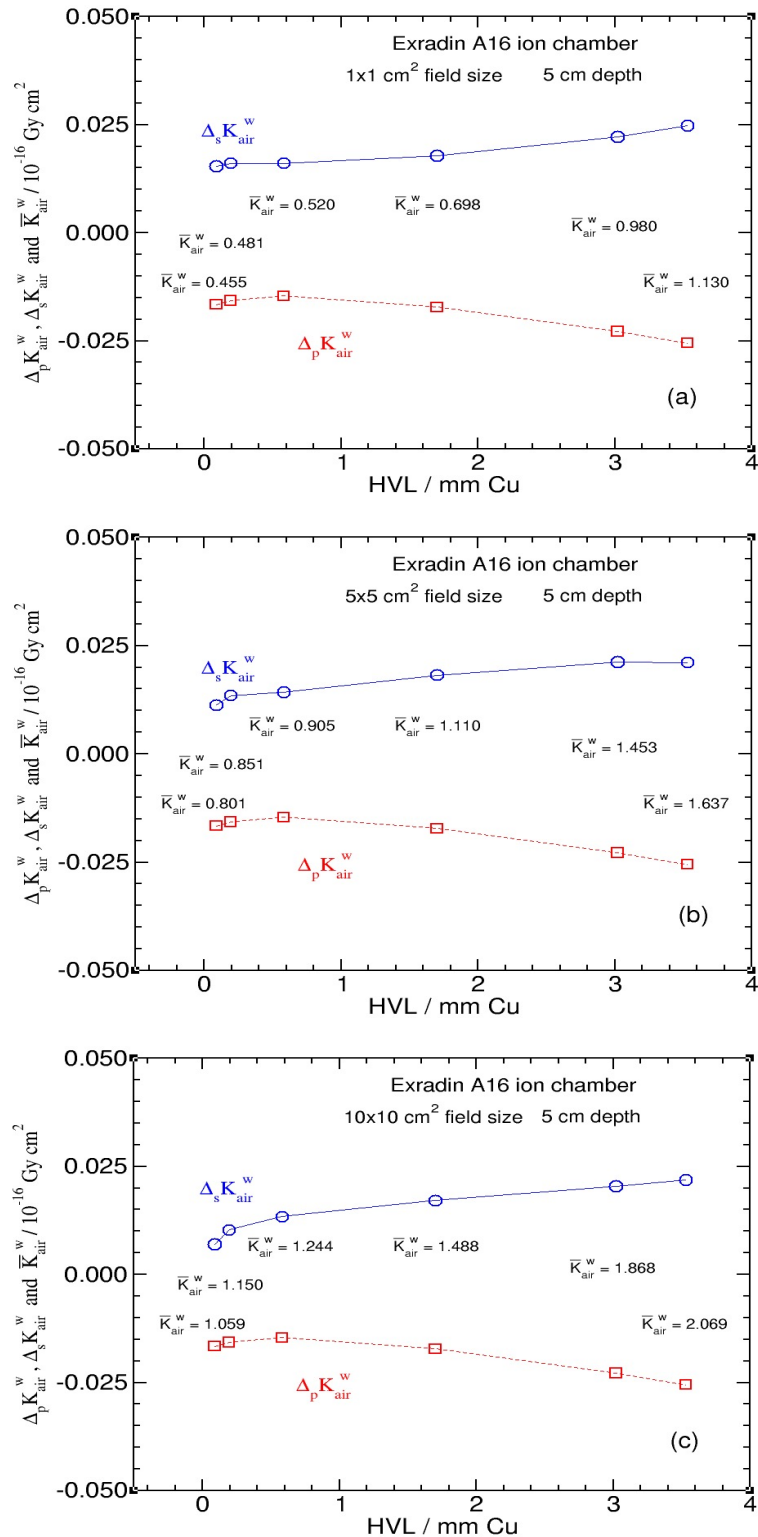


Figure 6.20: Same as figure 6.19 but at 5 cm depth.

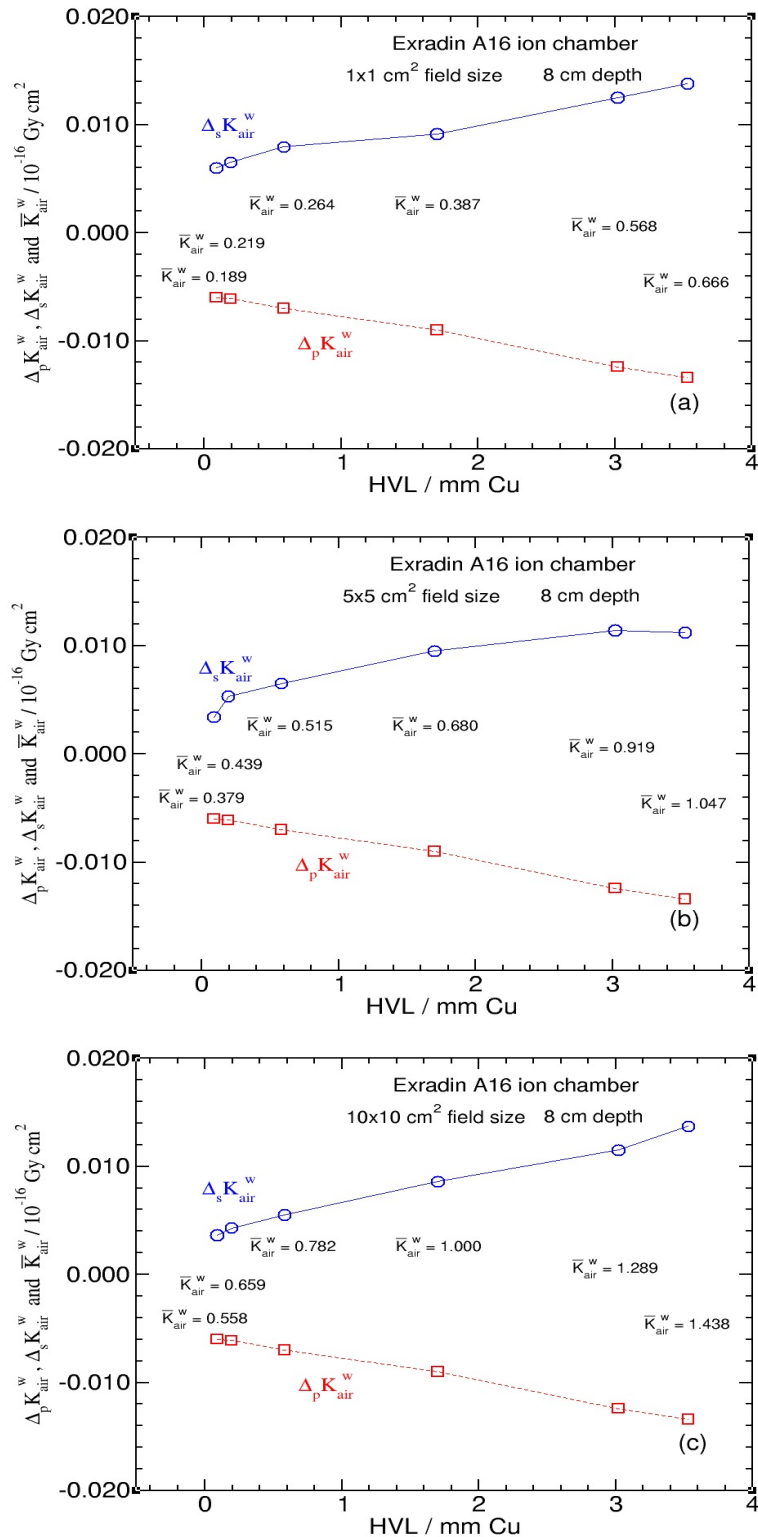


Figure 6.21: Same as figure 6.20 but at 8 cm depth.

Note that $\Delta_p K_{air}^w$ does not depend on the field size of the beam while $\Delta_s K_{air}^w$ does. The values of $\Delta_p K_{air}^w$ and $\Delta_s K_{air}^w$ get closer to zero with increasing depth in the water phantom due to the decreasing number of photons at depth in the water phantom.

6.3 The Exradin W1 plastic scintillator

The last detector used in this study is the Exradin W1 plastic scintillator. It is constructed from water equivalent materials at high energy(i.e., with low-Z and almost the water density) and composition with a cavity size of 0.0024 cm^3 which is 0.0035 times smaller than the cavity of the NE2571 ion chamber. The calculated variation of the $P_{Q,\text{cham}}$ correction factor with HVL for three different field sizes are presented in fig 6.22.

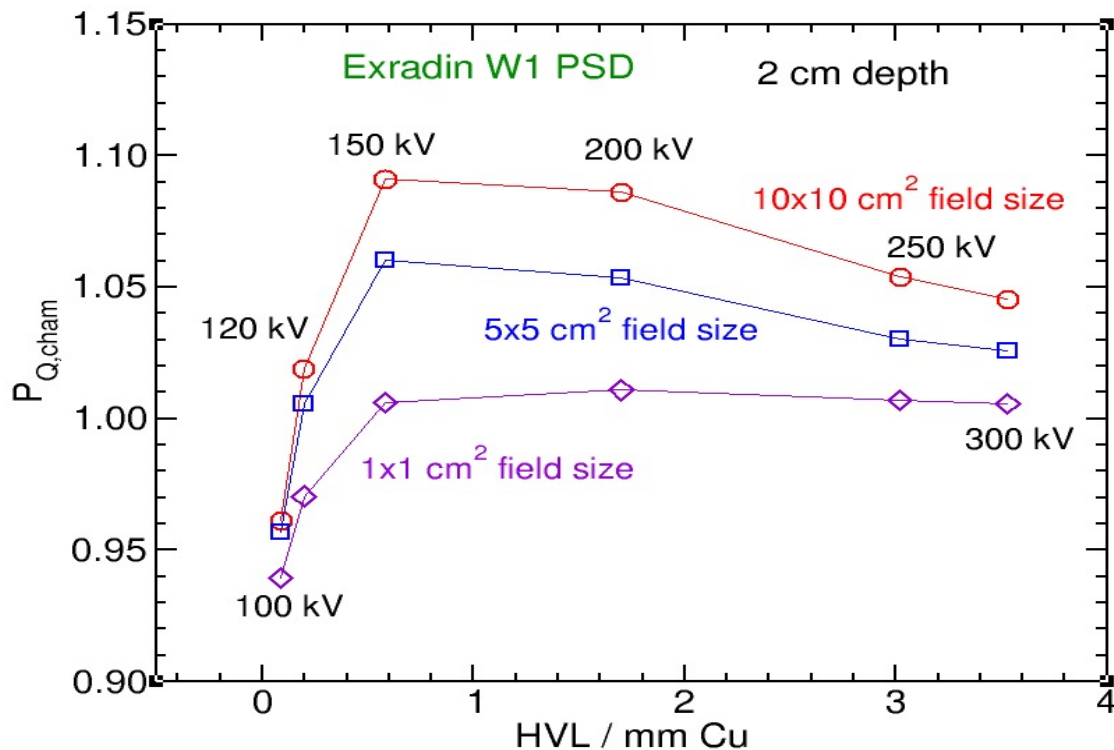


Figure 6.22: The $P_{Q,\text{cham}}$ values for the Exradin W1 plastic scintillator at 2 cm depth for 1 cm, 5 cm and 10 cm field sizes and x-ray tube potentials between 100 kV - 300 kV. The statistical uncertainties on the values are less than 0.1%.

For a given beam quality the $P_{Q,\text{cham}}$ correction factor increases with increasing

field size as opposed to the case for the Exradin A16 (fig 6.13, page 68) where the $P_{Q,cham}$ correction factor decreases as the field size increases. The variation is much more substantial than for the NE2571 ion chamber (fig 6.1, page 54) where there is virtually no variation between 5 and 10 cm field sizes. The maximum variations of the $P_{Q,cham}$ values with beam quality are 13.5%, 11%, and 7.6% for 10 cm, 5 cm, and for 1 cm field sizes respectively. These relatively large variations on the $P_{Q,cham}$ correction factor indicate that the response of Exradin W1 plastic scintillator in the water phantom is field size dependent relative to the in-air calibration due to the change of the beam quality caused by the water phantom.

6.3.1 The $P_{E,\theta}$ correction factor

The TG-61 protocol is based on the calibration of the detector in an appropriate x-ray beam in terms of air kerma free in air. A comparison between the three detectors used in this study shows that the two ion chambers have an air cavity but the Exradin W1 plastic scintillator has a cavity made of polystyrene (see fig 4.3, page 19) which means the air-kerma calibration coefficient (i.e., N_K^{air}) converts the absorbed energy in the polystyrene to that absorbed in air for the free in-air measurement.

To understand the variation of $P_{Q,cham}$ correction factor due to the cavity material for the Exradin W1 plastic scintillator, one can investigate the $P_{E,\theta}$ component of the $P_{Q,cham}$ correction factor since it takes into account the effect of the polystyrene cavity on the change of Exradin W1 plastic scintillator's response for in-water measurement relative to the free in-air calibration coefficient (i.e., N_K^{air}).

As discussed in section 5.6 (page 42), the $P_{E,\theta}$ correction factor can be calculated using,

$$P_{E,\theta} = \frac{\frac{\bar{K}_{air}^w}{D_{cav}^{w,stemless}}}{\frac{K_{air}^{free\ in-air}}{D_{cav}^{air,stemless}}} . \quad (6.8)$$

As mentioned in section 1.1 (page 3), the f conversion factor relates dose to the detector's cavity (i.e., Exradin W1) to the dose to the medium which is air in this case (see eqn 1.3, page 2). This conversion factor is approximately the ratio for air to polystyrene of the mean mass energy absorption coefficient averaged over the photon energy fluence spectrum (see eqn 1.4, page 3) for the Exradin W1 plastic scintillator

since its sensitive volume is made of polystyrene. Using eqn 1.4 (page 3), eqn 6.8 can be rewritten as,

$$P_{E,\theta} = \frac{f^w}{f^{free-in-air}} = \frac{\left[\left(\frac{\bar{\mu}_{en}}{\rho} \right)_{pst}^{air} \right]_{water}}{\left[\left(\frac{\bar{\mu}_{en}}{\rho} \right)_{pst}^{air} \right]_{air}}, \quad (6.9)$$

where $\left[\left(\frac{\bar{\mu}_{en}}{\rho} \right)_{pst}^{air} \right]_{water}$ is the ratio for air to polystyrene of the mean mass energy absorption coefficient in air averaged over the photon energy fluence spectrum which converts the absorbed energy in the polystyrene to the air for the in-water measurement and $\left[\left(\frac{\bar{\mu}_{en}}{\rho} \right)_{pst}^{air} \right]_{air}$ is the corresponding quantity for the free in-air measurement.

The variation of $\left[\left(\frac{\bar{\mu}_{en}}{\rho} \right)_{pst}^{air} \right]_{water}$ with HVL and field size has been studied but $\left[\left(\frac{\bar{\mu}_{en}}{\rho} \right)_{pst}^{air} \right]_{air}$ has been considered to be field size independent due to the small fraction of scattered photons produced in air.

The $\left[\left(\frac{\bar{\mu}_{en}}{\rho} \right)_{pst}^{air} \right]_{water}$ values were calculated using the same method as the $\left[\left(\frac{\bar{\mu}_{en}}{\rho} \right)_{air}^w \right]_{water}$ calculation (see fig 5.2, page 26) but instead of a water cavity in the water phantom, a polystyrene cavity was employed. The $\left[\left(\frac{\bar{\mu}_{en}}{\rho} \right)_{pst}^{air} \right]_{water}$ variation with HVL for the three different field sizes at 2 cm depth in water is shown in fig 6.23.

Fig 6.23 clearly shows a very large variation of the $\left[\left(\frac{\bar{\mu}_{en}}{\rho} \right)_{pst}^{air} \right]_{water}$ values as a function of HVL and a large variation between the three different field sizes for a specific HVL. The $\left[\left(\frac{\bar{\mu}_{en}}{\rho} \right)_{pst}^{air} \right]_{water}$ values increase with increasing field size and they increase substantially for lower-energy photons and these increase for larger field sizes.

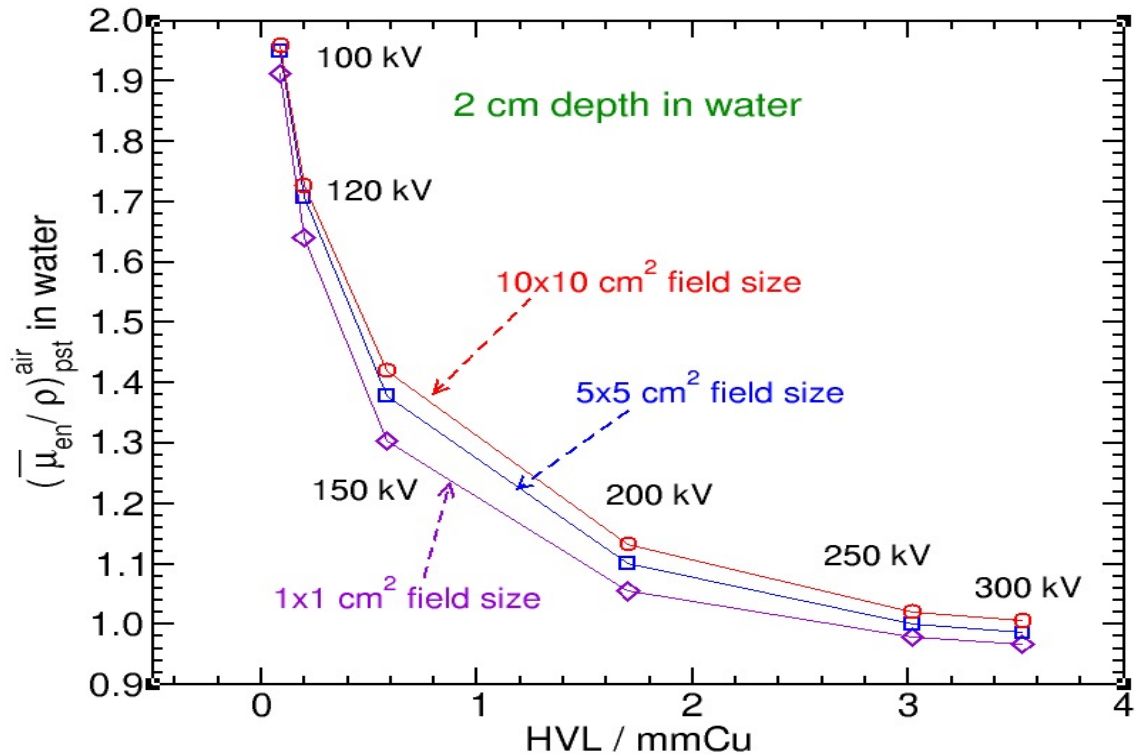


Figure 6.23: The $\left[\left(\frac{\bar{\mu}_{en}}{\rho} \right)_{pst}^{air} \right]_{water}$ variation with HVL at 2 cm depth for 1 cm, 5 cm and 10 cm field sizes and x-ray tube potential between 100 kV and 300 kV. The statistical uncertainties on the values are less than 0.1%.

The maximum deviation is 13% for the 150 kV x-ray beam (HVL: 0.581 mm Cu). This variation decreases for lower and higher energies. In addition to the field size dependence, the change of $\left[\left(\frac{\bar{\mu}_{en}}{\rho} \right)_{pst}^{air} \right]_{water}$ values with HVL is substantial. Beaulieu et al.²³ discussed the properties of a scintillation detector for mega-voltage photon beams. The $\left[\left(\frac{\bar{\mu}_{en}}{\rho} \right)_{pst}^{air} \right]_{water}$ values in their paper show it is energy independent over the range from 0.3 MeV to 3 MeV average energy of photon beams while fig 6.23 shows that the variation of $\left[\left(\frac{\bar{\mu}_{en}}{\rho} \right)_{pst}^{air} \right]_{water}$ is strongly energy dependent for 100 kV - 300 kV x-ray beams (i.e., 46.7 keV - 151 keV average energies).

To study the variation of the $P_{E,\theta}$ correction factor with field size, one can calculate the ratio of the $P_{E,\theta}$ corrections for two different field sizes. Using eqn 6.9 (page 82)

and the assumption of negligible variation of $\left[\left(\frac{\bar{\mu}_{en}}{\rho} \right)_{pst}^{air} \right]_{air}$ with field size, we have,

$$[P_{E,\theta}]_b^a = \frac{P_{E,\theta}^a}{P_{E,\theta}^b} = \frac{\left[\left(\frac{\bar{\mu}_{en}}{\rho} \right)_{pst}^{air} \right]_{water}^a}{\left[\left(\frac{\bar{\mu}_{en}}{\rho} \right)_{pst}^{air} \right]_{water}^b}, \quad (6.10)$$

where a and b represent the corresponding factors for the field size a and b .

To illustrate the influence of the $\left[\left(\frac{\bar{\mu}_{en}}{\rho} \right)_{pst}^{air} \right]_{water}$ variation with field size on the $P_{Q,cham}$ correction factor for the Exradin W1 plastic scintillator, values of $\left[\left(\frac{\bar{\mu}_{en}}{\rho} \right)_{pst}^{air} \right]_{water}$ normalized to the 1 cm field size are presented in fig 6.24.

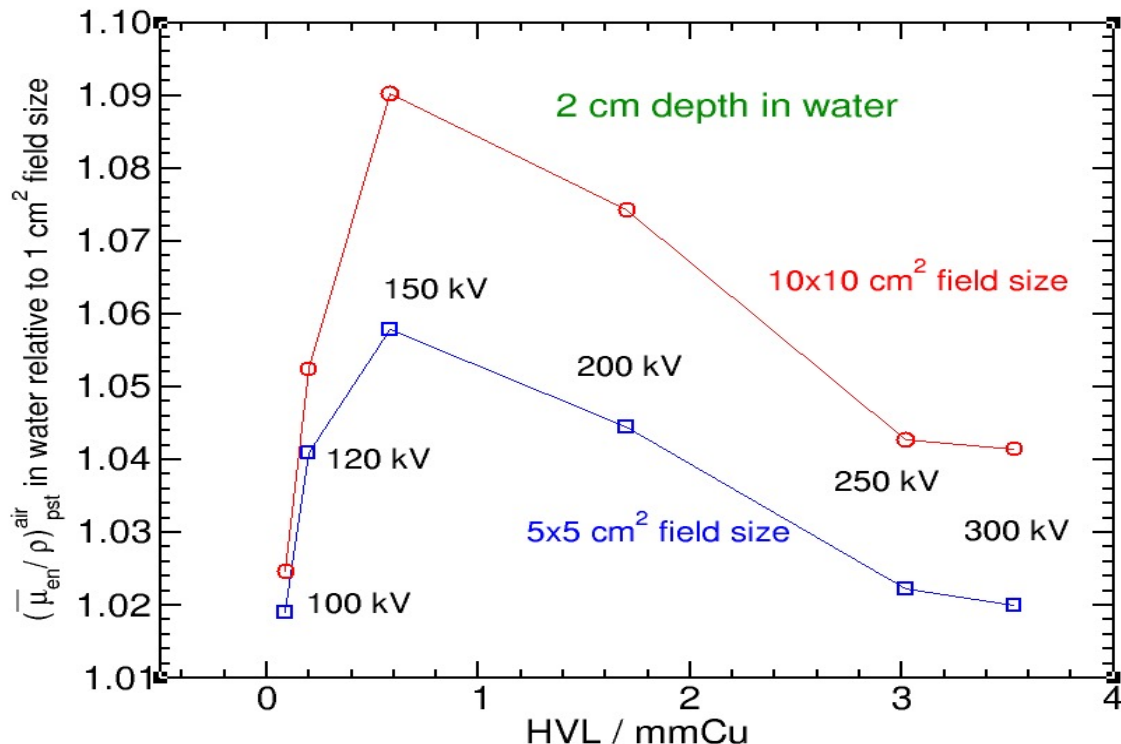


Figure 6.24: Values of $\left[\left(\frac{\bar{\mu}_{en}}{\rho} \right)_{pst}^{air} \right]_{water}$ normalized at values for 1 cm field size versus HVL at 2 cm depth for 5 cm and 10 cm field sizes and x-ray tube potential between 100 kV and 300 kV. The statistical uncertainties on the values are less than 0.1%.

The difference between 5 cm and 10 cm field size in fig 6.24 almost equals the difference between the $P_{Q,cham}$ values of the Exradin W1 plastic scintillator for a specific HVL between 5 cm and 10 cm field sizes shown in fig 6.22. This indicates that the $P_{E,\theta}$ correction is more important than the other two components (i.e., $P_{stem,w}$ and P_{dis}). For example, for the 100 kV (HVL: 0.088 mm Cu) x-ray beam the deviation of the $P_{E,\theta}$ factor from the $P_{Q,cham}$ correction factor is 1.1% at the 10 cm field size. This deviation decreases with increasing depth. For higher energy beams, the differences between the $P_{E,\theta}$ and $P_{Q,cham}$ values are less than 0.3%.

The $P_{Q,cham}$ correction factor and its components for the Exradin W1 plastic scintillator are shown in figs 6.25, 6.26 and 6.27 at 2 cm, 5 cm and 8 cm depths respectively. Note that the most important contribution to the $P_{Q,cham}$ correction factor is the $P_{E,\theta}$ correction factor.

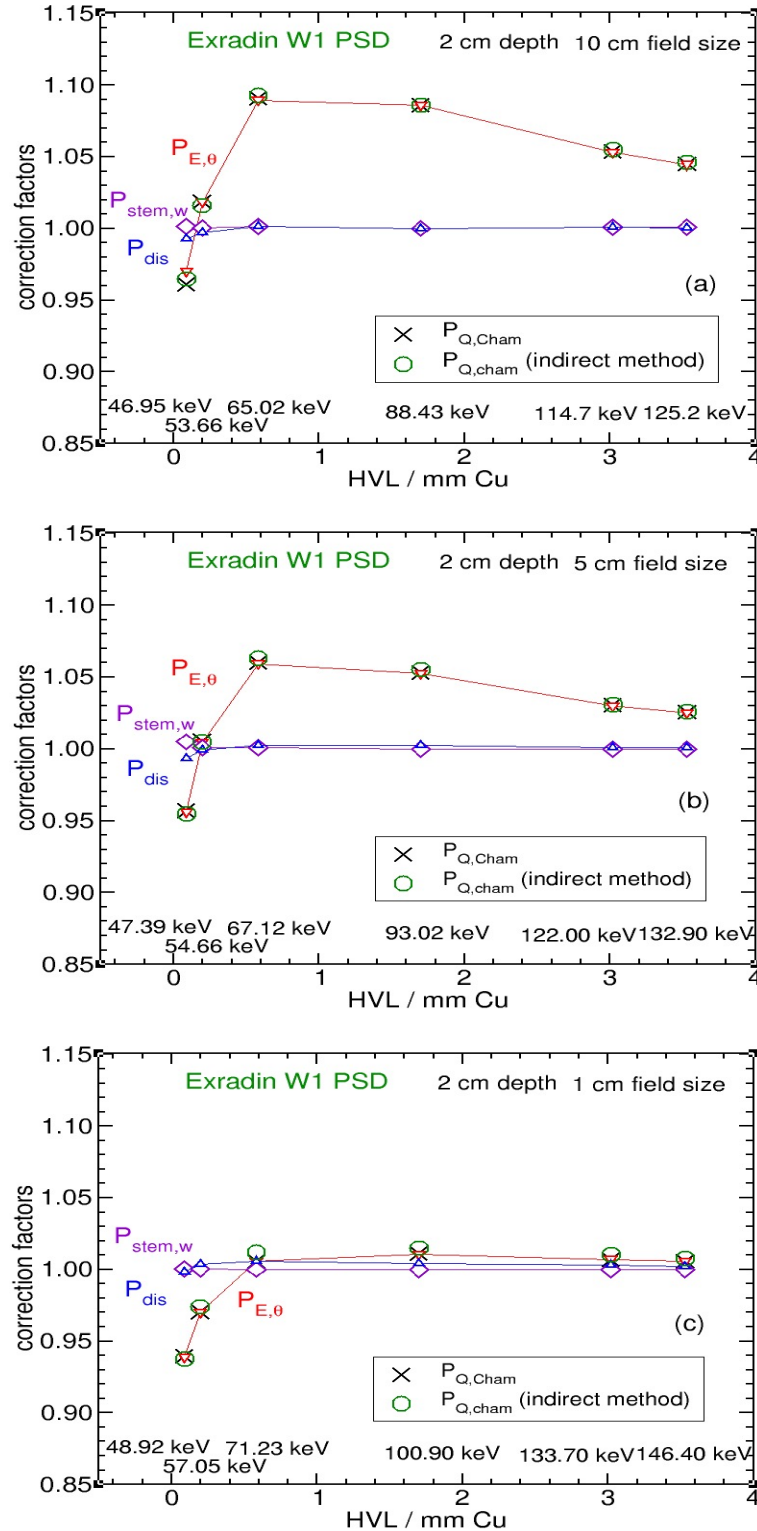


Figure 6.25: The variations with HVL of the $P_{Q,Cham}$ correction factor and its components for the Exradin W1 plastic scintillator for 10 cm (a), 5 cm (b), and 1 cm (c) field sizes at 2 cm depth in the water phantom.

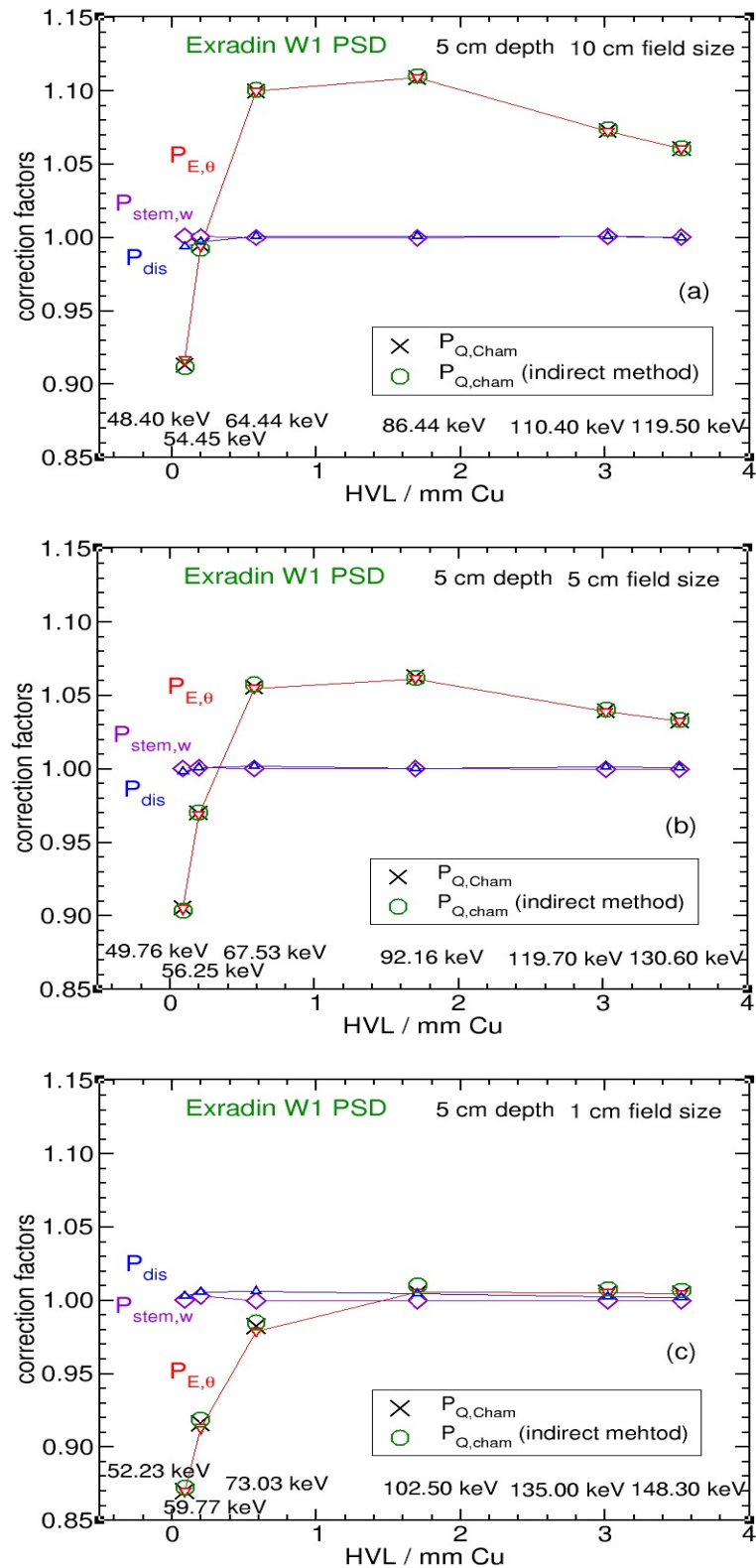


Figure 6.26: Same as fig 6.25 but at 5 cm depth in the water phantom.

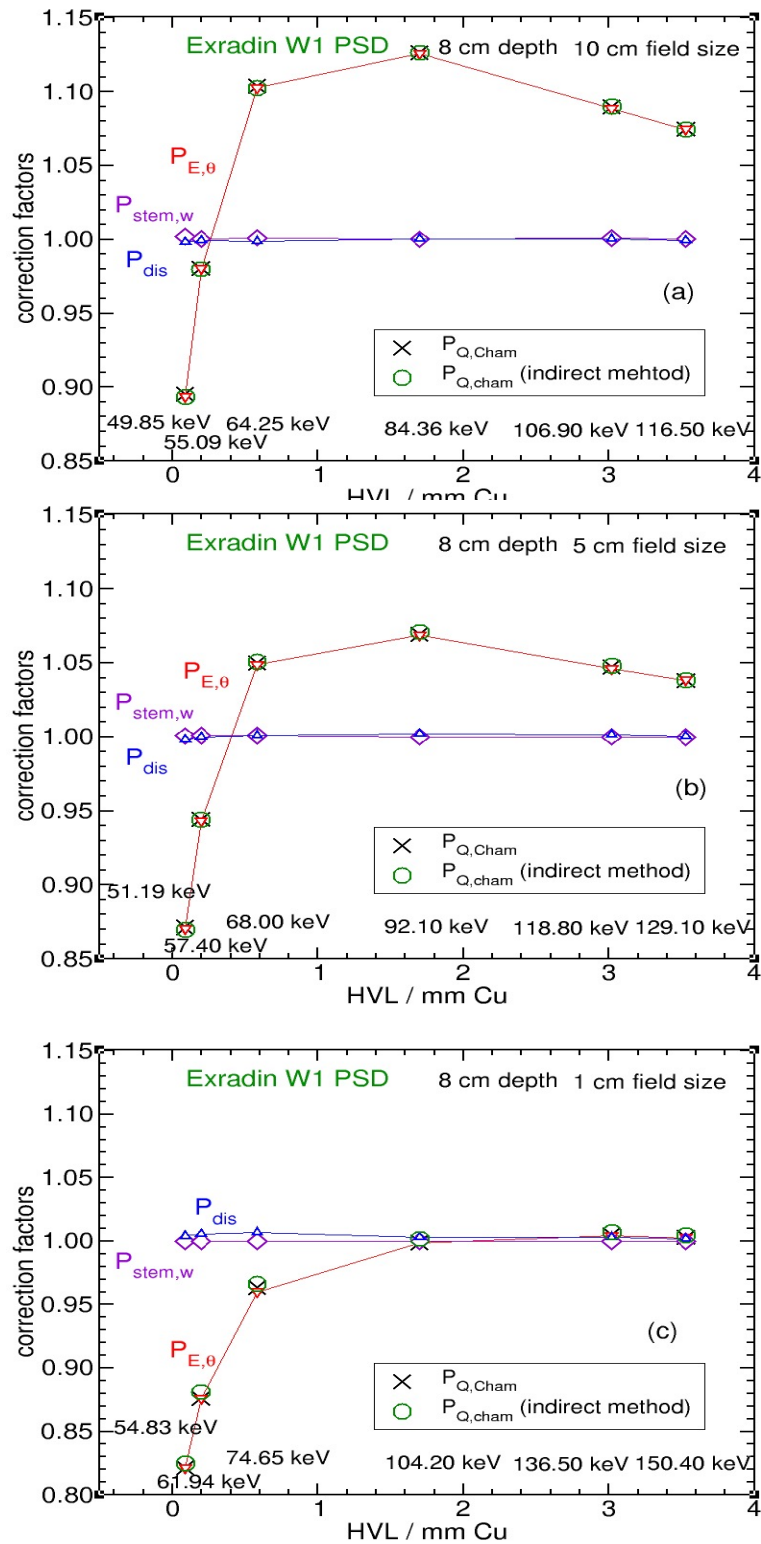


Figure 6.27: Same as fig 6.25 but at 8 cm depth in the water phantom.

6.3.2 The $P_{stem,w}$ and P_{dis} correction factors

Fig 6.25 shows the stem correction factor (i.e., $P_{stem,w}$) has a maximum value of 1.006 for the 100 kV (HVL: 0.088 mm Cu) x-ray beam at 5 cm field size. The $P_{stem,w}$ correction factor can be considered to be unity within the statistical uncertainty (i.e., 0.1%) for other beam qualities, used in this thesis. The main reason for this negligible influence of the $P_{stem,w}$ on the $P_{Q,cham}$ correction factor are the stem size of the Exradin W1 plastic scintillator (see chapter 4, page 16) and the low-Z materials of the stem relative to the stems of the Exradin A16 and NE2471 ion chambers. Also, the stem is isolated from the sensitive volume, unlike for the two ion chambers where the stem starts right after the sensitive volume.

The displacement correction factor has a deviation from unity of up to 0.7% at the lowest energy and 10 cm field size. This deviation decreases as depth increases. For higher energy beams, the P_{dis} correction factor equals unity within the 0.3% for all field sizes. The small body size of the Exradin W1 plastic scintillator (see chapter 4, page 16) and its near water density are the main reasons for such a small displacement correction factor.

Figs 6.25, 6.26 and 6.27 show that for a specific beam quality, the $P_{Q,cham}$ correction factor decreases with decreasing field size and its maximum variation is 5.5% at 5 cm depth between 10 cm and 1 cm field sizes which is due to the variation of the $P_{E,\theta}$ correction factor at this depth as is the case at 2 cm depth.

The $P_{stem,w}$ correction factor gets even closer to unity at 5 cm depth relative to that at 2 cm depth in water and can be considered to be unity within the 0.2% uncertainty. The same statement can be applied to the P_{dis} correction factor except for the 100 kV x-ray beam (HVL: 0.088 mm Cu) at 5 cm depth which is 0.6% different from unity.

At 8 cm depth in the water phantom (see fig 6.27), the $P_{E,\theta}$ component still governs the $P_{Q,cham}$ correction factor as at depth of 2 cm and 5 cm. The maximum variation of the $P_{E,\theta}$ correction is 13% for the 200 kV x-ray beam (HVL: 0.591 mm Cu) between 10 cm to the 1 cm depth.

The variation of $P_{stem,w}$ at 8 cm depth is negligible and can be considered to be unity within 0.2%. For a 130 kV x-ray beam (HVL: 0.195 mm Cu), the P_{dis} correction factor is 0.6% above unity and is negligible for other beam qualities at 8 cm depth within 0.2%.

The previous method for the analysis of the P_{dis} correction factor was not employed

for the Exradin W1 plastic scintillator since its body size is so small and the correction to the displaced water is almost negligible for all depths and field sizes.

Chapter 7

Conclusions

The main goal of this research is to calculate the $P_{Q,cham}$ correction factor and its components (i.e., $P_{E,\theta}$, $P_{stem,w}$, and P_{dis}) for three different detectors, namely the NE2571 ion chamber, Exradin A16 ion chamber, and Exradin W1 plastic scintillator. The variation of the $P_{Q,cham}$ correction factor with depth in a water phantom and for three different field sizes (i.e., 1x1 cm², 5x5 cm², and 10x10 cm²) was investigated for six different x-ray beams between 100 kV (HVL: 0.088 mm Cu) to 300 kV (HVL: 3.53 mm Cu). Two methods were introduced in section 5.6 (page 39), the direct and indirect methods. In the direct method the $P_{Q,cham}$ correction factor was calculated using eqn 5.5 (page 39) with 0.1% statistical uncertainty. In the indirect method, three components of the $P_{Q,cham}$ correction factor were obtained and then the overall detector correction factor ($P_{Q,cham}$) was calculated with 0.3% statistical uncertainty using

$$P_{Q,cham} = P_{E,\theta} \times P_{stem,w} \times P_{dis} . \quad (7.1)$$

7.1 The NE2571 ion chamber

The variation of the $P_{Q,cham}$ correction factor with HVL for two different field sizes (i.e., 5x5 cm² and 10x10 cm²) and 2 cm to 11 cm depths, was calculated. The maximum variation of the $P_{Q,cham}$ correction factor with depth is 1.5% and occurs for the 100 kV x-ray beam (HVL: 0.088 mm Cu). Significant improvement in the uncertainty of the $P_{Q,cham}$ correction factor was obtained in comparison with the overall uncertainty reported in the TG-61 protocol which is 1.5 % including at least a 1% systematic uncertainty while the $P_{Q,cham}$ values of this work have 0.1% statistical uncertainty. The systematic uncertainty for EGSnrc code system was previously reported by Muir and

Rogers³⁴ as 0.3% to 0.5% due to cross-section uncertainties in the energy range between cobalt beam energy (i.e., 1.25 MeV) and 25 MV beam. The uncertainty in photon cross sections is even greater for x-ray beam energies where the photoelectric effect dominates. In addition to the cross-section as a source of uncertainty, the value of $\left(\frac{W}{e}\right)_{air}$ contributes to the overall systematic uncertainty if there is a large change in energy. In this thesis, since the correction factors were calculated using the ratio of dose for the in-water and in-air calculations where the change in beam quality is small compared to those in Muir and Rogers's work, the systematic uncertainty is assumed to be around 0.5%.

The maximum variation of the $P_{Q,cham}$ correction factor for the NE2571 ion chamber at 2 cm depth are 2.6% with beam qualities between 100 kV (HVL: 0.088 mm Cu) to 300 kV(HVL: 3.53 mm Cu) and 0.26% with field size between 5x5 cm² and 10x10 cm². At lower energies, the P_{dis} correction dominates the other two components of the $P_{Q,cham}$ correction factor at 2 cm and 5 cm depth while the $P_{stem,w}$ factor is more important than other two factors at 8 cm and 11 cm depth. The $P_{Q,cham}$ values obtained from direct and indirect methods are in agreement within the statistical uncertainties. A comparison between the $P_{Q,cham}$ correction factor values in this thesis with those from the TG-61 protocol shows a disagreement of up to 0.8% for the 100 kV x-ray beam (HVL: 0.088 mm Cu). This disagreement decreases to 0.2% for a 70 kV x-ray beam (HVL: 0.088 mm Cu) with the same HVL as the 100 kV x-ray beam. This indicates that the specification of an x-ray beam must be done using two parameters, the x-ray tube potential and HVL of the beam.

7.2 The Exradin A16 ion chamber

The $P_{Q,cham}$ correction factor for the Exradin A16 varies significantly with field size and it decreases as field size increases from 150 kV (HVL: 0.591 mm Cu) to 300 kV (HVL: 3.53 mm Cu) x-ray beams. The maximum variation of the $P_{Q,cham}$ correction factor with HVL is 15.5%, 15%, and 26% for the 1x1 cm², 5x5 cm², and 10x10 cm² respectively. These variations are up to 2% for 100 kV (HVL: 0.088 mm Cu) and 120 kV (HVL: 0.195 mm Cu) x-ray beams.

The maximum variation of the $P_{Q,cham}$ correction factor with depth from 2 cm to

8 cm occurs for the 100 kV (HVL: 0.088 mm Cu) beam and is 17%, 15%, and 13% for the 1x1 cm², 5x5 cm², and 10x10 cm² field sizes respectively.

The $P_{E,\theta}$ correction factor mostly governs the $P_{Q,cham}$ variation which is due to the high-Z materials in the electrode of the Exradin A16 ion chamber discussed in section 6.2 (page 68). The $P_{stem,w}$ correction factor for the Exradin A16 ion chamber is greater than the same correction factor for the NE2571 ion chamber and Exradin W1 plastic scintillator mainly due to the larger stem size and the high-Z materials of the stem relative to the other two detectors. The maximum variation of the $P_{stem,w}$ correction factor with HVL is 5.5% and occurs for the 1x1 cm² field size and 2 cm depth.

The P_{dis} correction factor has the smallest contribution to the $P_{Q,cham}$ correction factor for the Exradin A16 ion chamber since the cavity size of the Exradin A16 ion chamber is so small. The P_{dis} correction varies up to 1% for the 100 kV x-ray beam (HVL: 0.088 mm Cu) and 10x10 cm² field size at 2 cm depth.

7.3 The Exradin W1 plastic scintillator

The $P_{Q,cham}$ correction factor for the Exradin W1 plastic scintillator varies dramatically with field size of the beam as shown in fig 6.22 (page 80). The $P_{Q,cham}$ values increase with increasing field size as opposed to the Exradin A16 ion chamber for which the $P_{Q,cham}$ values decrease as field size increases for x-ray beams above 120 kV (HVL: 0.195 mm Cu). The maximum variation of the $P_{Q,cham}$ correction factor with HVL at 2 cm depth is 7.5%, 10.5%, and 13.5% for the 1x1 cm², 5x5 cm², and 10x10 cm² field sizes respectively.

The contribution of the $P_{E,\theta}$ correction to the $P_{Q,cham}$ correction factor is larger for the Exradin W1 plastic scintillator in comparison with the other two detectors. This is mainly due to the large energy dependency of the Exradin W1 plastic scintillator response discussed in section 6.2 (page 68).

The $P_{stem,w}$ correction factor has a maximum variation of 0.6% within the 0.1% statistical uncertainties. The $P_{stem,w}$ correction factor can be considered to be unity for x-ray beams used in this study with tube potential greater than 100 kV. The negligible influence of the $P_{stem,w}$ on the $P_{Q,cham}$ correction factor is due to the small stem size of the Exradin W1 plastic scintillator and the low-Z materials of the stem relative to the

stems of the Exradin A16 and NE2571 ion chambers.

The P_{dis} correction factor has a deviation from unity of up to 0.7% with 0.1% statistical uncertainty at lowest energy and 10x10 cm² field size. For higher energy beams, this correction factor equals unity within 0.3% for all field sizes and depths. The small body size and near water density of the Exradin W1 plastic scintillator are the main reason for having a small displacement correction factor.

As opposed to the NE2571 ion chamber, our results show that the Exradin A16 ion chamber and Exradin W1 plastic scintillator are strongly energy dependent for the range of medium energy x-ray beams (100 kV - 300 kV) and may not be suitable for kilovoltage x-ray dosimetry. If these detectors are used, large variations of the correction factors must be carefully considered.

References

- [1] A. E. Nahum and R. T. Knight, Consistent formalism for kV x-ray dosimetry., In “Proceedings of the IAEA International Symposium on Measurement Assurance in Dosimetry” (Vienna: IAEA) , 451 – 459 (1994). (pp [xii](#) and [47](#))
- [2] C.-M. Ma and A. E. Nahum, Monte Carlo calculated correction factors for a NE2571 chamber in medium-energy photon beams, In “Proceedings of the IAEA International Symposium on Measurement Assurance in Dosimetry” (Vienna: IAEA) , 371 – 382 (1994). (pp [xii](#), [10](#), [39](#), and [66](#))
- [3] J. Seuntjens and F. Verhaegen, Dependence of overall correction factor of a cylindrical ionization chamber on field size and depth in medium energy X-ray beams, Med. Phys. **23**, 1789 – 1796 (1996). (pp [xii](#), [26](#), [39](#), [42](#), [45](#), [48](#), [54](#), [55](#), [60](#), [61](#), [62](#), and [66](#))
- [4] C.-M. Ma, C. W. Coffey, L. A. Dewerd, C. Liu, R. Nath, S. M. Seltzer, and J. P. Seuntjens, Status of Kilovoltage X-ray Beam Dosimetry in Radiotherapy, in *Kilovoltage x-ray beam dosimetry for radiotherapy and radiobiology: Proceedings of a workshop*, edited by C.-M. Ma and J. P. Seuntjens, pages 27 – 42, Medical Physics Publ., Madison, WI, USA, 1999. (pp [1](#), [4](#), [18](#), and [26](#))
- [5] C.-M. Ma, C. W. Coffey, L. A. DeWerd, C. Liu, R. Nath, S. M. Seltzer, and J. Seuntjens, Dosimetry of kilovoltage x-ray beams for radiotherapy, Med. Phys. **23**, 1114 (abstract) (1996). (pp [1](#), [6](#), [7](#), [8](#), and [40](#))
- [6] C. M. Ma, C. W. Coffey, L. A. DeWerd, C. Lu, R. Nath, S. M. Seltzer, and J. P. Seuntjens, AAPM protocol for 40-300 keV x-ray beam dosimetry in radiotherapy and radiobiology, Med. Phys. **28**, 868 – 893 (2001). (pp [1](#), [4](#), [8](#), and [12](#))
- [7] NCRP Report 69, Dosimetry of X-ray and gamma ray beams for Radiation Therapy in the Energy Range 10 keV to 50 MeV, NCRP Publications, 7910 Woodmont Avenue, Washington DC, 20014 USA (1981). (p [1](#))
- [8] IAEA, *Absorbed Dose Determination in Photon and Electron Beams; An International Code of Practice*, volume 277 of *Technical Report Series*, IAEA, Vienna, 1987. (pp [1](#) and [6](#))
- [9] D. W. O. Rogers, General characteristics of radiation dosimeters and a terminology to describe them, in *Clinical Dosimetry Measurements in Radiotherapy*, edited by D. W. O. Rogers and J. E. Cygler, pages 137 – 145, Medical Physics Publishing, Madison, Wisconsin, 2009. (p [2](#))

- [10] A. R. Beierholm, C. F. Behrens, and C. E. Andersen, Comment on “Characterization of the Exradin W1 scintillator for use in radiotherapy” [Med. Phys. 42, 297–304 (2015)], Med. Phys. **42**, 4414 – 4416 (2015). (p 2)
- [11] J. P. Seuntjens, L. Van der Zwan, and C.-M. Ma, Type dependent correction factors for cylindrical chambers for in-phantom dosimetry in medium energy x-ray beams, in *Kilovoltage x-ray beam dosimetry for radiotherapy and radiobiology: Proceedings of a workshop*, edited by C.-M. Ma and J. P. Seuntjens, pages 159 – 174, Medical Physics Publ., Madison, WI, USA, 1999. (pp 3, 12, 39, 53, and 54)
- [12] W. R. Nelson, H. Hirayama, and D. W. O. Rogers, The EGS4 code system, Report SLAC-265, Stanford Linear Accelerator Center, Stanford, California, 1985. (pp 3 and 21)
- [13] D. W. O. Rogers, How accurately can EGS4/PRESTA calculate ion chamber response?, Med. Phys. **20**, 319 – 323 (1993). (p 3)
- [14] I. Kawrakow, E. Mainegra-Hing, D. W. O. Rogers, F. Tessier, and B. R. B. Walters, The EGSnrc Code System: Monte Carlo simulation of electron and photon transport, NRC Technical Report PIRS-701 v4-2-3-2, National Research Council Canada, Ottawa, Canada. http://www.nrc-cnrc.gc.ca/eng/solutions/advisory/egsnrc/download_egsnrc.html, 2011. (p 3)
- [15] G. Poludniowski, G. Landry, F. DeBlois, P. M. Evans, and F. Verhaegen, SpekCalc : a program to calculate photon spectra from tungsten anode x-ray tubes, Phys. Med. Biol. **54**, N433 – N438 (2009). (pp 4, 12, and 55)
- [16] IAEA, *Absorbed Dose Determination in External Beam Radiotherapy: An International Code of Practice for Dosimetry Based on Standards of Absorbed Dose to Water*, volume 398 of *Technical Report Series*, IAEA, Vienna, 2001. (p 6)
- [17] K. Cranley, B. J. Gilmore, G. W. Fogarty, and L. Desponds, Catalogue of diagnostic x-ray spectra and other data - CD edition (electronic version prepared by D Sutton), Technical Report Report 78, The Institute of Physics and Engineering in Medicine (IPEM), 1997. (p 12)
- [18] D. W. O. Rogers, C.-M. Ma, G. X. Ding, B. Walters, D. Sheikh-Bagheri, and G. G. Zhang, BEAMnrc Users Manual, NRC Report PIRS 509(a)revF (2001). (p 12)
- [19] C.-M. Ma and J. P. Seuntjens, Mass-energy absorption coefficient and backscatter factor ratios for kilovoltage x-ray beams, Phys. Med. Biol. **44**, 131 – 143 (1999). (pp 12, 26, and 53)
- [20] D. W. O. Rogers, I. Kawrakow, J. P. Seuntjens, and B. R. B. Walters, NRC User Codes for EGSnrc, NRC Technical Report PIRS-702, National Research Council Canada, Ottawa, Canada. <http://www.irs.inms.nrc.ca/inms/irs/EGSnrc/EGSnrc.html>, 2000. (pp 14 and 21)
- [21] I. Kawrakow, : the EGSnrc C++ class library, Technical Report PIRS-899, National Research Council Canada, Ottawa, Canada, 2005. (pp 16 and 21)

- [22] B. R. Muir and D. W. O. Rogers, The central electrode correction factor for high-Z electrodes in small ionization chambers, *Med. Phys.* **38**, 1081 – 1088 (2011). (pp 18 and 73)
- [23] L. Beaulieu *et al.*, Report of the Task Group 186 on model-based dose calculation methods in brachytherapy beyond the TG-43 formalism: Current status and recommendations for clinical implementation, *Med. Phys.* **39**, 6208 – 6236 (2012). (pp 18, 38, and 83)
- [24] I. Kawrakow and D. W. O. Rogers, The EGSnrc Code System: Monte Carlo simulation of electron and photon transport, Technical Report PIRS-701, National Research Council Canada, Ottawa, Canada , see <http://www.irs.inms.nrc.ca/inms/irs/EGSnrc/EGSnrc.html> (2000). (pp 21 and 55)
- [25] I. Kawrakow, Accurate condensed history Monte Carlo simulation of electron transport. I. EGSnrc, the new EGS4 version, *Med. Phys.* **27**, 485 – 498 (2000). (p 21)
- [26] J. Wulff, K. Zink, and I. Kawrakow, Efficiency improvements for ion chamber calculations in high energy photon beams, *Med. Phys.* **35**, 1328– 1336 (2008). (p 23)
- [27] C.-M. Ma and A. E. Nahum, Monte Carlo calculated stem effect corrections for NE2561 and NE2571 chambers in medium-energy x-ray beams, *Phys. Med. Biol.* **40**, 63 – 72 (1995). (pp 45, 46, and 62)
- [28] C.-M. Ma, Monte Carlo simulation of dosimeter response using transputers, PhD Thesis, London University (Institute of Cancer Research), also available as Int. Report ICR-PHYS-1/92 (Sutton, Surrey SM2 5PT, UK: Physics Dept, Royal Marsden Hospital, 1992) (1992). (p 46)
- [29] C.-M. Ma and A. E. Nahum, Calculation of ion chamber displacement effect corrections for medium-energy x-ray dosimetry, *Med. Phys.* **40**, 45–62 (1995). (p 47)
- [30] A. E. Nahum, Perturbation Effects in Dosimetry, Technical Report ICR-PHYS-1/94, Joint Dept of Physics, The Royal Marsden Hospital, Sutton, Surrey, SM2 5PT, UK, 1994. (p 48)
- [31] K. V. H. Liden, Errors introduced by finite size of ion chambers in depth-dose measurements, Selected Topics in Radiation Dosimetry. In: Proceedings of an International Conference held in Vienna. (Vienna: IAEA) , 161 – 172 (1961). (p 49)
- [32] R. T. Knight and A. E. Nahum, Depth and field-size dependence of ratios of mass-energy absorption coefficient, water-to-air, for kV X-ray dosimetry, In “Proceedings of the IAEA International Symposium on Measurement Assurance in Dosimetry” (Vienna: IAEA) , 361 – 370 (1994). (p 60)

- [33] J. R. Snow, J. A. Micka, and L. A. DeWerd, Microionization chamber air-kerma calibration coefficients as a function of photon energy for x-ray spectra in the range of 20–250 kVp relative to ^{60}Co , *Med. Phys.* **40**, 041711, 5pp (2013). (p 73)
- [34] B. R. Muir and D. W. O. Rogers, Monte Carlo calculations of k_Q , the beam quality conversion factor, *Med. Phys.* **37**, 5939 – 5950 (2010). (p 92)